

Transient antenna-plasma interaction in inductive plasma thrusters

Robin Georg



THE UNIVERSITY
of ADELAIDE

Copyright 2018–2022 Robin Georg

Submission date: 8 July 2022

School of Mechanical Engineering
The University of Adelaide
5005 South Australia
Australia

The images preceding each chapter are taken from a Hubble Space Telescope mosaic image of the Andromeda galaxy. The images form a sequence from the galaxy's centre to its outer disk. Public domain. Credit: NASA, ESA, J. Dalcanton, B.F. Williams, and L.C. Johnson (University of Washington), the PHAT team, and R. Gendler.

Unless otherwise stated, all other images in this thesis are original works.

**Transient antenna-plasma interaction
in inductive plasma thrusters**

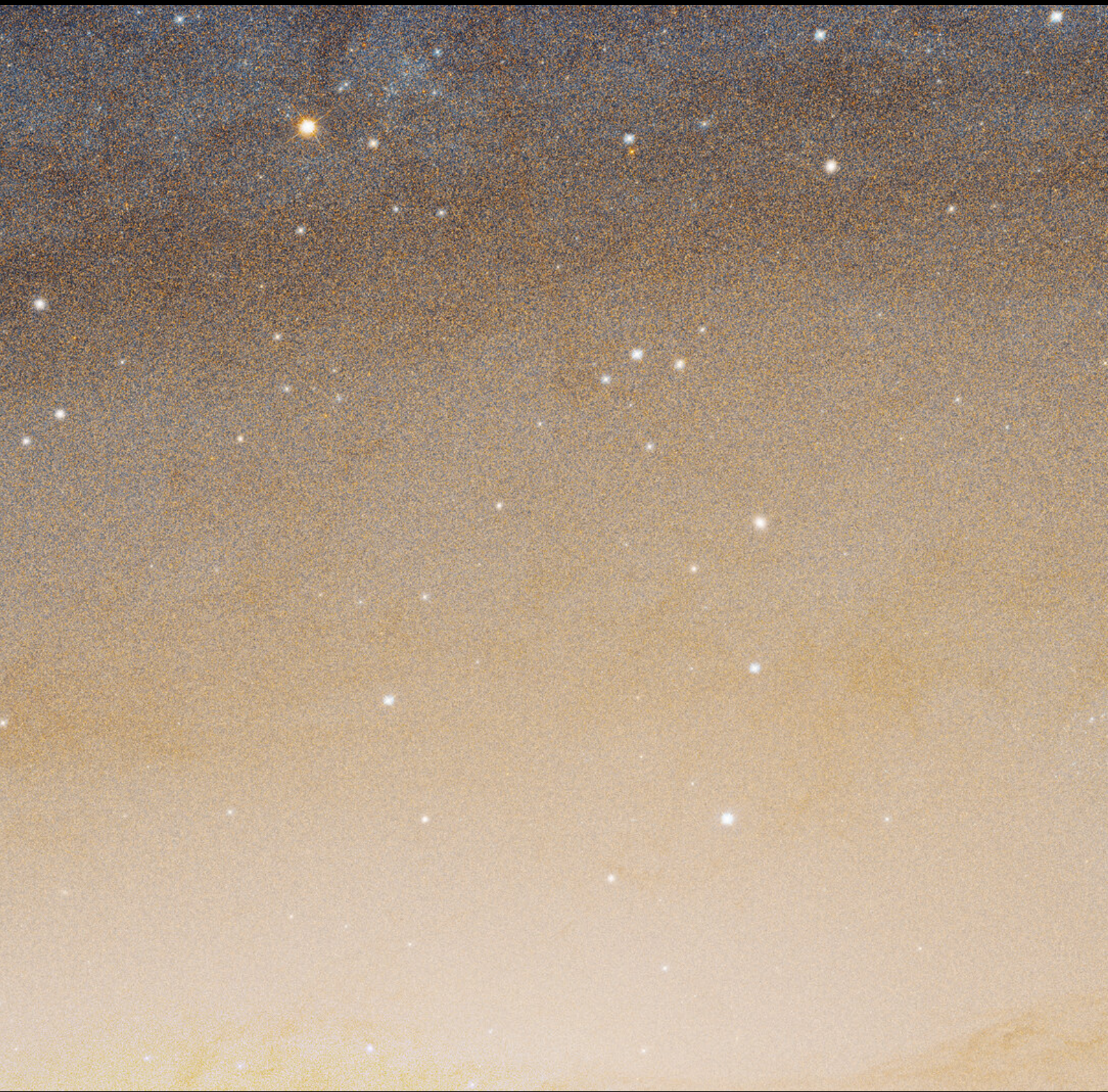
THESIS

submitted to fulfill the requirements
for the degree of Doctor of Philosophy
at the University of Adelaide

by

Robin Christopher Georg

born in Forreston, Australia



Abstract

An electric thruster using material sourced from beyond Earth as propellant would unlock new possibilities for the exploration and exploitation of space. Compared to other technologies under consideration, inductive plasma thrusters are a promising candidate due to their high thrust density and proven propellant flexibility. In contrast with conventional space propulsion technologies, inductive coupling can deliver energy to a propellant without direct contact, making it a form of electrodeless electric propulsion. This can increase its lifetime and enable a more flexible propellant choice in terms of composition. A significant hurdle to the development and eventual implementation of inductive plasma thrusters is the lack of detailed information on the discharge behaviour and diagnostic tools that can be applied for various power and propellant operating conditions. These two aspects are critical to advance the understanding of underlying phenomena and hence the potential for both optimisation and in-flight health monitoring of future thrusters.

Previous work has identified transient antenna current behaviour within an inductive plasma thruster that points to complex antenna-plasma interactions, including coupling mode transitions. This thesis documents investigations into these phenomena in order to assess, quantify, explain and exploit them. Firstly, it is shown that these phenomena are observable under a range of conditions and are strongly linked to coupling mode transitions. Secondly, the effect is quantified and its relationship with the overall propulsive performance is examined. Thirdly, a model is developed that adequately explains and illuminates the phenomena. Finally, these phenomena are exploited to develop a new diagnostic tool for investigating transient effects based on antenna current measurements.

The new diagnostic tool is non-intrusive in nature since it relies on antenna current measurements, making it highly suitable for use in flight to aid monitoring and control of the thruster. It is especially compatible with a propellant-flexible thruster because it can be applied to a wide range of propellants. It can be implemented with a sufficiently high sampling frequency to resolve transient effects and it can be operated in real time to support flight hardware.

The combination of diagnostics, modelling approaches and generated results form a powerful resource to understand transient antenna-plasma interactions within a high-power and propellant-flexible inductive plasma thruster. These results are based on existing experimental data that includes various mixtures of oxygen, carbon dioxide, nitrogen and argon at flow rates from 1.66 to 3.74 g/s and input powers from 0.9 to 154.5 kW. Overall, this thesis documents and explains transient antenna-plasma interactions within an inductive plasma thruster. This amounts to the generation of a significant related dataset, associated knowledge and a new diagnostic tool to support the design, development, testing and operation of inductive plasma thrusters.

Declaration

I certify that this work contains no material which has been accepted for the award of any other degree or diploma in my name in any university or other tertiary institution and, to the best of my knowledge and belief, contains no material previously published or written by another person, except where due reference has been made in the text. In addition, I certify that no part of this work will, in the future, be used in a submission in my name for any other degree or diploma in any university or other tertiary institution without the prior approval of the University of Adelaide and where applicable, any partner institution responsible for the joint award of this degree.

I acknowledge that copyright of published works contained within this thesis resides with the copyright holder(s) of those works.

I give permission for the digital version of my thesis to be made available on the web, via the University's digital research repository, the Library Search and also through web search engines, unless permission has been granted by the University to restrict access for a period of time.

I acknowledge the support I have received for my research through the provision of an Australian Government Research Training Program Scholarship.

8 July 2022

Acknowledgements

Firstly, I would like to thank my supervisors: Bassam, Georg and Ashley. When I first met with Bassam in late 2017 to discuss the possibility of undertaking a PhD related to space propulsion, he offered me the choice of conventional rocket engines or electric propulsion. Wanting to test myself, I chose the latter. Despite the challenges of a project that was located somewhere between Adelaide and Stuttgart, I don't regret it. It was Bassam's clear-headed perseverance and focus on the goal that got me to the end.

Georg has been a source of enthusiasm and ideas, deeply-rooted in technical knowledge and experience. The collaboration with IRS in Stuttgart that he facilitated enabled me to work on an exciting electric propulsion project from my home in Adelaide. It's hard to imagine a better balance between work and family life. He encouraged me to think beyond what had already been done.

Ashley's contribution has been invaluable since he joined the project in late 2018. He has acted both literally and metaphorically as an interpreter of all things German and IRS. He gifted me experimental data and ideas that have been crucial to the work in this thesis. Ashley helped me to navigate between the pragmatic and the perfect.

My thanks to Paul for his assistance with completing the project. Financial support for this project was provided by the Australian Government Department of Education, the South Australian Space Industry Centre, and the Sir Ross and Sir Keith Smith Fund. This support is greatly appreciated. In particular, the latter two underwrote trips to Stuttgart in 2019 and 2020 respectively. These trips were not only crucial to the project but also gave me a wealth of personal experiences for which I am grateful.

I appreciate the kindness of the many people at IRS who gave me a warm welcome, and especially Francesco for his useful technical discussions. I would like to thank my colleagues in the University of Adelaide's School of Mechanical Engineering. In particular, Alison-Jane for assisting with editing. Thanks also to my friends and office mates: Araz, Fred, James, James, James and Matt.

Finally, my love and thanks to my family: those who have arrived (Rob, Vivienne, Blythe, Stella and Jasper), those who have departed (Marion) and everyone else.

For Emily and Vivienne.

8 July 2022

Contents

Abstract	v
Declaration	vi
Acknowledgements	vii
Contents	viii
List of figures	x
List of tables	xi
1 Introduction	1
1.1 Background literature	2
1.1.1 Thrusters	2
1.1.2 Propellant-flexible thrusters	4
1.1.3 Inductive plasma thrusters	7
1.1.4 Diagnostic tools	9
1.1.5 Non-intrusive diagnostic tools	10
1.1.6 Modelling inductive plasmas	11
1.1.7 Electrical behaviour of inductive plasma thrusters	12
1.2 Gaps, aim and objectives	14
1.3 Thesis structure	16
References	18
2 Transient behaviour	25
Statement of authorship	26
Abstract	27
2.1 Introduction	27
2.2 Methodology	32
2.2.1 Experimental setup	32
2.2.2 Collation of discharge cycles	37
2.3 Results & discussion	37
2.3.1 Spatially resolved discharge cycles	43
2.4 Conclusion	48
Acknowledgements	51
References	51
3 Power efficiency estimation	57
Statement of authorship	58
Abstract	59
3.1 Introduction	59
3.2 Methodology	63
3.2.1 Experimental setup	63

3.2.2	Measuring inductive coupling	67
3.3	Results & discussion	69
3.3.1	Antenna current	69
3.3.2	Calorimetry	73
3.4	Conclusion	78
	Acknowledgements	81
	References	81
4	Circuit model	87
	Statement of authorship	88
	Abstract	89
4.1	Introduction	89
4.2	Experimental setup	91
4.3	Circuit model	92
4.3.1	Collisionless	97
4.3.2	Collisional	98
4.3.3	Solution method	99
4.4	Results & discussion	102
4.5	Conclusion	109
	Acknowledgements	110
	References	110
4.A	Coil self-inductance calculation	113
4.B	Coil resistance calculation	114
5	Hybrid circuit-chemistry model	117
	Statement of authorship	118
	Abstract	119
5.1	Introduction	119
5.2	Methodology	120
5.2.1	Circuit model	121
5.2.2	Chemistry model	125
5.2.3	Experimental setup	126
5.3	Results & discussion	127
5.4	Conclusion	134
	Acknowledgements	135
	References	135
5.A	BOLSIG+ data	138
6	Summary and conclusion	141
6.1	Future work	142

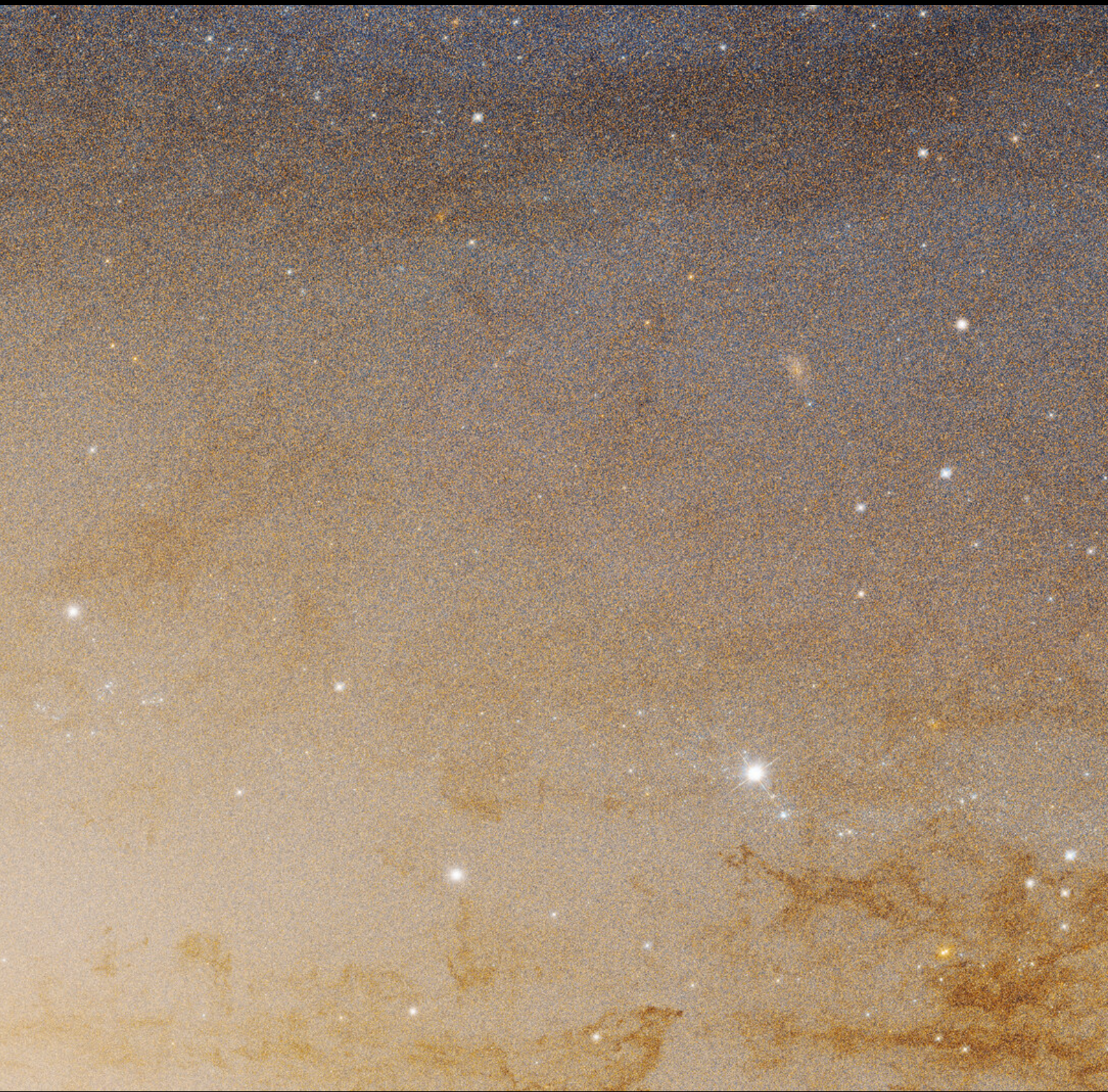
List of figures

1.1	Schematic diagram of a generic radiofrequency thruster	6
1.2	Radial profiles of radiated power for capacitive and inductive regimes	6
1.3	Transformer model of an inductively coupled plasma	13
1.4	IRS inductive plasma resonant circuit	13
2.1	Axial photograph of an inductively-coupled nitrogen plasma	31
2.2	TIHTUS operating principle and test facility	33
2.3	Experimental setup including IPG7	33
2.4	IPG7 resonant circuit	34
2.5	Method used to collate the discharge cycles	37
2.6	Collated discharge cycles for pure nitrogen	40
2.7	Collated discharge cycles for argon-nitrogen	40
2.8	Collated discharge cycles for argon-oxygen	42
2.9	Emission intensity against radial position for pure nitrogen	45
2.10	Radial-temporal distribution of emission intensity for pure nitrogen	45
2.11	Emission intensity against radial position for argon-nitrogen	47
2.12	Radial-temporal distribution of emission intensity for argon-nitrogen	47
2.13	Emission intensity against radial position for argon-oxygen	49
2.14	Radial-temporal distribution of emission intensity for argon-oxygen	49
3.1	TIHTUS operating principle and test facility	64
3.2	Sectional view of IPG7	64
3.3	Resonant circuit	66
3.4	Processing of antenna current measurements	68
3.5	Antenna power causing capacitive–inductive transition	71
3.6	Measures of inductive coupling	72
3.8	Tube and jet calorimetric powers	77
4.1	Resonant circuit	93
4.2	Sectional view of IPG7	95
4.3	Solution space for the model	99
4.4	Model solution method	100
4.5	Plasma power against anode power	101
4.6	Time series of model input parameters	105
4.7	Time series of model output parameters	107

5.1	Sectional view of IPG7	121
5.2	Resonant circuit	122
5.3	Overview of the model	123
5.4	Plasma volume representation	124
5.5	Time series of coil current	129
5.6	Time series of normalised frequency shift	129
5.7	Time series of normalised effective collision frequency	130
5.8	Time series of localised electron fraction and density	130
5.9	Time series of plasma volume	132
5.10	Thermal efficiency against plasma volume	132
5.11	Time series of number of electrons	133

List of tables

2.1	Summary of experimental conditions	35
2.2	Coil conditions at maximum current	42
3.1	Overview of experimental conditions	70
3.2	Summary of results	79
4.1	Summary of model parameters	100
4.2	Summary of experimental conditions	102
4.3	Comparison of parameter extrema	108
5.1	Summary of experimental conditions	127
6.1	Summary of all experimental conditions	143



Introduction

Human exploitation of space is rapidly expanding and evolving. Space is now deeply involved in the lives of individuals, communities and nations through the provisioning of a wide range of services including navigation, communications and meteorology. The monolithic structures of ‘old space’ are fragmenting with the emergence of market competition at the national level and new space powers at the international level. Ubiquitous high-speed internet access through satellite constellations is only the latest disruption. Many more can be expected in the coming decades, as barriers to entry are removed and a greater collective human will and intellect is directed towards space exploitation.

These trends are mirrored by human exploration of space. New, ambitious, international players are emerging. These include China, India, Japan, Germany, France, Israel, Luxembourg and the European Space Agency, who have each sent unmanned spacecraft to other celestial bodies in the past two decades. There are two human presences in space as of 2022: the International Space Station and China’s Tiangong space station. NASA’s Lunar Gateway space station is scheduled for launch in 2024.

Despite this progress, human space capability is still significantly limited in at least one aspect. Since the beginning of the space age, any assets or resources to be used in space were first transported from Earth’s surface. This included the material, such as vehicles, consumables and occupants, and the immaterial, such as power, commands and maintenance. Over time, the immaterial resources have been sourced elsewhere. For example, power has been collected by solar arrays, command of robots has been automatized, and repairs to the ISS have been conducted by its occupants. Nonetheless, the transport of materials from Earth’s surface to stable orbit remains necessary and is the single greatest barrier to the exploitation of space. This costly barrier explains why space exploitation was the domain of the superpowers in the twentieth century. Although the cost has been reduced in recent decades, it remains a significant deterrent.

The use of materials that have not originated from Earth to support space activities has yet to be achieved meaningfully. In the literature, this concept is termed ‘in-situ resource utilisation’ (ISRU). Possible applications of ISRU include the production of drinkable water from Lunar ice, the production of hydrocarbon fuels from carbon

1 Introduction

dioxide and water on Mars, and the construction of shelters from earthworks. The realisation of a self-sustaining population on Mars will require the use of many ISRU concepts.

Of the material resources consumed in space, the most significant is the mass that is expelled by the propulsion system to generate thrust. This mass is called propellant. It is required in large quantities that rapidly scale with the total mass of the spacecraft and it cannot be recycled. Attempting to recycle propellant would annihilate its effect due to the conservation of momentum. If all the vehicle's propellant is sourced from Earth, the rocket equation dictates that propellant mass must grow dramatically as range increases. Propellant derived from ISRU is necessary to unlock deeper exploration into space, such as beyond our solar system, and enable more propellant-intensive operations, such as round trips between Earth and Mars.

The utilisation of ISRU propellant requires both its production, and its consumption by a suitable thruster. Several propellant-flexible thruster technologies have been proposed and are in development. Inductive plasma thrusters are promising candidates given their high level of technical development, propellant compatibility and scalability. Nonetheless, there are still several technical issues that limit the potential of inductive plasma thrusters. In particular, there is a need to develop diagnostic tools that can accommodate various propellants while linking the internal behaviour of the thruster at the 'microscopic' level to its propulsive output at the 'macroscopic' level.

This thesis supports the development of inductive plasma thrusters for propellant-flexible space propulsion by exploring transient interactions between the antenna and the plasma. The following section of this introductory chapter lays out the relevant background literature on the topic. This serves as a broad background for the subsequent chapters, which each have their own bespoke literature reviews. Subsequently, the gaps, aim and objectives are summarised in section 1.2 and the thesis structure is described in section 1.3.

1.1 Background literature

1.1.1 Thrusters

The propulsion system of a spacecraft enables it to change orbit and/or travel between celestial bodies. It consists of one or more thrusters that expel propellant to generate a reaction force. The key distinction between different thrusters is the source of the energy that is used to accelerate the propellant. In chemical propulsion, the energy comes from chemical potential energy stored in the propellant, as in a rocket engine. In electric propulsion, the energy comes from an electric source such as a solar array or batteries, as in an ion thruster.

The chief characteristics of electric propulsion, as opposed to conventional chemical propulsion, are high propellant efficiency due to high effective exit velocity, and low thrust. Launching an object into space from Earth requires a high level of thrust, which is unachievable by electric propulsion both now and in the foreseeable future. Hence this remains the realm of the conventional chemical rocket. Where electric propulsion currently excels is operations in space such as orbit-raising, attitude control and positioning, and long duration manoeuvres. The duration of manoeuvres could be reduced by using a more potent energy source such as nuclear power. Previous studies have explored this idea in the form of a manned Mars mission using nuclear-powered electric propulsion—they found that such a mission is not only plausible, but also favourable when compared with alternatives such as a conventional chemical propulsion mission (T. D. Schmidt et al., 2006; Loeb et al., 2015).

Electric propulsion has historically been the subject of much research and development, with little practical use beyond exploration missions, and technological tests and demonstrations. Since the 1990s, however, the commercial use of electric propulsion has increased dramatically. Lev et al. (2017) analysed the 248 satellites with electric propulsion systems (excluding resistojets) launched during the period between 1993–2016, and the related increase in technological readiness and commercial adoption. Over 70% of them had either gridded ion or Hall-effect thrusters. The majority of those satellites (208) were located in geosynchronous equatorial orbit (GEO) due to a combination of commercial and technical factors. Commercial communication satellites in GEO were the main adopters for two key reasons. Firstly, the satellites have large solar arrays for communications that can be temporarily repurposed for propulsive power when needed; and secondly, they have significant propulsion requirements for orbit-raising and station-keeping, therefore the high efficiency of electric propulsion provides a significant benefit. By contrast, small satellites and low Earth orbit (LEO) satellites have not adopted electric propulsion to the same extent, mainly because they do not have the capacity for large solar arrays to power the systems. Electric propulsion continues to be an excellent match for planetary and interplanetary spacecraft due to their extreme propulsion requirements, and will remain dominant for the foreseeable future.

Electric propulsion technologies can be broadly categorised by the method used to accelerate the propellant: electrothermal, electrostatic, or electromagnetic, or hybrids thereof (Dankanich, 2010). Electrothermal thrusters use electricity to heat the propellant, most commonly through either resistive heating of a heating element (resistojets) or of an electric arc between two electrodes (arcjets) (Wollenhaupt et al., 2018). In both cases, the addition of heat leads to gas-dynamic acceleration through a diverging nozzle. For the remaining two acceleration methods, the propellant must be ionised in order to experience accelerating forces. This may be achieved within the accelerating region or as a separate prior stage. The ionised propellant generally meets the criteria

1 Introduction

of a plasma, hence these devices are also referred to as ‘plasma thrusters’.

An issue common to conventional electric thrusters such as resistojets, ion thrusters and Hall effect thrusters is the exposure of electrical components to the high-enthalpy propellant flow. Propellant selection is a critical design choice for electric propulsion systems and is influenced primarily by mass and reactivity, which leads to the use of noble gases: argon, krypton, and especially xenon (Ahedo, 2011; Brown & Walker, 2020). Xenon is particularly attractive in the case of electrostatic thrusters because its first and second ionisation energies are relatively low and high respectively, hence it is possible to generate many single-charge ions without expending significant energy to generate double-charge ions. Noble gases have the additional benefit of being monatomic, meaning that energy is not expended on dissociation. The resulting erosion necessitates a trade-off between thruster lifetime and propellant choice. This trade-off has been navigated with great success: each of these technologies has been practically applied. Despite this, less constrained propellant choice is an attractive proposition to allow greater flexibility of operation.

The unique advantages of electric propulsion systems make them most suitable for operation over long periods of time. Therefore, the longevity of these systems becomes a critical issue in their design and operation. Erosion and deterioration of electrical components is the main factor due to the combination of voltage, temperature, and chemically-reactive propellants. Electrodeless designs address this by isolating the propellant from the electrical components.

1.1.2 Propellant-flexible thrusters

A propellant-flexible thruster is one which can consume a range of propellants to generate thrust. This is typically achieved by adopting an electrodeless design, because deterioration of exposed electrical components is the main factor that limits propellant choice. A diverse range of potential technologies has been suggested and investigated. In a recent review paper, Bathgate et al. (2017) presented and discussed the operating principles of more than twenty different electrodeless thruster concepts.

An important distinction between different technologies is the acceleration mechanism, in particular whether or not there is an electromagnetic component, because it dictates how the electrical components interact with the propellant. If the acceleration is purely gas-dynamic, then heating of the propellant is required. If electromagnetic acceleration is employed, then this heating must be sufficient to generate the necessary ions. In any case, intense contactless heating of the propellant is required. Contactless heating of a gas can be achieved by putting it in close proximity to an antenna that is excited by a radiofrequency current. A schematic diagram of a generic radiofrequency thruster is shown in figure 1.1. Typically, propellant gas flows through a cylindrical volume which is bounded by a dielectric material, usually a quartz tube. Antennae can

take diverse shapes, and there is a rich literature on optimising antennae shapes for certain applications, although the most common shape is a helical coil. The antenna is positioned such that it encloses the quartz tube and minimises the distance to the propellant gas.

Three distinct power coupling mechanisms have been observed in radiofrequency plasma sources: capacitive, inductive and helicon. In general, these mechanisms are given in order of increasing power and electron density, although there are important exceptions.

Capacitive coupling is caused by the dominance of an axial electric field, which results from the voltage gradient along the length of the coil. The alternating axial electric field generates a corresponding azimuthal magnetic field. The electric field causes electrons in the propellant gas to oscillate, and results in both Ohmic and stochastic heating. Capacitive coupling is associated with low input powers and a weak emission of visible light.

Inductive coupling is caused by the dominance of an axial magnetic field that results from the coil behaving as a solenoid. The alternating axial magnetic field generates a corresponding azimuthal electric field. This azimuthal electric field causes electrons in the propellant gas to oscillate such that they form an induced current. Ohmic and quasi-stochastic heating occur in a thin layer close to the quartz tube with a thickness of δ , known as the skin depth. Inductive coupling is associated with high input powers and a strong emission of visible light in a ring-shaped volume close to the tube wall.

A plasma source that is capable of inductive coupling will typically exhibit capacitive coupling at lower input powers. When the input conditions are sufficiently high, the system will abruptly transition to inductive coupling, which is marked by a bright ring of light. Capacitive and inductive coupling can be distinguished by the radial profile of emitted light, as shown in figure 1.2. Capacitive coupling continues to occur in parallel with inductive coupling (Godyak et al., 2002; Godyak, 2003). Capacitive–inductive transitions have been a topic of great interest since their observation by MacKinnon (1929), primarily because it is desirable to maintain the inductive mode for many practical applications. The necessary conditions for mode transitions were studied by Turner and Lieberman (1999), who showed that an inductive discharge could be maintained at a lower antenna current than the current required to initiate inductive coupling. This hysteresis phenomenon remains a topic of investigation in the literature (Lee & Chung, 2015; Wegner et al., 2016). In terms of a radiofrequency thruster, it is important to understand the mode behaviour because it both determines the amount of power that is coupled into the plasma, and alters the radial profile and therefore the heat transferred to the tube wall.

The third coupling mechanism, called the helicon mode, is not a topic of the thesis but is mentioned here for completeness. The helicon mode is a special case of inductive coupling that is associated with the presence of low frequency whistler waves (Harding

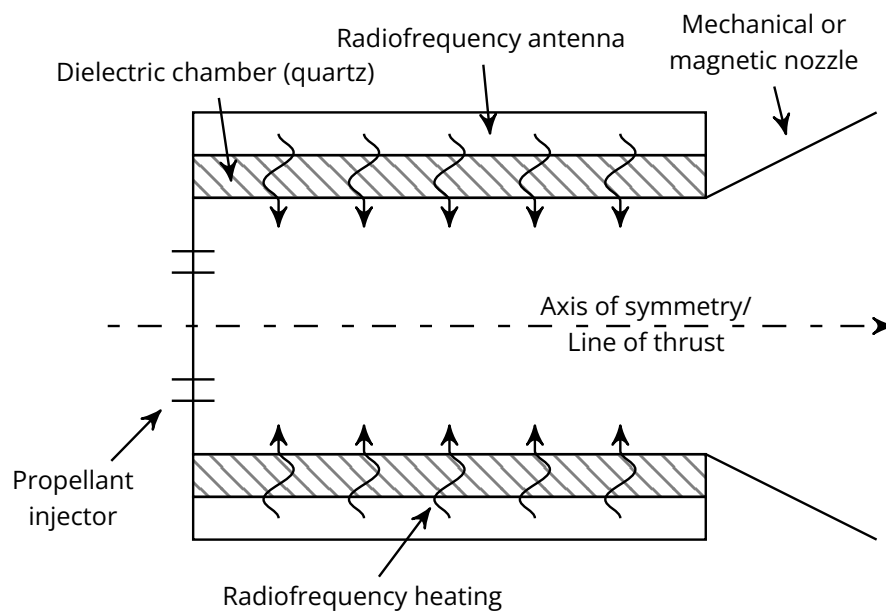


Figure 1.1: Schematic diagram of a generic, axi-symmetric radiofrequency thruster.

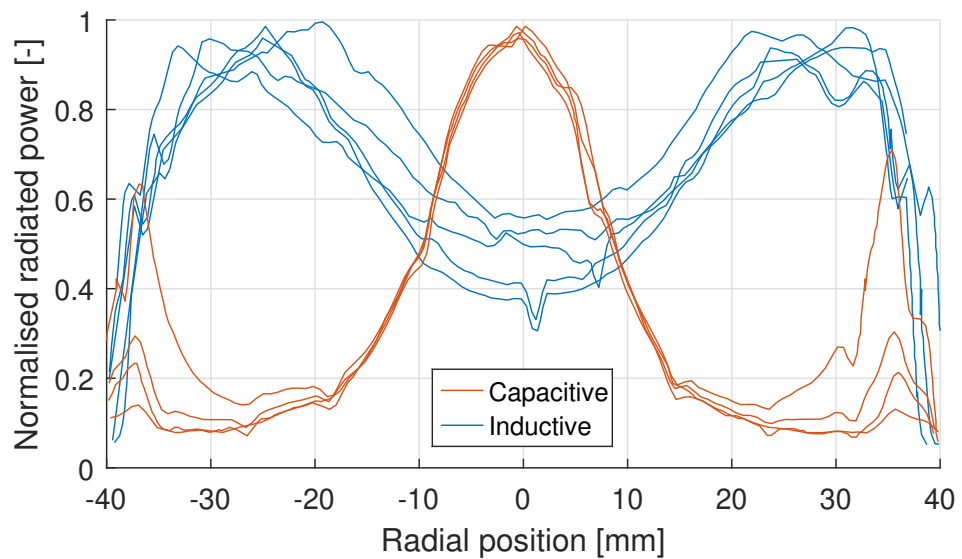


Figure 1.2: Radial profiles of normalised radiated power for capacitive and inductive regimes for an air plasma. The capacitive and inductive profiles were scaled independently. Adapted from Herdrich (2004).

& Thonemann, 1965). It occurs only in the presence of an additional applied magnetic field and is characterised by a higher electron number density (Chen, 2015). The relative merit of thrusters based on helicon plasmas with respect to those based on inductive plasmas is an of ongoing debate (Godyak, 2020; Takahashi et al., 2020).

A variety of propellants are under consideration for propellant-flexible thrusters that can be classed as Earth-originating or ‘in-situ resource utilisation’ (ISRU). The latter can be further divided into those that are collected from the environment and those that are by-products or waste generated within the spacecraft (Charles, 2009). Key ISRU propellants of interest include oxygen, nitrogen, water vapour, carbon dioxide, and syn-gases from waste gasification and pyrolysis processes (Anih et al., 2019). Iodine is an example of a propellant candidate that is not derived from ISRU. It has attractive storage properties and lower cost than the more conventional alternative, xenon. An inductive thruster targeting the microsatellite market that uses iodine propellant is currently in development (Bellomo et al., 2022).

Air breathing electric propulsion (ABEP) is a special case of ISRU electric propulsion in which a satellite in a very low orbit continuously ingests atmospheric material through an intake and accelerates it to generate thrust; this allows a satellite to maintain a very low altitude (typically 150 to 250 km for Earth) that would otherwise be unstable, by offsetting drag with thrust (Vaidya et al., 2022). In such a system, the propellant composition and flow rate are determined by the atmospheric composition and density at the specified altitude. At an altitude of 200 km, a typical ordering of species in Earth’s atmosphere from most abundant to least is atomic oxygen ($3.99 \times 10^{15} \text{ m}^{-3}$), molecular nitrogen ($2.81 \times 10^{15} \text{ m}^{-3}$), molecular oxygen ($1.14 \times 10^{14} \text{ m}^{-3}$), atomic nitrogen ($2.67 \times 10^{13} \text{ m}^{-3}$), helium ($7.41 \times 10^{12} \text{ m}^{-3}$), argon ($2.18 \times 10^{12} \text{ m}^{-3}$) and hydrogen ($1.78 \times 10^{11} \text{ m}^{-3}$) (Romano et al., 2022). Atomic oxygen and molecular nitrogen are the dominant species. A wide range of propellant compositions must be tolerated since the atmospheric composition can vary significantly as a function of time, solar activity, and latitude and longitude.

1.1.3 Inductive plasma thrusters

Recent interest in inductively coupled plasmas as a propulsion technology has led to the ongoing development of numerous inductive and helicon plasma thruster concepts (Sou et al., 2000; Herdrich et al., 2013; Isayama et al., 2018; Navarro-Cavallé et al., 2018; Takahashi, 2019; Vitucci, 2019; Chadwick et al., 2020; Kralkina et al., 2020; Romano et al., 2020; Tsifakis et al., 2020; Bellomo et al., 2022; Romano et al., 2022). At the same time hybrid concepts, such as TIHTUS and VASIMR, have also been developed. TIHTUS (Thermal-Inductive Hybrid Engine of the University of Stuttgart) uses a two-stage approach, with the first being an arcjet and the second being an inductive plasma generator (Böhrk & Auweter-Kurtz, 2006). VASIMR (VARIABLE Specific

1 Introduction

Impulse Magnetoplasma Rocket) uses a helicon first-stage and an ion cyclotron resonance second-stage to couple energy into the plasma efficiently (Giambusso et al., 2017). Although the propellant-flexibility of inductive plasmas is a favourable feature, there has been relatively little work looking at ISRU propellants. Argon is typically used because it is easily ionised, readily available, safe, inexpensive, well-studied and monatomic (has simple chemistry). Molecular propellants and propellant mixtures are, by their nature, more difficult to study due to their complex chemistry. Perhaps the most comprehensive study of ISRU propellants in an inductive plasma thruster was conducted by Chadwick et al. (2020). Oxygen, nitrogen and carbon dioxide were studied with an argon component between 0 to 79 %, as well as pure argon for reference. This study reinforced previous work showing that mixtures of the molecular propellants with argon can produce more favourable propulsion conditions than either compound alone.

Inductively coupled plasmas have well-established uses in various industrial processes, especially silicon wafer etching. In those applications, the input powers are typically low, in the order of Watts. High power inductive plasma applications are less established, and include surface coating, waste treatment and re-entry simulation (Herdrich & Auweter-Kurtz, 2006; Herdrich et al., 2014). For re-entry simulation, an inductive plasma generator may be used as the source for a plasma wind tunnel. These devices operate at input powers in the order of kilowatts.

A useful characteristic of inductive plasma thrusters is their scalability with respect to conventional electric propulsion technologies. Designs can be scaled for low or high power applications. This contrasts with ion thrusters and Hall effect thrusters, which are typically used in clusters for high-power applications, increasing the design complexity and redundant mass. Despite this scalability, most research efforts on inductive plasmas thrusters have focused on low power devices. There are three primary reasons for this trend. Firstly, there are practical concerns related to budgets and the reuse of facilities and equipment that are suited for low power sources. Secondly, existing technical knowledge can be carried over from the extensively studied low power devices. Thirdly, low powered thrusters are more likely to find a market and application under current business trends.

Despite the several strong motivations to investigate low power inductive plasma thrusters, it is nonetheless important to simultaneously develop high power thrusters to target different applications: for example, nuclear-powered interplanetary travel. The application of existing knowledge to high power inductive plasma thrusters is hindered by three key issues. Firstly, the larger scale (geometry, input power and flow rate) means that different physical processes become important, for example, the thermal boundary layer. Secondly, the use of complex propellants has been understudied. Thirdly, high power inductive plasmas have not been extensively studied with respect to the need to maximise propulsion characteristics.

1.1.4 Diagnostic tools

It is important to measure the system-level characteristics of a thruster accurately, such as thrust, efficiencies, propellant utilisation, effective exhaust velocity and thrust-to-weight ratio. These figures of merit quantify the ‘macroscopic’ performance of the thruster. Many of these figures require an accurate measurement of thrust.

Thrust is measured most directly by a thrust stand, where the thruster is attached to a platform that is fixed in place via load cells. The load cells directly measure the reaction force generated by the thruster. For electric propulsion, thrust stands can be problematic because the measured thrust is very small and the thruster must be connected to a vacuum tank, propellant supply and electric supply. An alternative method for measuring thrust is a baffle plate (Böhrk & Auweter-Kurtz, 2009). A plate is placed in the vacuum chamber and fixed in place via load cells. The plume generated by the thruster collides with the plate, which depletes its axial momentum. The force required to keep the plate from moving is an analogue of the thrust force.

An energy-balance analysis of the system can be achieved by considering the various pathways for energy to enter or exit, and measuring or estimating each of these. Calorimetry represents a powerful tool for estimating heat rates. As it applies to electric propulsion diagnostics, calorimetric measurements are achieved by using a closed loop of circulating fluid, usually water, to cool a component. Direct measurement of temperatures and flow rates, in conjunction with knowledge of the specific heat capacity of the fluid, allows one to calculate the heat rate. In addition to estimating heat rates, this kind of arrangement also provides the benefit of cooling components that are prone to overheating. Multiple calorimetric loops can be used to observe multiple heat rates. In this way, it is possible to build up an energy-balance analysis of a propulsion system, so long as the steady state assumption is satisfied. In practice, however, this approach is limited by the inherent inaccuracies of calorimetry as well as various unmeasurable heat pathways such as the interface between the propulsion device and the vacuum tank, convection of the ambient air, and black body radiation.

Calorimetry may also be applied to the exhaust plume of a propulsion device via a cavity calorimeter. A cavity calorimeter is a cup-like water-cooled device that is designed to maximise heat transfer from the plume to the cooling water, for the purpose of calorimetric measurements. These devices have been used extensively for electric propulsion diagnostics since they are effective at directly measuring the enthalpy in the plasma plume. They have been successfully developed for high-power (kilowatt range) inductive plasma sources with an overall accuracy of approximately 10% (Herdrich et al., 2002). A significant characteristic of the baffle plate and cavity calorimeter approaches is that they interfere with the plume, hence they disturb the operating conditions of the thruster, for example, by generating back pressure in the tube. For obvious reasons, they cannot be used in-flight.

1 Introduction

The Langmuir probe is a key plasma diagnostic tool because it can directly measure the electrical characteristics of a localised region of plasma. In its simplest form, it is a probe made of thin wire that is inserted into the plasma volume. It is held at a certain potential with respect to ground while the current is measured. Controlling the potential of the wire with respect to the plasma itself allows one to control whether the current is a positive current related to electrons, or a negative current related to positive ions (Lieberman & Lichtenberg, 2005). By sweeping the potential, a current-voltage curve can be determined that can be used to calculate various plasma properties depending on the electron distribution (Chen, 2016). A wide range of devices and techniques have been developed from this simple concept in order to compensate for a variety of factors and extract the most information about the plasma conditions, including oscillating bias potential and multiple electrode arrangements. It is the most typical plasma diagnostic device due to its long history and relatively simple operating principle (J. Schmidt et al., 2018). However, its intrusive nature means that the presence of the probe disturbs the plasma conditions that are being measured. While the highly-localised nature of the measurements is useful for some applications, it does present problems for characterising a large plasma volume, especially one with significant temporal and spatial variation. High-power radiofrequency plasmas present a difficult environment for obtaining experimental measurements due to the high temperature and radiofrequency power, and the need to avoid disturbing the conditions inside the chamber.

1.1.5 Non-intrusive diagnostic tools

Inductive plasmas generally emit strong radiation due to various state changes and associated emission bands. For many species of interest, many of these bands are in the visible range. Several diagnostic tools rely on this fact to assess the plasma non-intrusively. By their nature, these tools require optical access to the plasma and will integrate the plasma properties along the line of sight.

Optical emission spectroscopy (OES) is a well-developed non-intrusive plasma diagnostic tool that relies on the identification of emission bands in conjunction with a detailed chemistry and radiative model. Since the emission bands are generated by state changes, they are associated with reaction rates rather than species populations. Therefore, to derive the species populations it is necessary to consider a number of reactions (emission bands) and acquire an independent reference number, for example, the electron number density, to generate absolute numbers.

Other non-intrusive techniques involve passing a laser beam through the plasma volume through transparent openings that are designed for this purpose. Since the laser passes through a linear volume of plasma, any measured value will be an integral of this volume. However, by sweeping the laser through the plasma cross-section, and performing analysis with the inverse Abel transformation, it is possible to extract the

radial profiles of the measured values. An example of such a value is the electron density obtained via a Mach–Zehnder interferometer. The device uses the change in the refractive index due to the presence of electrons (Chan et al., 2018). Another example is the plasma translational temperature and number density, as determined by laser absorption spectroscopy (Mayer et al., 2016). Fitting of emission spectra has also been demonstrated to determine radially-resolved number densities, and vibrational and rotational temperatures (Burghaus et al., 2021).

An important complicating factor for diagnostic tools is the need to assess transient phenomena. This is especially problematic for non-intrusive techniques because they typically rely on taking observations that are longer in duration than the transient phenomena and treat the system as steady state. It is possible to observe transient effects by performing a temporally-resolved optical emission spectroscopy, called in the literature phase-resolved optical emission spectroscopy or PROES (Schulze et al., 2010).

1.1.6 Modelling inductive plasmas

Modelling is an important approach that can be used in conjunction with diagnostic tools. In order to capture the behaviour of a radiofrequency plasma, there are three main phenomena which must be considered: antenna-plasma coupling, wave propagation, and plasma transport. A number of analytical models have been developed; however, they are very specific in nature owing to simplifying assumptions, and their initial and boundary conditions. Numerical models are more general and work by computing governing equations for a finite number of elements. In the extreme case, these elements correspond to the chemical species present in the plasma, and the model would be better described as a simulation. This approach is generally not practical for plasma sources above a certain size due to the number of calculations required. Therefore, a number of methods for discretising the problem have been developed, with the aim of reducing the number of elements as much as possible, while retaining physically accurate solutions. Despite the high fidelity that can be achieved via numerical models, they have not replaced analytical models. Analytical models are particularly suited for investigating trends to develop intuitive understanding of a system and inform engineering decisions.

The transformer model is perhaps the most universally applicable analytical model for inductive plasmas. The antenna-plasma system is considered as an air-core electrical transformer, resulting in an intuitive zero-dimensional (or integral) model for inductively coupled plasmas. The inductive coil is the primary winding and the plasma is the secondary, one-turn winding. Together, they form the circuit diagram shown in figure 1.3 where power is inductively transferred from the coil to the plasma with losses. Analysis of this circuit yields an analytical solution for the unknowns: the coupling coefficient, k , and the secondary winding (plasma) inductance, L_2 . The model has been

1 Introduction

employed widely in the literature in the context of inductively coupled plasmas for the semi-conductor industry. Chabert and Braithwaite (2011) provided a more recent review of the transformer model, concluding generally that the model is appropriate for high electron density but may fail at low and intermediate electron density.

An important consequence of the transformer model is an appreciation that the antenna and plasma form a coupled system. From the perspective of the power supply, the plasma can be seen as a complex impedance that is determined by the plasma properties. Cunge et al. (1999) showed that, when transitioning from capacitive to inductive coupling, the current drawn may either increase or decrease, depending on the power supply configuration. That is, there is a complex interconnection between the power circuit and the antenna-plasma system. El-Fayoumi and Jones (1998) were able to link plasma properties to transformer model circuit elements analytically for their planar-coil inductive source. Although they were not able to make direct numerical comparisons with experimental results, they nonetheless showed good agreement in terms of trends and magnitudes. The resonant frequency of the circuit is another important factor. Generally, it is favourable to match the excitation frequency with the resonant frequency of the circuit, where the former is determined by power supply conditions and the latter is a property of the circuit that changes as the plasma impedance changes. Nishida et al. (2014) used the transformer model approach to estimate resonant frequency, which had good agreement with experimental results.

1.1.7 Electrical behaviour of inductive plasma thrusters

One way to avoid the problem of matching the driving frequency with the resonant frequency of the circuit is to use a resonant circuit to generate the oscillating current. For example, an Armstrong/Meissner oscillating circuit uses a capacitor, an inductor and a vacuum tube to generate oscillating current from a DC source. The frequency of the oscillations is the resonant frequency of the circuit, determined by the capacitor and inductor. This is a common technique for high power inductive heating in industrial applications.

The resonant circuit approach was used in the design of the inductive plasma generators, known as IPGs, for the plasma wind tunnel facilities of the Institute for Space Systems (IRS), University of Stuttgart, Germany (Auweter-Kurtz & Wegmann, 1999; Herdrich, 2004; Herdrich & Petkow, 2008; Loehle et al., 2022). Shown in figure 1.4, the resonant circuit consists of a high power triode vacuum tube, a switchable capacitor bank, and inductance provided by the coil. The frequency may be altered by switching the effective capacitance by connecting or disconnecting individual capacitors and/or the effective inductance by using coils with various numbers of turns. In addition to re-entry simulation, IPGs have been developed in parallel as a propellant-flexible thruster technology. The two-stage thruster TIHTUS consists of a first-stage arcjet and

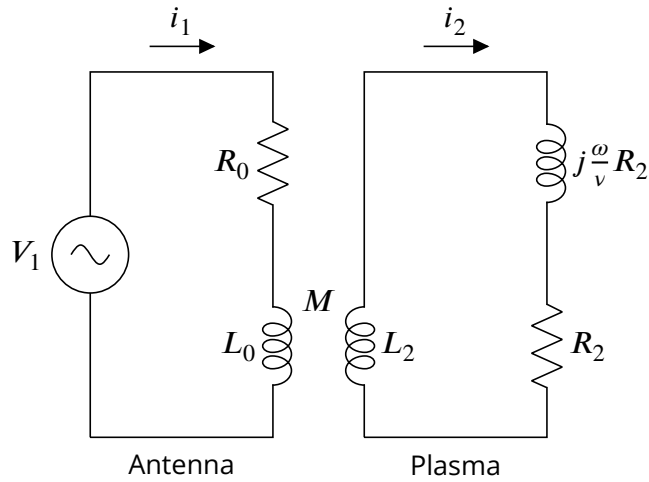


Figure 1.3: Transformer model of an inductively coupled plasma source. A sinusoidal radiofrequency voltage V_1 is fed to an induction coil with inductance L_0 , and resistance R_0 . The coil forms the primary winding of an air-core transformer, where the plasma forms the one-turn secondary winding. The plasma has a resistance R_2 , and an inductance which consists of a component coupled to the plasma L_2 , and a component related to electron inertia, $j(\omega/\nu)R_2$. M is the mutual inductance. Adapted from Piejak et al. (1992).

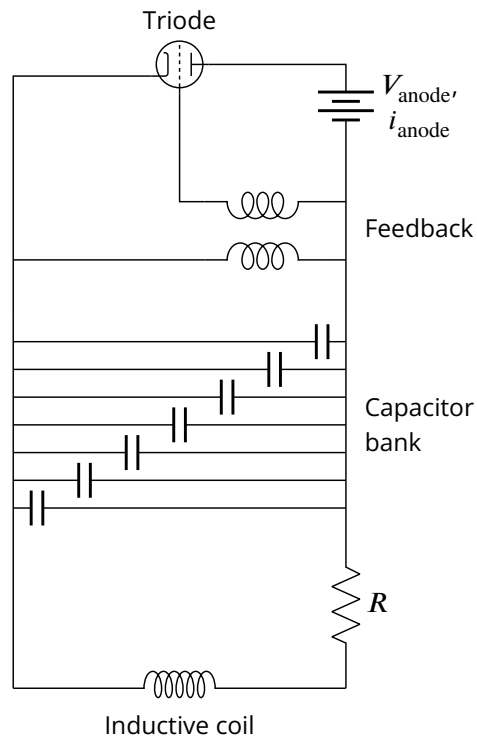


Figure 1.4: Simplified diagram of the resonant circuit that drives the inductive plasma generators of IRS. Adapted from Auweter-Kurtz and Wegmann (1999).

1 Introduction

a second-stage IPG. The arcjet is used to heat a conventional propellant such as argon, which is then mixed with another propellant before undergoing inductive heating in the second stage. In this sense the thruster is partially propellant-flexible. The TIHTUS facility provides for investigations of the IPG stage independently, or, in other words, as a standalone inductive plasma thruster.

If the antenna current of an IPG is measured with sufficient sampling frequency, one can observe that the amplitude of the oscillating signal is not constant, but rather varies at the timescale of 300 Hz. This is related to the incomplete smoothing of the full-bridge rectified three-phase 50 Hz facility power. This quasi-DC source essentially modulates the antenna current. Herdrich (2004) first documented that this modulation takes distinct forms, depending on the IPG operating conditions. In particular, low power conditions are distinct from high power conditions. Besides documenting this observation, that work did not contain analysis of the transient current phenomena, but rather dealt with root-mean-square values.

Later, Chadwick et al. (2016) comprehensively studied these phenomena from a transient perspective. They showed that the shape of the modulation corresponded to the operating mode with the capacitive, low inductive, and high inductive modes each having distinct current profiles. Furthermore, short-time Fourier transform analysis was used to show that the excitation frequency was varying simultaneously. This work showed that transitions between capacitive and inductive coupling were occurring at the 300 Hz timescale. In other words, by observing both the envelope and the frequency of the measured current at the 300 Hz timescale, one can qualitatively assess the coupling behaviour of the antenna-plasma system. This is especially significant because the antenna current is easily obtained through non-intrusive means. Hence, Chadwick et al. (2016) showed that it may be possible to non-intrusively assess transient phenomena related to the antenna-plasma interaction through analysis of the antenna current, although, development of a comprehensive explanation of the phenomena and quantitative relationships is yet to be achieved.

1.2 Gaps, aim and objectives

The background literature presented in the previous section exposed several gaps in the literature on inductive plasma thrusters. Although there are several groups developing the technology, there are two key aspects that remain understudied. Those are the use of alternative propellants and mixtures, and the operation of high power thrusters. The former relates to the exploitation of the propellant-flexible aspect of inductive plasma thrusters, to permit the use of ISRU propellants. The latter relates to the scalable aspect, to enable high power applications such as crewed missions.

The combination of high powers and diverse propellants necessitates the develop-

ment of new diagnostic tools. In particular, there is a lack of diagnostic tools that are non-intrusive and can tolerate diverse propellant chemistries and mixtures. At the same time, there is mounting evidence that suggests a strong link between the transient behaviour of the antenna current and that of the plasma, within an inductive plasma thruster. An explanation of these transient antenna-plasma interactions is needed to support the monitoring and control of inductive plasma thrusters. Furthermore, a theoretical understanding of these interactions may lead to a new diagnostic tool that is non-intrusive and can be applied to diverse propellants.

The overall aim of this thesis is the advancement of inductive plasma thrusters as a propellant-flexible space propulsion technology, through investigations of transient interactions between the antenna and the plasma, leading to the development of a new diagnostic tool. This aim is achieved through the following objectives.

1. Investigate the transient behaviour of the inductive plasma thruster. The transient behaviour of the antenna current has been observed and documented previously (Herdrich, 2004; Chadwick et al., 2016). However, the mechanism driving this behaviour was not clear. In particular, whether or not the periodic variation of the antenna current is related to a periodic variation of the internal state of the plasma; and, if they are related, what is the causal nature of this relationship. Diverse propellants will be considered to investigate the role that the propellant plays in the transient phenomena. Multiple measurement techniques will be used to confirm that these phenomena are observable through different mechanisms and not simply an artifact of the particular technique that was used in the first investigations.
2. Investigate the relationship between antenna current observations and the thermal efficiency of the thruster. The thermal efficiency of a thruster is an important figure of merit for its operation. Laboratory measurements of the thermal efficiency show significant variance when operating conditions are changed, for example, input power and propellant species. Those measurement techniques are intrusive in nature and therefore not suitable for use in flight. As a result, there is a strong use-case for a technique that infers the thermal efficiency from antenna current measurements, which are easily obtained. As an initial step to developing such a technique it is necessary to first establish whether the antenna current has a predictive relationship with the thermal efficiency.
3. Develop a quantitative relationship between antenna current observations and the time-varying properties of an inductive plasma. The previous two objectives establish qualitative relationships; however, the establishment of a quantitative relationship would enable non-intrusive and time-resolved measurements of the plasma properties. This has important implications for monitoring and control

1 Introduction

of a thruster in-flight. Furthermore, the development of a robust quantitative relationship supports the theoretical understanding of why the observed antenna current variations occur.

4. Use the developed quantitative relationship to understand the differences between various input conditions, particularly different propellant species. Understanding the relative performance of different propellant species is necessary to assess the feasibility of different operating concepts. For example, both oxygen and argon can be used as propellants in an inductive plasma thruster, but oxygen is much more abundant. A mixture of argon and oxygen can produce better performance than oxygen alone under the same input conditions, although the mechanisms behind this are not well understood (Chadwick et al., 2020). Understanding these mechanisms can support the selection of particular mixture ratios for particular operating conditions.
5. Develop a new diagnostic tool for inductive plasma thrusters based on antenna current observations. The previous objectives incrementally build the necessary foundation for a new diagnostic tool that is non-intrusive and capable of resolving transient phenomena. Since the tool is non-intrusive, it is relatively simple to implement alongside other experimental techniques, which may not themselves reveal transient phenomena. Hence, it becomes possible to investigate the relationship between transient phenomena and, for example, thermal efficiency. In principle, such a tool could be implemented in real-time in flight hardware for monitoring and control, since it is non-intrusive and requires minimal computational resources. Furthermore, it is not necessary to know the chemical composition of the propellant, which may be useful for applications including in-situ resource utilisation.

1.3 Thesis structure

The main part of the thesis is composed of chapters 2 to 5, each of which contains a reproduced journal article. The first three articles have been peer-reviewed and published in high-ranking journals. The fourth article has been submitted to a high-ranking journal and is currently under peer-review at time of writing. Preceding each article is an introduction that explains the article's relevance to the thesis, and a statement of authorship that explains each co-author's contribution to the article. The articles have been reformatted to form a cohesive thesis and to comply with relevant publication agreements. The changes include the referencing system, and the appearance and layout of text, figures and tables. No changes have been made that alter the meaning of

the text. Each article contains its own literature review and reference list. The chapters are briefly summarised as follows.

Chapter 1, *Introduction*, introduces the thesis and provides the motivation and necessary background context for the following chapters.

Chapter 2, *Transient behaviour*, contains investigations of the transient phenomena in an inductive plasma thruster, addressing objective 1. It reports on experiments involving the simultaneous measurement of antenna current, visible light emission and magnetic field strength. Pure nitrogen, argon-nitrogen, and argon-oxygen plasmas are investigated under low and high input powers. This chapter builds on objective 5 by establishing that the periodic variation of the antenna current is related to a periodic variation of the plasma state, hence it may be possible to infer one from the other.

Chapter 3, *Power efficiency estimation*, contains a more detailed study of the antenna current in particular, how it can be quantified as a proxy for inductive coupling, and how that relates to system-level figures of merit such as thermal efficiency, addressing objective 2. Importantly, it links ‘microscopic’ behaviour (transient antenna current) to ‘macroscopic’ behaviour (thermal efficiency). Pure oxygen, pure carbon dioxide, and mixtures of both with argon are investigated at various flow rates, mixture ratios and input powers. This chapter builds on objective 5 by establishing that the antenna current as a proxy for inductive coupling is linked to system-level behaviour.

Chapter 4, *Circuit model*, presents a new diagnostic tool for estimating the time-varying properties of an inductive plasma from measurements of the antenna current. A circuit model of the resonant circuit and coupled antenna-plasma system is used to infer the plasma effective impedance from the antenna current, and the plasma properties from the impedance. This forms a quantitative relationship between the antenna current observations and the plasma properties, addressing objective 3. The antenna-plasma system is modelled as a transformer. Results of this technique applied to pure oxygen plasmas at two different flow rates and various input powers are presented. This chapter partially achieves objective 5 through the creation of a new diagnostic tool, which is expanded further in the following chapter.

Chapter 5, *Hybrid circuit–chemistry model*, contains a comparison of oxygen and oxygen-argon plasmas based on the antenna current diagnostic tool, addressing objective 4. To facilitate this comparison, the circuit model is augmented with a simple chemistry model. The hybrid circuit–chemistry model enables the estimation of the time-varying effective collision frequency and electron number density. This chapter completes objective 5 by providing the complete diagnostic tool.

Chapter 6, *Summary and conclusion*, concludes the thesis. It provides a brief summary, key conclusions and suggestions for future work.

References

- Ahedo, E. (2011). Plasmas for space propulsion. *Plasma Physics and Controlled Fusion*, 53(12), 1–18. <https://doi.org/10.1088/0741-3335/53/12/124037>
- Anih, S., Pagan, A. S., Koch, H., Martinez, P., Laufer, R., & Herdrich, G. (2019). Waste for Energy and Volume Recovery (WEVR) using Inductively Heated Plasma Generator Samuel. *70th International Astronautical Congress*, IAC–19–B3, 7, 8, x54017.
- Auweter-Kurtz, M., & Wegmann, T. (1999). Overview of IRS plasma wind tunnel facilities. *RTO AVT Course on "Measurement Techniques for High Enthalpy and Plasma Flows"*.
- Bathgate, S. N., Bilek, M. M., & McKenzie, D. R. (2017). Electrodeless plasma thrusters for spacecraft: A review. *Plasma Science and Technology*, 19(8). <https://doi.org/10.1088/2058-6272/aa71fe>
- Bellomo, N., Magarotto, M., Manente, M., Trezzolani, F., Mantellato, R., Cappellini, L., Paulon, D., Selmo, A., Scalzi, D., Minute, M., Duzzi, M., Barbato, A., Schiavon, A., Di Fede, S., Souhair, N., De Carlo, P., Barato, F., Milza, F., Toson, E., & Pavarin, D. (2022). Design and In-orbit Demonstration of REGULUS, an Iodine electric propulsion system. *CEAS Space Journal*, 14(1), 79–90. <https://doi.org/10.1007/s12567-021-00374-4>
- Böhrk, H., & Auweter-Kurtz, M. (2006). Preliminary Results of TIHTUS Operation. *42nd AIAA/ASME/SAE/ASEE Joint Propulsion Conference & Exhibit*, AIAA 2006–5158. <https://doi.org/10.2514/6.2006-5158>
- Böhrk, H., & Auweter-Kurtz, M. (2009). Thrust Measurement of the Hybrid Electric Thruster TIHTUS by a Baffle Plate. *Journal of Propulsion and Power*, 25(3), 729–736. <https://doi.org/10.2514/1.34324>
- Brown, N. P., & Walker, M. L. (2020). Review of plasma-induced hall thruster erosion. *Applied Sciences (Switzerland)*, 10(11). <https://doi.org/10.3390/app10113775>
- Burghaus, H., Herdrich, G., & Fasoulas, S. (2021). Derivation of species distribution in inductively heated CO₂ plasma via automated spectral fitting. *Vacuum*, 184(August 2020), 109901. <https://doi.org/10.1016/j.vacuum.2020.109901>
- Chabert, P., & Braithwaite, N. (2011). *Physics of radio-frequency plasmas* (Vol. 9780521763). <https://doi.org/10.1017/CBO9780511974342>
- Chadwick, A. R., Dally, B. B., Herdrich, G., & Kim, M. (2020). High-power inductive electric propulsion operation with alternative propellants. *The Aeronautical Journal*, 124(1272), 151–169. <https://doi.org/10.1017/aer.2019.141>
- Chadwick, A. R., Herdrich, G., Kim, M., & Dally, B. B. (2016). Transient electromagnetic behaviour in inductive oxygen and argon-oxygen plasmas. *Plasma Sources Science and Technology*, 25(6). <https://doi.org/10.1088/0963-0252/25/6/065025>

- Chan, Y., Boxberger, A., Herdrich, G., Soga, R., & Tanaka, S. (2018). Development , Set-up and Implementing of a Mach-Zehnder Interferometer for Plasma Diagnostics Development , Set-up and Implementing of a Mach-Zehnder Interferometer for Plasma Diagnostics. *Space Propulsion Conference 2018*, (May).
- Charles, C. (2009). Plasmas for spacecraft propulsion. *Journal of Physics D: Applied Physics*, 42(16). <https://doi.org/10.1088/0022-3727/42/16/163001>
- Chen, F. F. (2015). Helicon discharges and sources: A review. *Plasma Sources Science and Technology*, 24(1), 14001. <https://doi.org/10.1088/0963-0252/24/1/014001>
- Chen, F. F. (2016). *Introduction to Plasma Physics and Controlled Fusion* (3rd ed.). Springer International Publishing. <https://doi.org/10.1007/978-3-319-22309-4>
- Cunge, G., Crowley, B., Vender, D., & Turner, M. M. (1999). Characterization of the E to H transition in a pulsed inductively coupled plasma discharge with internal coil geometry: bi-stability and hysteresis. *Plasma Sources Science and Technology*, 8(4), 576–586. <https://doi.org/10.1088/0963-0252/8/4/309>
- Dankanich, J. W. (2010). Low-thrust Propulsion Technologies, Mission Design, and Application. In T. T. Arif (Ed.), *Aerospace technologies advancements* (pp. 219–240). <https://doi.org/10.5772/32009>
- El-Fayoumi, I. M., & Jones, I. R. (1998). The electromagnetic basis of the transformer model for an inductively coupled RF plasma source. *Plasma Sources Science and Technology*, 7(2), 179–185. <https://doi.org/10.1088/0963-0252/7/2/012>
- Giambusso, M., Carter, M. D., Squire, J. P., Chang Diaz, F., Dean, L., Corrigan, A., McCaskill, G., Glover, T., Castro, J., & Del Valle, J. (2017). Progress in the VASIMR VX-200SS Plasma Testing Program. *53rd AIAA/SAE/ASEE Joint Propulsion Conference*, (July), 10–12. <https://doi.org/10.2514/6.2017-4630>
- Godyak, V. A. (2003). Plasma phenomena in inductive discharges. *Plasma Physics and Controlled Fusion*, 45(12A), A399–A424. <https://doi.org/10.1088/0741-3335/45/12A/026>
- Godyak, V. A. (2020). On helicon thrusters: Will they ever fly? *Journal of Applied Physics*, 127(10). <https://doi.org/10.1063/1.5139998>
- Godyak, V. A., Piejak, R. B., & Alexandrovich, B. M. (2002). Electron energy distribution function measurements and plasma parameters in inductively coupled argon plasma. *Plasma Sources Science and Technology*, 11(4), 525–543. <https://doi.org/10.1088/0963-0252/11/4/320>
- Harding, G. N., & Thonemann, P. C. (1965). A study of helicon waves in indium. *Proceedings of the Physical Society*, 85(2), 317–328. <https://doi.org/10.1088/0370-1328/85/2/313>
- Herdrich, G. (2004). *Construction, qualification and characterisation of an inductively heated plasma wind-tunnel system to simulate atmospheric entry (Aufbau, Qual-*

- ifikation und Charakterisierung einer induktiv beheizten Plasmawindkanalanlage zur Simulation atmosphärischer*) (Ph.D. Thesis). Universität Stuttgart.
- Herdrich, G., Auweter-Kurtz, M., Kurtz, H. L., Laux, T., & Winter, M. (2002). Operational behavior of inductively heated plasma source IPG3 for entry simulations. *Journal of Thermophysics and Heat Transfer*, 16(3), 440–449. <https://doi.org/10.2514/2.6698>
- Herdrich, G., & Auweter-Kurtz, M. (2006). Inductively heated plasma sources for technical applications. *Vacuum*, 80(11-12), 1138–1143. <https://doi.org/10.1016/j.vacuum.2006.01.044>
- Herdrich, G., Bauder, U., Boxberger, A., Gabrielli, R. A., Lau, M., Petkow, D., Pfeiffer, M., Syring, C., & Fasoulas, S. (2013). Advanced plasma (propulsion) concepts at IRS. *Vacuum*, 88(1), 36–41. <https://doi.org/10.1016/j.vacuum.2012.02.032>
- Herdrich, G., & Petkow, D. (2008). High-enthalpy, water-cooled and thin-walled ICP sources characterization and MHD optimization. *Journal of Plasma Physics*, 74(3), 391–429. <https://doi.org/10.1017/S0022377807006927>
- Herdrich, G., Schmalzriedt, S., Laufer, R., Dropmann, M., & Gabrielli, R. (2014). Inductively heated plasma waste treatment for energy recovery. *Environmental Technology*, 35(13), 1611–1617. <https://doi.org/10.1080/09593330.2013.875066>
- Isayama, S., Shinohara, S., & Hada, T. (2018). Review of helicon high-density plasma: Production mechanism and plasma/wave characteristics. *Plasma and Fusion Research*, 13, 1–27. <https://doi.org/10.1585/PFR.13.1101014>
- Kralkina, E. A., Nekliudova, P., Pavlov, V., Vavilin, K., Zadiriev, I., & Zhao, C. (2020). Experimental study of a low-pressure hybrid RF discharge. *Plasma Science and Technology*, 22(5), 055405. <https://doi.org/10.1088/2058-6272/ab69bd>
- Lee, H.-C., & Chung, C.-W. (2015). Effect of Electron Energy Distribution on the Hysteresis of Plasma Discharge: Theory, Experiment and Modeling. *Scientific Reports*, 5(1), 15254. <https://doi.org/10.1038/srep15254>
- Lev, D., Myers, R. M., Lemmer, K. M., Kolbeck, J., Keidar, M., Koizumi, H., Yu, D., Schoenherr, T., Gonzalez, J., Choe, W., Albertoni, R., & Hart, W. (2017). The Technological and Commercial Expansion of Electric Propulsion in the Past 24 Years. *The 35th International Electric Propulsion Conference*, (October), IEPC–2017–242.
- Lieberman, M. A., & Lichtenberg, A. J. (2005). *Principles of Plasma Discharges and Materials Processing*. John Wiley & Sons, Inc. <https://doi.org/10.1002/0471724254>
- Loeb, H., Petukhov, V., Popov, G., & Mogulkin, A. (2015). A realistic concept of a manned Mars mission with nuclear–electric propulsion. *Acta Astronautica*, 116, 299–306. <https://doi.org/10.1016/j.actaastro.2015.07.019>

- Loehle, S., Zander, F., Eberhart, M., Hermann, T., Meindl, A., Massuti-Ballester, B., Leiser, D., Hufgard, F., Pagan, A. S., Herdrich, G., & Fasoulas, S. (2022). Assessment of high enthalpy flow conditions for re-entry aerothermodynamics in the plasma wind tunnel facilities at IRS. *CEAS Space Journal*, *14*(2), 395–406. <https://doi.org/10.1007/s12567-021-00396-y>
- MacKinnon, K. A. (1929). On the origin of the electrodeless discharge. *The London, Edinburgh, and Dublin Philosophical Magazine and Journal of Science*, *8*(52), 605–616. <https://doi.org/10.1080/14786441108564921>
- Mayer, T. S., Massuti-Ballester, B., Herdrich, G., & Fasoulas, S. (2016). Characterization of High-Enthalpy and non-Equilibrium Flows using Laser Absorption Spectroscopy. *46th AIAA Thermophysics Conference*, (June), 1–9. <https://doi.org/10.2514/6.2016-3692>
- Navarro-Cavallé, J., Wijnen, M., Fajardo, P., & Ahedo, E. (2018). Experimental characterization of a 1 kW Helicon Plasma Thruster. *Vacuum*, *149*, 69–73. <https://doi.org/10.1016/j.vacuum.2017.11.036>
- Nishida, K., Mochizuki, S., Ohta, M., Yasumoto, M., Lettry, J., Mattei, S., & Hatayama, A. (2014). Equivalent circuit of radio frequency-plasma with the transformer model. *Review of Scientific Instruments*, *85*(2), 4–7. <https://doi.org/10.1063/1.4832060>
- Piejak, R. B., Godyak, V. A., & Alexandrovich, B. M. (1992). A simple analysis of an inductive RF discharge. *Plasma Sources Science and Technology*, *1*(3), 179–186. <https://doi.org/10.1088/0963-0252/1/3/006>
- Romano, F., Chan, Y.-A., Herdrich, G., Traub, C., Fasoulas, S., Roberts, P., Smith, K., Edmondson, S., Haigh, S., Crisp, N., Oiko, V., Worrall, S., Livadiotti, S., Huyton, C., Sinpetru, L., Straker, A., Becedas, J., Domínguez, R., González, D., ... Heißerer, B. (2020). RF Helicon-based Inductive Plasma Thruster (IPT) Design for an Atmosphere-Breathing Electric Propulsion system (ABEP). *Acta Astronautica*, *176*(January), 476–483. <https://doi.org/10.1016/j.actastro.2020.07.008>
- Romano, F., Herdrich, G., Chan, Y. A., Crisp, N. H., Roberts, P. C., Holmes, B. E., Edmondson, S., Haigh, S., Macario-Rojas, A., Oiko, V. T., Sinpetru, L. A., Smith, K., Becedas, J., Sullioti-Linner, V., Bisgaard, M., Christensen, S., Hanessian, V., Jensen, T. K., Nielsen, J., ... Villain, R. (2022). Design of an intake and a thruster for an atmosphere-breathing electric propulsion system. *CEAS Space Journal*, (0123456789). <https://doi.org/10.1007/s12567-022-00452-1>
- Schmidt, J., Laufer, R., Herdrich, G., & Hyde, T. W. (2018). Electrostatic probe measurements in the inductively-heated plasma generator IPG6-B. *7th Russian-German Conference on Electric Propulsion*, (October). https://www.researchgate.net/publication/331686238%7B%5C_%7DElectrostatic%7B%5C_%7Dprobe%7B%5C_%7Dmeasurements%7B%5C_%7Din%7B%5C_%7Dthe%7B%5C_

%7Dinductively - heated% 7B % 5C_% 7Dplasma% 7B % 5C_% 7Dgenerator% 7B% 5C_% 7DIPG6-B

- Schmidt, T. D., Seboldt, W., & Auweter-Kurtz, M. (2006). Flexible Piloted Mars Missions Using Continuous Electric Propulsion. *Journal of Spacecraft and Rockets*, 43(6), 1231–1238. <https://doi.org/10.2514/1.17843>
- Schulze, J., Schüngel, E., Donkó, Z., Luggenhölscher, D., & Czarnetzki, U. (2010). Phase resolved optical emission spectroscopy: A non-intrusive diagnostic to study electron dynamics in capacitive radio frequency discharges. *Journal of Physics D: Applied Physics*, 43(12). <https://doi.org/10.1088/0022-3727/43/12/124016>
- Sou, H., Takao, Y., Noutsuka, T., Mori, Y., Uemura, K., & Nakashima, H. (2000). Study of plasma propulsion system with RF heating. *Vacuum*, 59(1), 73–79. [https://doi.org/10.1016/S0042-207X\(00\)00256-6](https://doi.org/10.1016/S0042-207X(00)00256-6)
- Takahashi, K. (2019). Helicon-type radiofrequency plasma thrusters and magnetic plasma nozzles. *Reviews of Modern Plasma Physics*, 3(1), 3. <https://doi.org/10.1007/s41614-019-0024-2>
- Takahashi, K., Charles, C., Boswell, R. W., Takao, Y., Fruchtman, A., Navarro-Cavallé, J., & Merino, M. (2020). Commentary: On helicon thrusters: Will they ever fly? *Frontiers in Physics*, 8(10), 8–10. <https://doi.org/10.3389/fphy.2020.00277>
- Tsifakis, D., Charles, C., & Boswell, R. (2020). An Inductively-Coupled Plasma Electrothermal Radiofrequency Thruster. *Frontiers in Physics*, 8(February), 1–10. <https://doi.org/10.3389/fphy.2020.00034>
- Turner, M. M., & Lieberman, M. A. (1999). Hysteresis and the E-to-H transition in radiofrequency inductive discharges. *Plasma Sources Science and Technology*, 8(2), 313–324. <https://doi.org/10.1088/0963-0252/8/2/312>
- Vaidya, S., Traub, C., Romano, F., Herdrich, G. H., Chan, Y. A., Fasoulas, S., Roberts, P. C., Crisp, N. H., Edmondson, S., Haigh, S. J., Holmes, B. E., Macario-Rojas, A., Oiko, V. T., Smith, K. L., Sinpetru, L. A., Becedas, J., Sullioti-Linner, V., Christensen, S., Hanessian, V., ... Belkouchi, B. (2022). Development and analysis of novel mission scenarios based on Atmosphere-Breathing Electric Propulsion (ABEP). *CEAS Space Journal*, 14(4), 689–706. <https://doi.org/10.1007/s12567-022-00436-1>
- Vitucci, J. J. (2019). *Development and test of a superconducting helicon plasma thruster* (Ph.D. Thesis). University of Maryland.
- Wegner, T., Küllig, C., & Meichsner, J. (2016). Mode transition and hysteresis in inductively coupled radio frequency argon discharge. *Physics of Plasmas*, 23(2). <https://doi.org/10.1063/1.4941586>
- Wollenhaupt, B., Le, Q. H., & Herdrich, G. (2018). Overview of thermal arcjet thruster development. *Aircraft Engineering and Aerospace Technology*, 90(2), 280–301. <https://doi.org/10.1108/AEAT-08-2016-0124>



Transient behaviour

Resolving transient discharge cycle behaviour in modulated inductive plasmas

2

The first article is an investigation into non-intrusive measurements taken of pure nitrogen, argon-nitrogen, and argon-oxygen plasmas. The non-intrusive measurements include the antenna current, visible light emission and magnetic field strength. These three measurements are strongly coupled and clearly indicate mode transitions within the plasma-antenna system. The mode transitions are transient phenomena that can only be resolved with a high sampling frequency. In other words, a conventional time-averaged analysis is shown to be inappropriate for the system under consideration. The investigations show that the antenna current is the most suitable indicator of mode transitions because it is global in nature, easy to measure and reveals the transitions in two ways: a shift in the amplitude and a shift in the frequency.

Statement of authorship

Title Resolving transient discharge cycle behaviour in modulated inductive plasmas

Publication Published: Georg, R., Chadwick, A. R., Dally, B. B., & Herdrich, G. (2020). Resolving transient discharge cycle behaviour in modulated inductive plasmas. *Vacuum*. <https://doi.org/10.1016/j.vacuum.2020.109636>

Principal author contribution

This paper reports on original research I conducted during the period of my Higher Degree by Research candidature and is not subject to any obligations or contractual agreements with a third party that would constrain its inclusion in this thesis. I am the primary author of this paper.

Principal author R. Georg

Contribution I contributed approximately 80 % to the authorship of this paper. Excluding the experimental component, I was primarily responsible for the conception of the paper. I drafted the manuscript including all tables and figures. I conducted the majority of the analysis. I acted as the corresponding author.

My contribution satisfies all authorship criteria of the *Australian Code for the Responsible Conduct of Research*.

_____ 8 July 2022

Co-author contributions

By signing the statement of authorship, each co-author certifies that: i. the candidate's stated contribution to the publication is accurate (as detailed above); ii. permission is granted for the candidate to include the publication in the thesis; and iii. the sum of all co-author contributions is equal to 100 % less the candidate's stated contribution.

Co-author A. R. Chadwick

Contribution Collected the experimental data that is analysed in the paper. Provided knowledge and assisted with analysis and revising the manuscript. Involved in the conception of the paper, particularly the experimental component.

_____ 8 July 2022

Co-author B. B. Dally

Contribution Provided knowledge and assisted with analysis and revising the manuscript.

_____ 8 July 2022

Co-author G. Herdrich

Contribution Provided knowledge and assisted with analysis and revising the manuscript. Involved in the conception of the paper, particularly the experimental component.

_____ 8 July 2022

Abstract

The further development of inductive plasma generators (IPGs) for space propulsion applications has driven the need for the development of non-intrusive experimental techniques that can resolve transient discharge cycle behaviour and accommodate a variety of propellant gases and gas-mixtures. In this work, a new approach is presented that simultaneously measures the antenna current, radially-resolved axial magnetic field strength and the radially-resolved emission in the visible range, at a sampling frequency sufficient to capture the driving and discharge cycle frequencies. Experiments were conducted using IPG7: a helical antenna IPG, driven nominally at 586 kHz, with 300 Hz discharge cycles. Nitrogen, argon-nitrogen, and argon-oxygen propellants were tested at capacitive and inductive conditions with input powers ranging from 4 kW to 36 kW. The propellants could be sourced from the space environment under in-situ resource utilisation. Analysis of the mean discharge cycle has made it possible to identify different coupling modes occurring within the cycle. These findings underscore the need to model such plasmas at the timescale of individual discharge cycles and demonstrate the value of the measured data for developing such models.

2.1 Introduction

Inductive plasma generators (IPGs) are well-established as a technology for silicon wafer etching; however, their application in space propulsion systems is a relatively new and ongoing development. Existing electric propulsion technologies involve direct contact between the electrode(s) and the propellant flow, causing erosion and limiting useful life. Currently, this problem is partially mitigated by using less reactive propellants, typically argon and xenon. In contrast, IPGs couple power from the antenna into the plasma remotely, with a dielectric barrier separating the two. Electrodeless thrusters, including those using inductive plasmas, are an active area in the literature with development occurring across several research groups (Sou et al., 2000; Herdrich et al., 2013; Navarro-Cavallé et al., 2018; Manente et al., 2019). A review of electrodeless thrusters conducted by Bathgate et al. (2017) gives an overview of the different approaches being pursued and their relative performance and development to-date. The development of electrodeless thrusters enables the use of more chemically reactive ‘alternative’ propellants, such as oxygen, water (vapour), carbon dioxide, or syngas from waste gasification and pyrolysis processes (Anih et al., 2019). This enables two new operating concepts: ‘in-situ resource utilisation’ (ISRU), collecting and using resources from the space environment, and ‘atmosphere-breathing electric propulsion’ (ABEP), accelerating atmospheric gases to offset drag in a very low Earth orbit. Development of a practical ABEP system based on an IPG and an applied static magnetic field is

ongoing (Romano et al., 2018; Romano et al., 2019). Both ISRU and ABEP represent a leap forward in terms of space operation capabilities and motivate the development of the various electrodeless electric propulsion approaches seen in the literature.

The chief issues when transferring knowledge and techniques from established IPG applications (Herdrich & Auweter-Kurtz, 2006) to a space propulsion application are the larger scale (e.g. larger geometries, flow rates, and powers), the use of complex feed gases (e.g. molecular gases and gas mixtures), and assessing and controlling propulsion characteristics (e.g. thrust, specific impulse, and thrust per unit power). In particular, the need to maximise propulsion characteristics necessitates a deeper understanding of the conditions within the plasma flow. Typically, this need is met by intrusive measurement techniques, for example Langmuir probes, however, they also disturb the plasma volume. This leads to characterisations which do not necessarily reflect the true operating conditions within the plasma. Furthermore, the extreme thermal and electromagnetic environment inside the discharge chamber, due to the high power, restricts the possibility of obtaining intrusive measurements over a significant period. Consequently, non-intrusive measurement techniques, such as optical emission spectroscopy (OES) or laser-induced fluorescence (LIF), have become important for investigating inductive plasma generators, particularly under high-power conditions. However, these techniques require consideration of the propellant gas chosen, and are limited when gas mixtures are considered, particularly for LIF. To derive the greatest benefit from the propellant-flexibility of an IPG-based thruster the diagnostic technique should also be flexible with regard to the propellant. A challenge common to both techniques is the need to obtain direct line-of-sight to the region of interest. The integration of the measured quantity along that line means that the spatial variation of the discharge is not captured.

Another important feature of the measurement technique, beyond the non-intrusive requirement, is the desire to conduct measurements at a high-sampling frequency in order to investigate transient effects. Transient effects appear when the driving frequency is modulated, either intentionally (modulated or dual-frequency plasmas) or unintentionally, due to power supply effects. In either case, experimental techniques that can resolve the modulation frequency are needed to understand the respective behaviours of such plasmas. Furthermore, resolving the driving frequency can give insight into the coupling behaviour. Chadwick et al. (2016) investigated the shift in the antenna current characteristic frequency over the discharge cycle duration using a high-speed current probe, showing a clear relationship between the frequency shift and coupling mode.

Optical emission spectroscopy (OES) is an established and well-known non-intrusive plasma diagnostic technique that consists of identifying different atomic and/or molecular states present in the plasma by their distinctive emission spectra. The method relies on the use of an appropriately detailed model of the species, their interaction and

respective emission spectra. The primary outputs of this method are number densities for various states present in the plasma, which are identifiable via their relative abundance, and the presence of distinguishing features in their emission spectra. While the majority of OES literature focuses on time-integrated measurements due to their relative simplicity, there is growing interest in measurements that are sufficiently frequent to resolve individual discharge cycles: this technique has been termed ‘phase-resolved OES’ (PROES) in the literature (Schulze et al., 2010).

By combining PROES with a collision-radiative model, Kaupe et al. (2018) were able to determine number densities and temperatures of various energy levels in an argon dielectric barrier discharge (DBD) excited at 30 kHz. Their technique was further developed to deal with the addition of small amounts of nitrogen to the argon (ranging 0% to 4%), although the nitrogen densities and temperatures were not determined (Kaupe et al., 2019). While the addition of nitrogen shows the robustness of their method, it also illustrates the inherent complexity of using PROES with plasmas containing multiple species, since the method could only tolerate 4 % nitrogen. Pure argon is typically studied due to its relatively simple and well-understood chemistry, while other species and mixtures of species remain a challenge (Schulze et al., 2010). This poses a problem when considering molecular species such as carbon dioxide, or mixtures such as argon-nitrogen or argon-oxygen, which may behave favourably when compared with pure nitrogen or oxygen alone for propulsive purposes in an IPG (Chadwick, 2017).

It is possible to use optical emission measurements without the need to incorporate a radiative model by considering the optical emission intensity as a measure of relative excitation in the plasma body. This approach was taken by Zaka-ul-Islam et al. (2015) to investigate the coupling modes in a radiofrequency-biased inductive plasma based on spatially- and temporally-resolved measurements of the oxygen 844 nm emission line. In particular, they were able to compare the effect of the coil and bias excitations on the plasma independently and together. They did not have simultaneous, synchronous measurements of the respective coil and bias currents, so they were forced to infer the time dependence between the currents and the measured optical emissions. Furthermore, they did not identify capacitive-inductive mode transitions at the timescale of the driving frequencies.

In an IPG two mechanisms for power absorption are provided by capacitive (E) and inductive (H) coupling modes. At low input powers the capacitive mode dominates, while at high input powers the inductive mode dominates. The conditions under which the transition occurs, specifically the discrepancy between starting and maintenance currents associated with hysteresis, were studied by Turner and Lieberman (1999). Subsequently, Cunge et al. (1999) demonstrated the significant effect that the matching conditions can have on the capacitive-inductive transition: in one matching condition the transition was marked by a sharp increase in antenna current, while in another it

2 Transient behaviour

was marked by a sharp decrease. More recently, the conditions of capacitive-inductive transition have been shown to be sensitive to factors such as plasma geometry, antenna geometry, pressure and plasma parameters (active and equivalent plasma resistances) (Kralkina et al., 2017; Kralkina et al., 2020). It has been shown that the capacitive coupling mode exists in parallel with the inductive coupling mode, and therefore the ‘inductive regime’ should properly be the ‘inductive-dominant regime’. When this capacitive component becomes significant it causes discrepancies with calculations based on a purely inductive coupling assumption. There have been several attempts to assess the parallel capacitive coupling by measuring the effect of either blocking it with a metallic screen (Godyak et al., 2002; Godyak, 2003) or enhancing it (Kralkina et al., 2016); in the latter work it was found that parallel capacitive coupling has a strong effect at pressures greater than 0.1 Torr.

The transition from a capacitive to inductive mode can be qualitatively identified by a significant increase in light emission which simultaneously concentrates in a ring distribution. The ring shape is explained by the combined effect of electromagnetic attenuation by the plasma volume (characterised by the skin depth δ) and the thermal boundary layer formed at the discharge chamber wall. Several formulae exist in the literature that couple the skin depth with other plasma parameters, such as the electron number density or conductivity, however, the effect of a thermal boundary layer is typically ignored (Lieberman & Lichtenberg, 2005). The thermal boundary layer thickness has previously been estimated at approximately 20 mm for IPG3 and IPG4 (predecessors to the IPG7 which have only minor differences) (Herdrich & Petkow, 2008). Such a layer would mean a region of lower charged-particle density due to lost energy. This layer has a significant effect in high-power sources, as evidenced by the heat transferred through the discharge chamber wall. Previous experimental work has determined this rate of heat transfer calorimetrically, ranging between 4 kW and 9 kW for an argon-nitrogen plasma with antenna power in the order of 25 kW, depending on the mixture ratio (Chadwick, 2017).

The capacitive mode can be further delineated into an alpha and gamma regime, the transition between which can be understood as a Paschen breakdown of the plasma sheath (Godyak & Kanneh, 1986). In the former regime ionisation in the plasma bulk is significant in maintaining the discharge, while in the latter regime it is the generation of electrons in the sheath near electrode. Consequently, the alpha regime is associated with a centralised distribution of light emission while the gamma regime is associated with a concentration near the antenna. The radial distribution of light emission can be used to distinguish between the various modes. Figure 2.1 is an axial photograph of an inductively coupled nitrogen plasma. The thermal boundary layer is visible as a relatively dark band at the outer radius of the plasma. The depth at which the maximum visible emission occurs, δ_{vis} , is also labelled. It is reasonably expected that many factors affect δ_{vis} since it is a product of electromagnetic, kinetic and thermal phenomena.

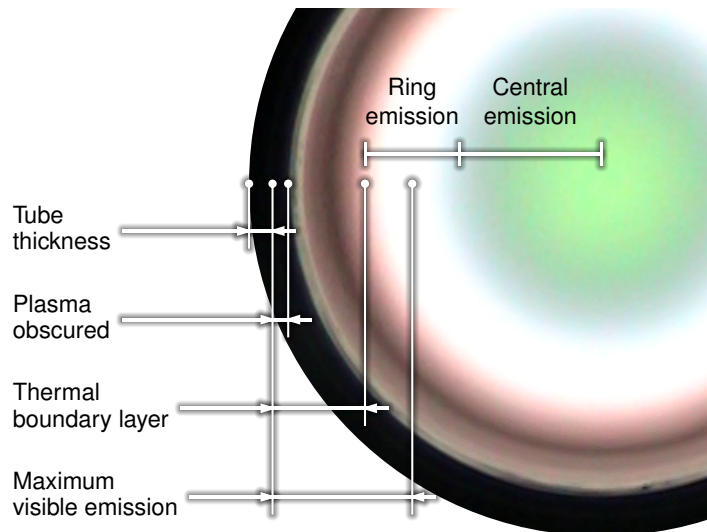


Figure 2.1: Axial photograph of an inductively-coupled nitrogen plasma.

Oxygen and nitrogen are likely candidates for electric propulsion ISRU due to their relative abundance in the space environment. However, because they occur as diatomic molecules, a significant amount of the energy delivered by the antenna is spent on dissociation; therefore, the ionisation degree is lower than, for example, argon which is monatomic. An argon-oxygen or argon-nitrogen mixture can overcome this issue because the easily ionised argon generates an electron population that can couple power from the antenna and heat the oxygen or nitrogen via collisions. Wang et al. (2018) demonstrated the positive relationship between argon fraction and electron density for an inductive argon-oxygen plasma. Additionally, argon's lower thermal conductivity brings the average thermal conductivity of the mixture down, thereby increasing the maximum operating power of the IPG before tube failure occurs due to thermal stress (Chadwick, 2017). Therefore, supplementing the ISRU nitrogen or oxygen with argon, either carried from Earth or also ISRU, presents an attractive solution for an IPG-based propulsion system. For these reasons, the candidate propellants for this work were nitrogen, oxygen, argon, argon-oxygen, and argon-nitrogen. In practice it was not possible to produce a stable inductive mode for pure oxygen and argon, therefore only nitrogen, argon-nitrogen, and argon-oxygen are presented in this work.

This paper presents a new approach to studying the transient behaviour of modulated inductive plasmas over the duration of individual discharge cycles. This approach involves the simultaneous non-intrusive measurement of the antenna current, axial magnetic field strength and light emission, alongside analyses of the synchronised signals. The approach is applied to high-power modulated argon-oxygen, nitrogen, and nitrogen plasmas in the context of characterising thrusters for space propulsion systems.

2.2 Methodology

2.2.1 Experimental setup

Experiments were conducted in the TIHTUS (thermal-inductive heated thruster of the University of Stuttgart) facility of the Institute for Space Systems (IRS), University of Stuttgart, Germany. The facility consists of a first-stage arcjet and a second-stage inductive plasma generator, which can be operated either independently or together (Böhrk & Auweter-Kurtz, 2006a). The operating principle of TIHTUS is shown diagrammatically in figure 2.2 (a). The arcjet deposits energy into the central region of the plume and is fed by an initial gas supply that is compatible with the arcjet (non-reactive with respect to the hot cathode). The inductive plasma generator deposits energy into the outer region of the plume and may be fed by an additional gas supply that is less restricted. The combined effect is to maximise propellant utilisation by creating a more uniform distribution of enthalpy in the plasma plume. Additionally, the IPG has a wider range of operating powers under inductive coupling owing to the ionisation provided by the arcjet. The arrangement of two independent gas supplies means that propellant flexibility of the IPG stage is not compromised. The layout of the TIHTUS test facility is shown in figure 2.2 (b). The facility is fitted with several diagnostic techniques for both the generator and the plume. The generator is mounted onto a vacuum chamber with a length of 3 m and a diameter of 2 m. A notable feature of this facility is the optical diagnostics locations which allow optical access to the generator and the plasma plume. In this work, the arcjet is removed and only the inductive plasma generator, IPG7 (Massuti-Ballester et al., 2013), is considered.

Figure 2.3 shows the layout of the experimental setup, including a simplified sectional view of IPG7. This generator has an axi-symmetric design, consisting of a quartz tube (the discharge chamber), surrounded by a 5.5-turn helical coil antenna. It can achieve steady operation up to a maximum anode (input) power of 180 kW, necessitating an active tube cooling system. A jacket encloses the coil and tube, forming channels for cooling water to flow through. The antenna coil is excited by a Meissner oscillator (also known as Armstrong oscillator) resonant circuit without matching network, shown in figure 2.4. The 50 Hz three-phase facility power is full-wave rectified and capacitively damped to produce a quasi-DC power that feeds the resonant circuit at the triode's anode. This process introduces characteristic frequencies at 100, 200, 300, 600 and 900 Hz. The 300 Hz frequency is the most significant of these, and modulates the power provided to the antenna to the extent that plasma ignition, mode transitions, and extinguishment, can occur within each 3.33 ms discharge cycle.

A typical arrangement for exciting an inductive plasma consists of signal generator, amplifier, matching network and antenna. This provides a stable excitation frequency and enables the minimisation of reflected power by matching the source and

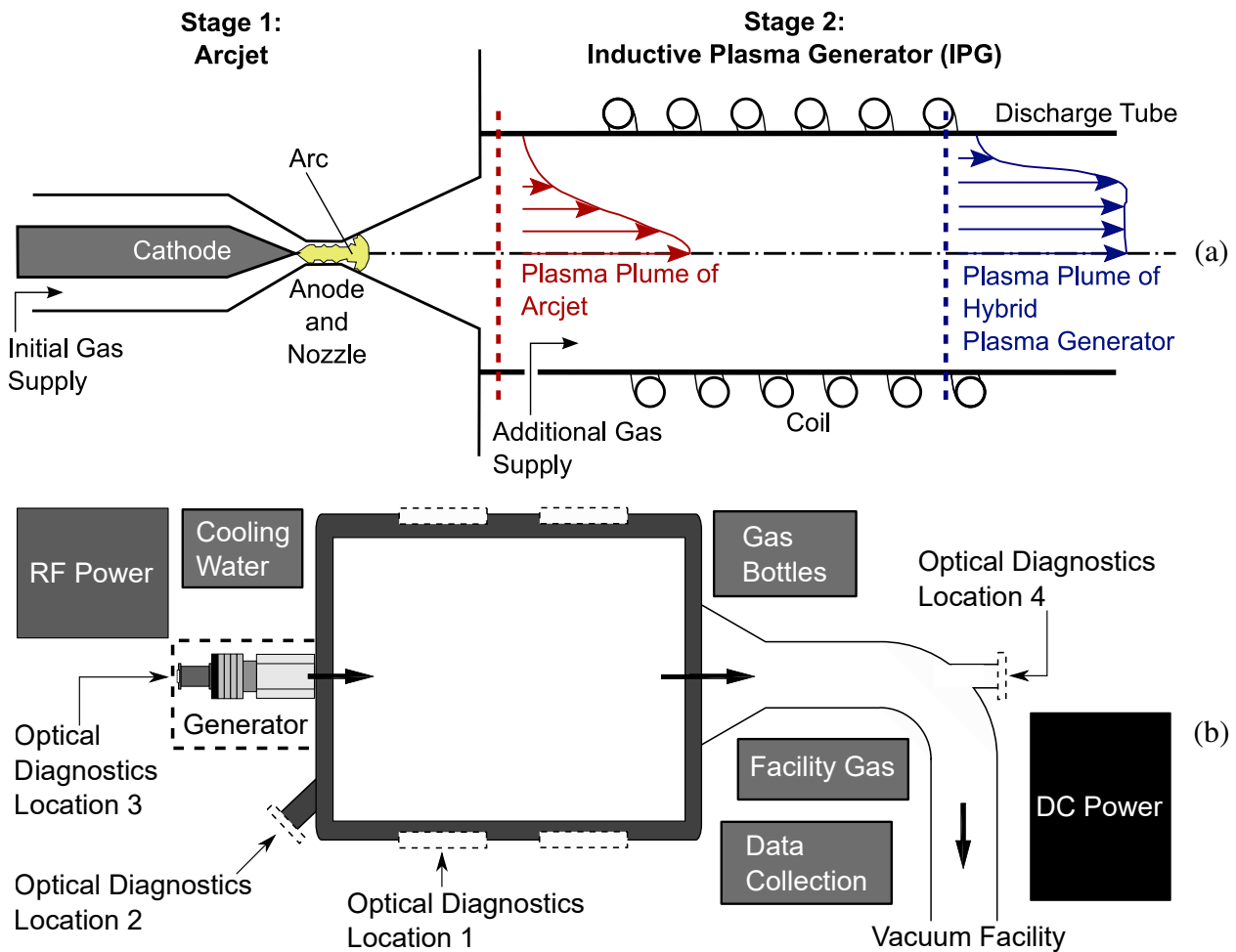


Figure 2.2: TIHTUS (thermal-inductive heated thruster of the University of Stuttgart) operating principle (a) (adapted from Böhrk and Auweter-Kurtz (2006b)) and test facility (b) (adapted from Herdrich et al. (2015)).

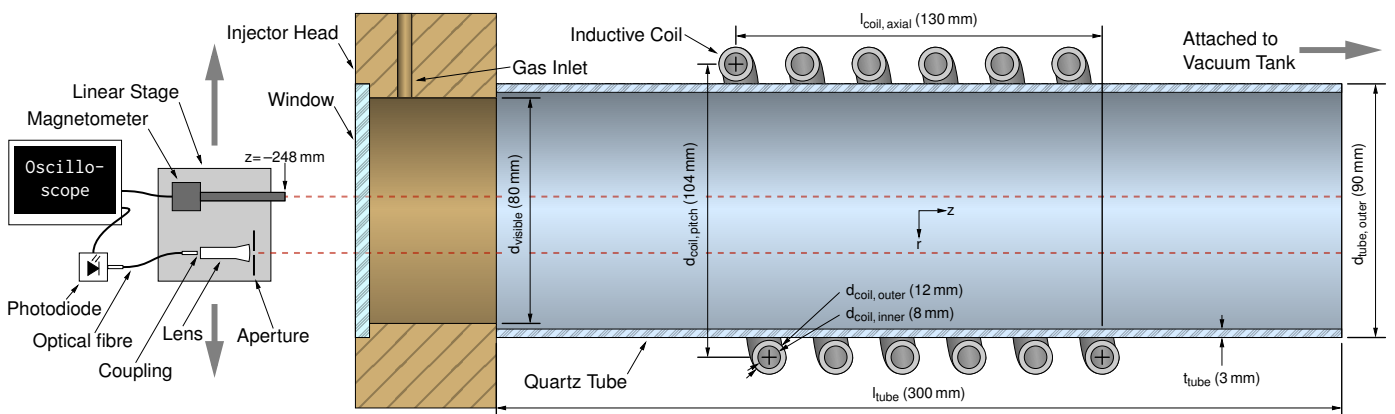


Figure 2.3: Experimental setup including simplified sectional view of IPG7 with dimensions. A jacket encloses the coil, forming channels for cooling water (not shown).

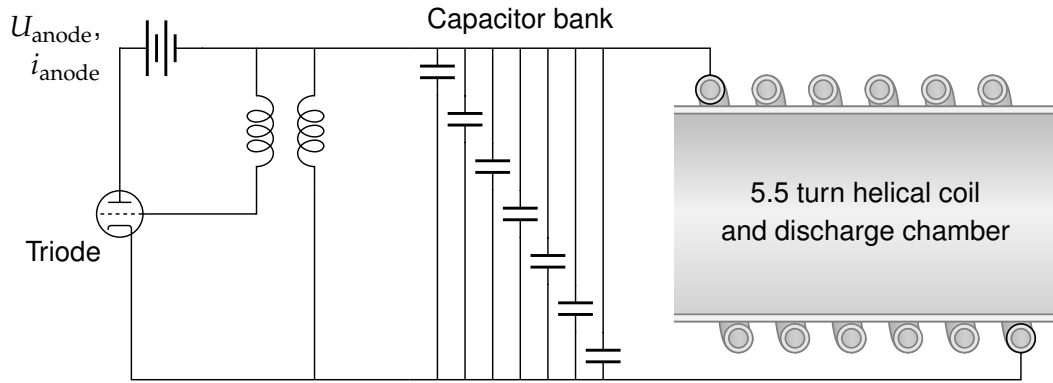


Figure 2.4: IPG7 resonant circuit.

load impedances. In IPG7 the resonant circuit ensures that the excitation frequency always matches the resonant frequency, however, there is no matching network, or in other words the matching condition is fixed. In this fixed ‘matching condition’ the antenna current always decreases sharply at the capacitive-inductive transition.

The resonant frequency of the circuit is determined by its effective capacitance and inductance. The effective capacitance is determined by a bank of seven 6 nF capacitors and the effective inductance is determined by the geometry of the coil. In this work, five of the capacitors were connected, corresponding to a nominal frequency of 586 kHz for the particular coil geometry used (Herdrich & Petkow, 2008). Taking the FFT of the antenna current reveals a distribution of frequencies surrounding the nominal frequency. Furthermore, a short-time FFT reveals that this distribution can be described as a single instantaneous characteristic frequency that varies over the 3.33 discharge cycle period. In a capacitive coupling mode, this variation is relatively small and could be attributed to the temperature-dependant properties of the circuit or capacitance between the antenna and plasma body. In an inductive coupling mode, the characteristic frequency increases significantly due to the development of an azimuthal current within the plasma that increases the effective inductance of the circuit (Chadwick et al., 2016). Consequently, the plasma discharge is not truly steady, and the behaviour at the level of discharge cycle should be considered. This is also important for diagnostic purposes as the IRS IPG family is also used for aerothermodynamic testing (e.g. to test heat shield materials) (Herdrich et al., 2009; Loehle et al., 2022).

The coil current was measured by a Hofer-Noser Karrer (HOKA) probe designed by Kametech AG (Karrer et al., 1999; Karrer et al., 2003). The probe measures the magnetic field produced by the current flowing in the coil. Special features of the probe are its ability to withstand long periods of exposure to the current, due to its non-ferrous design, and its relatively high sampling frequency (up to 4 MHz). It has been noted in previous investigations that, due to the strong coupling between the coil

Table 2.1: Summary of experimental conditions. For each propellant mixture, data was collected at a stable anode potential just before (capacitive) and after (inductive) the capacitive-inductive transition. The unit L_n/min refers to normal litres per minute.

Case		Regime	Anode conditions		Pressure		
Species: flow rate [L_n/min]	Total mass flow rate [g/s]		Potential [kV]	Power [kW]	Injector [Torr]	Tube (est.) [Torr]	Tank [Torr]
N ₂ : 107	2.23	Cap.	2	4	31	2.9	0.20
		Ind.	4	25	31	3.9	0.22
Ar: 90, N ₂ : 43	3.58	Cap.	2	4	43	4.3	0.19
		Ind.	4	34	43	5.2	0.20
Ar: 90, O ₂ : 43	3.69	Cap.	3	10	43	4.7	0.19
		Ind.	4	36	43	5.3	0.22

and the plasma, variations in the magnitude and characteristic frequency of the plasma current can be observed by way of the HOKA probe (Chadwick et al., 2016; Herdrich & Petkow, 2008; Auweter-Kurtz & Wegmann, 1999).

The electrodeless nature of IPG7 allows the use of the chemically reactive propellant gases such as oxygen, carbon-dioxide, and water vapour, in addition to gases, such as argon, hydrogen and nitrogen. A co-axially positioned window in the injector head (optical diagnostics location 3 in figure 2.2 (b)) allows radially-resolved non-intrusive measurements. Pressure can reach less than 1 Pa without propellant flow or 10–30 Pa with a typical propellant flow in the order of g s^{-1} for gases such as oxygen, nitrogen or carbon dioxide.

Radial profiles of light emission and axial magnetic field strength were obtained by sensors mounted on a linear stage located at the injector head window. Light emission in the visible range was measured by a Thorlabs DET210 photodiode unit connected via optical fibre to a lens and aperture assembly. The spectral response covers 200 nm to 1100 nm (including the complete visible range), with a peak response of 0.45 A/W at 730 ± 50 nm (ThorLabs, 2005). The axial magnetic field strength was captured by a Projekt Elektronik FM 302 magnetometer with axial probe AS-HAP (Projekt Elektronik, 2016). During each data acquisition, the emission intensity, magnetic strength, and coil current were measured simultaneously over a 20 ms duration at a sampling frequency of 5 MHz, approximately 10 times the driving frequency. In this study, the relative intensity of the light emission is considered, therefore, the measured values are given in normalised units. Neither the axial location of the lens nor the effect that the intensity is integrated along the line of sight are critical. For the magnetometer, the distance from the probe tip to the centre of the coil was 248 mm.

The axial magnetic field strength, as measured by the magnetometer, arises primarily

2 Transient behaviour

from the coil current and secondarily from the motion of charge particles in the plasma. Considering the coil as a current-carrying sheet with some diameter and length but zero radial thickness allows for determination of an analytical expression for the magnetic field resulting from the coil current at arbitrary points in space. There are several exact and approximate solutions available in the literature. The solution developed by Derby and Olbert was selected for this work because it is exact, relatively simple, and an efficient algorithm is provided for its computation (Derby & Olbert, 2010). The axial magnetic field strength per unit coil current, at a location specified by the axial (z) and radial (ρ) coordinates, is given by

$$\frac{H_z}{I_{\text{coil}}}(z, \rho) = \frac{N}{2b\pi} \frac{a}{a + \rho} [\beta_+ C(k_+, \gamma^2, 1, \gamma) - \beta_- C(k_-, \gamma^2, 1, \gamma)]$$

where

$$\beta_{\pm} = \frac{z_{\pm}}{\sqrt{z_{\pm}^2 + (a + \rho)^2}}, \quad k_{\pm} = \sqrt{\frac{z_{\pm}^2 + (a - \rho)^2}{z_{\pm}^2 + (a + \rho)^2}}, \quad z_{\pm} = z \pm b, \quad \gamma = \frac{a - \rho}{a + \rho}.$$

Here, a is the effective radius of the coil, b is half the axial length of the coil, and N is the number of turns. The parameter C is a generalised complete elliptic integral; an algorithm for computing it is provided in (Derby & Olbert, 2010).

Three propellant mixtures were selected for this study: nitrogen, argon-nitrogen, and argon-oxygen. For each propellant, the anode potential was adjusted to achieve two conditions: a stable capacitive condition just before capacitive-inductive transition and a stable inductive condition just after transition. These conditions are summarised in table 2.1. The various conditions were identified by examining the overall magnitude and radial distribution of the emitted visible light; the capacitive regime having little or no emission and the inductive regime having significant emission and a ring-like distribution. Pressures were measured at the injector head and at the tank wall, representing respectively upper and lower bounds for the discharge chamber (tube) pressure which was not measured directly. Tube pressures were estimated based on a linear interpolation of tube pressures that were previously measured as a function of propellant mass flow rate and anode power for pure oxygen in IPG3, and should be taken only as an indication of the order of magnitude and trend (Herdrich, 2004). The relatively high tube pressures, in the range of 2 Torr to 6 Torr, suggest the possibility of a significant capacitive coupling channel in parallel to the inductive coupling channel (Kralkina et al., 2016).

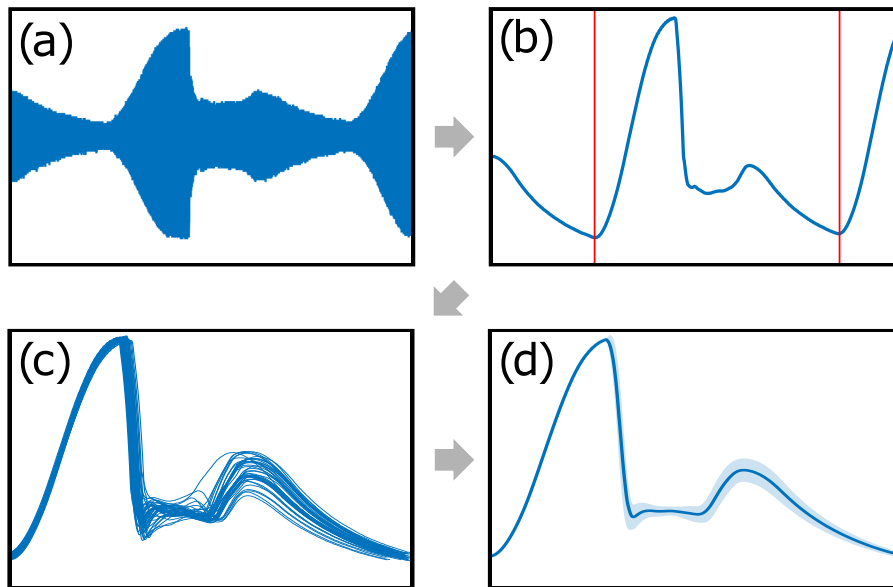


Figure 2.5: Method used to collate the discharge cycles. (a) raw signal, (b) RMS signal with cycle boundaries identified by minima, (c) individual cycles collated, (d) mean and standard deviation represented by line and shaded region.

2.2.2 Collation of discharge cycles

The coil current, emission intensity, and magnetic field strength measurements all exhibit a cyclical pattern at approximately 300 Hz. This phenomenon has previously been observed in the coil current and is attributed to the design of the facility's power supply (Herdrich & Petkow, 2008). The appearance of the same cyclical pattern in the other signals indicates the strong interconnection between them. A process was developed to collate the individual cycles together to assess the level of variation and to enable further analyses: this process is summarised in figure 2.5. The resulting mean and standard deviation curves represent, respectively, the typical discharge cycle and the level of variation between cycles. The process is initially performed on the antenna current signal, then repeated for the emission intensity and magnetic field strength measurements, using the cycle boundaries identified from the antenna current to preserve synchronicity. These collated signals are the basis for the results that follow.

2.3 Results & discussion

Firstly, the time-resolved measurements of coil current, axial magnetic field strength, emission intensity and coil current characteristic frequency over the discharge cycle period are presented at different conditions according to table 2.1 in figures 2.6 to 2.8. From this data, it is possible to observe the effect of mode transition on these parame-

2 Transient behaviour

ters and to identify clearly the periods of different coupling modes. Subsequently, the spatially- and time-resolved measurements of light emission are presented in figures 2.9 to 2.14.

Figure 2.6 shows the coil current, axial magnetic field strength, relative light emission (visible range), and characteristic frequency of the coil current for pure nitrogen over the discharge period. For the capacitive 2 kV condition, the coil current has a smooth, continuous profile, indicating minimal interaction between the coil and the plasma. For the inductive 4 kV condition, there is the same trend, except for the period between 0.8 ms and 2 ms where the current dips significantly. This reduction of the coil current is evidence of inductive coupling occurring between the coil and the plasma, and therefore marks the inductive portion of the cycle. Hence, when the ‘inductive’ case is examined at the level of individual discharge cycles, it is revealed that each cycle is comprised of a capacitive-dominated period and an inductive-dominated period.

The measured and calculated magnetic field strength profiles have a near-identical resemblance for both conditions, especially at higher magnitude. This is remarkable since the model that is the basis for the calculations is relatively simplistic and does not account for the plasma current. Since the plasma current does not appear as a discrepancy between the measured and calculated magnetic field strengths, this implies there is a negligible contribution from the plasma current. Two exceptions to the similarity occur at approximately 1 and 2 ms in the 4 kV condition; both occur during the capacitive part of the cycle. The standard deviation is more significant for these periods, indicating high random variation between individual cycles.

The capacitive case produces negligible visible radiation: this is seen in all the capacitive datasets. For the inductive case, there is an increase in emission intensity coinciding with the sudden decrease in coil current. The visible radiation peaks as the coupling mode transitions from inductive to capacitive and then decays. This indicates the halting of the generation of heavy, energetic, light-emitting species, and their subsequent decay.

The difference between the capacitive and inductive coupling periods is the most distinct in the characteristic frequency plot. For the capacitive 2 kV condition, the profile is near constant, with a small (1.2 % of the mean), steady increase over the cycle period. This small increase could be explained by thermal effects within the power circuit changing the effective capacitance. The same profile is seen in the 4kV condition for the periods of capacitive coupling. The transition to inductive coupling triggers a sharp departure from the capacitive profile, indicating a change in the effective inductance due to the establishment of an azimuthal plasma current. Based on the characteristic frequency, which gives the clearest indication of the coupling mode, the capacitive and inductive modes occupy approximately 75% and 25% of the cycle duration, respectively. The difference between characteristic frequencies for capacitive and inductive

conditions gives a qualitative measure of the plasma current, since they are connected by the plasma inductance.

Following the assumption that the frequency change is due to an azimuthal plasma current, the frequency change can be used as a qualitative measure of that plasma current. Therefore, the peak plasma current occurs 0.31 ms after the peak antenna current and 0.40 ms before the peak light emission. The first period indicates the lag between the inductive ‘ignition’ and maximum inductive coupling. The second period indicates the lag between the maximum inductive coupling and the maximum population of light emitting species: in other words, the time necessary for the electron and ion populations to reach equilibrium.

Figure 2.7 shows the coil current, axial magnetic field strength, light emission (visible range), and coil current characteristic frequency for an argon-nitrogen mixture over the discharge period. The trends of the coil current profiles bear a strong resemblance to that of the nitrogen case, although here the dip in the profile for the inductive case is longer in duration and therefore assumes a lower value when the capacitive regime is resumed. The coil current is not steady throughout this period and at 1.8 ms there is a high level of variation between cycles. The measured and calculated magnetic field strengths are relatively close, more so than for nitrogen. The exception, in this case, is the peak just before transition to the inductive mode. Again, a negligible contribution from the plasma current is implied.

The light emission profile for the inductive case resembles a smooth, non-skewed curve that increases from zero at the capacitive-inductive transition, peaks just before the inductive-capacitive transition, and decays to zero just as the next capacitive-inductive transition occurs. In other words, the population of heavy, light-emitting particles dips to zero only momentarily. The smooth maximum occurring before the end of the inductive regime may represent an equilibrium state where the population of light-emitting particles stabilises for that particular set of conditions. This is in contrast with the light emission profile for nitrogen, which shows a sharp peak, indicating that the population of light-emitting particles was still increasing rapidly when the inductive regime ended.

The inductive period of the characteristic frequency profile has a strong left skew, indicating a rapid onset and slow decay of the plasma current. The capacitive and inductive modes occupy approximately 43% and 57% of the cycle duration, respectively. The peak plasma current occurs 0.37 ms after the peak antenna current, and 1.04 ms before the peak light emission.

Figure 2.8 shows the coil current, axial magnetic field strength, light emission (visible range), and characteristic frequency of the coil current for an argon-oxygen mixture over the discharge period. The trends of the coil current profiles have a stronger resemblance to the argon-nitrogen case than the nitrogen case, due to the long period of inductive coupling, although the current is steadier during the inductive period. Here

2 Transient behaviour

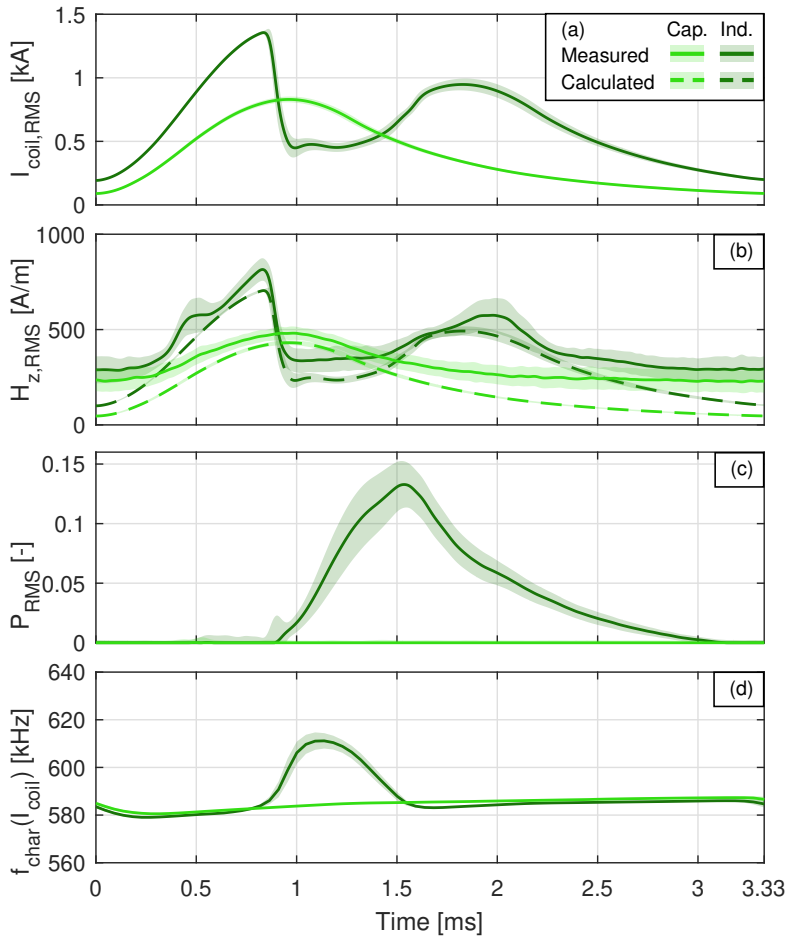
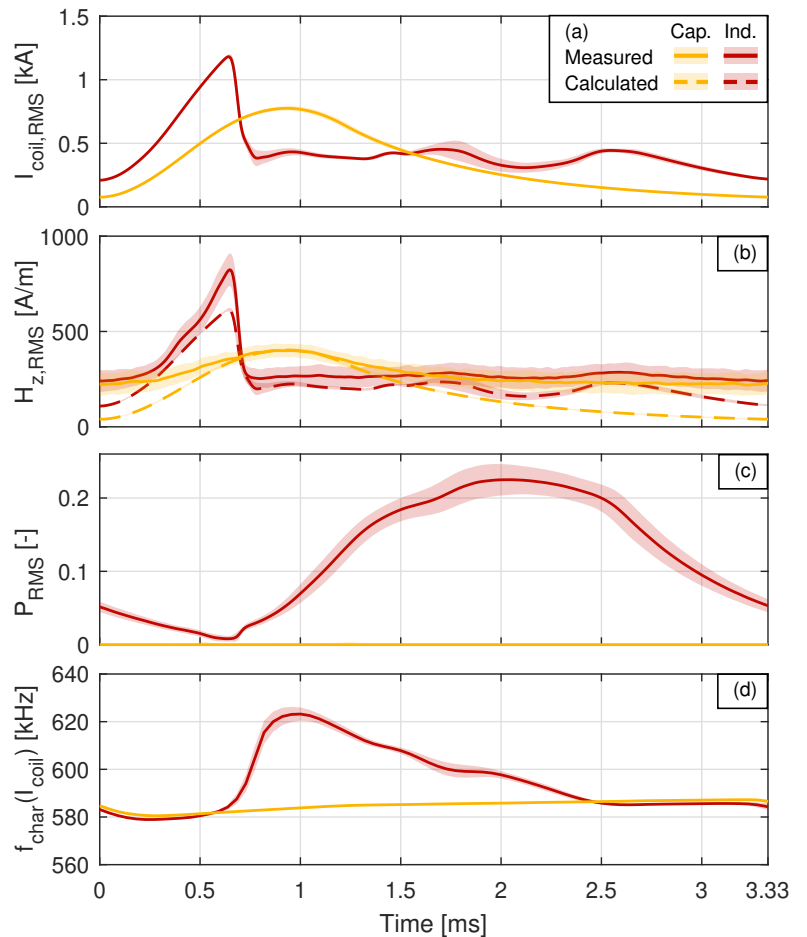


Figure 2.6: Coil current (a), axial magnetic field strength (b), emission intensity (c), and coil current characteristic frequency (d) for pure nitrogen, over the discharge cycle period. The lines and shaded regions represent the means and standard deviations of the collated discharge cycles, respectively.

Figure 2.7: Coil current (a), axial magnetic field strength (b), emission intensity (c), and coil current characteristic frequency (d) for an argon-nitrogen mixture, over the discharge cycle period. The lines and shaded regions represent the means and standard deviations of the collated discharge cycles, respectively.



the anode potential for the capacitive case is 3 kV, rather than the 2 kV seen for the other two propellants. This is reflected in a proportional increase in the magnitude of the capacitive profiles of the coil current and the magnetic field strength. Once again the measured and calculated magnetic field strengths are near-identical, implying a negligible contribution from the plasma current.

The capacitive argon-oxygen case has negligible visible radiation, despite having the highest anode potential and power of any of the capacitive cases. The inductive case has the highest radiation intensity of any propellant. There is a sudden increase in emission intensity coinciding with the capacitive-inductive transition, with the maximum radiation intensity reached soon after, well before the inductive-capacitive transition. The smooth maximum occurring during the inductive coupling period suggests the attainment of an equilibrium state, as it did for the argon-nitrogen case. The key departures from the argon-nitrogen are the left-skew of the distribution, and the non-zero value of the minimum. The minimum value indicates that the population of light-emitting particles is present throughout the entire cycle.

Similar to argon-nitrogen, the inductive period of the characteristic frequency profile has a strong left skew, indicating a rapid onset and slow decay of the plasma current. The capacitive and inductive modes occupy approximately 30% and 70% of the cycle duration, respectively. The peak plasma current occurs 0.38 ms after the peak antenna current, and 0.50 ms before the peak light emission.

The near-identical trends of the argon-oxygen and argon-nitrogen cases, when comparing the antenna current, axial magnetic field, and characteristic frequency, indicate near-identical behaviour in terms of the coupling between antenna and plasma. Therefore, different coupling behaviour between the two cases cannot explain the observation that the light emission intensity profile is left skewed for argon-oxygen and not for argon-nitrogen. A preliminary interpretation is that the argon-nitrogen case is slower to reach equilibrium; however, the spatially resolved data presented in the next section gives some further insight into this phenomenon.

The results presented in this section clearly show the mode transitions occurring on the time scale of the 300 Hz discharge cycle for the inductive cases. The transitions are discernible by the deviations of the characteristic frequency and coil current profiles. For the coil current, capacitive-inductive transition occurs at the maximum value, which raises the question of whether that value represents a critical value. This hypothesis is contradicted by the argon-oxygen case, because the maximum capacitive coil current exceeds the maximum inductive coil current. Two alternatives were considered as predictors for the capacitive-inductive transition and are presented in table 2.2: the accumulated energy over the period between the minimum and maximum current, and the instantaneous power at the maximum current. Again, argon-oxygen presents an exception, as the accumulated energy is greater for the capacitive case than the inductive case. For all three propellants, the instantaneous power has the desired trend,

Figure 2.8: Coil current (a), axial magnetic field strength (b), emission intensity (c), and coil current characteristic frequency (d) for an argon-oxygen mixture, over the discharge cycle period. The lines and shaded regions represent the means and standard deviations of the collated discharge cycles, respectively.

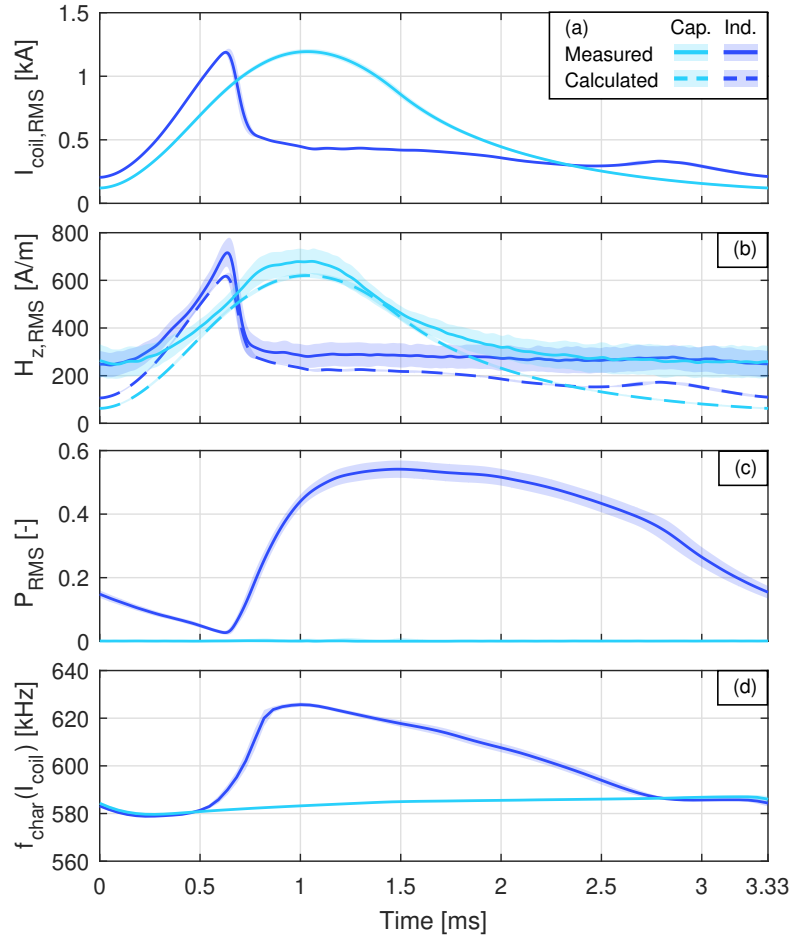


Table 2.2: Coil conditions at maximum current for each propellant for capacitive and inductive cases. The accumulated energy is calculated as $U_{\text{anode}} \cdot \int_{t=0}^{t=t_{\text{max}}} I_{\text{coil,RMS}}(t) dt$, and the instantaneous power is calculated as $U_{\text{anode}} \cdot I_{\text{coil,RMS}}(t = t_{\text{max}})$. U_{anode} is used in place of U_{coil} , since they are of the same order (Herdrich & Petkow, 2008) and the latter was not measured.

Case		Anode conditions		Coil conditions at maximum current	
Species: flow rate [L _n /min]	Regime	Potential [kV]	Power [kW]	Accum. energy [kJ]	Instant. power [MW]
N ₂ : 107	Cap.	2	4	0.92	1.66
	Ind.	4	25	2.39	5.37
Ar: 90, N ₂ : 43.2	Cap.	2	4	0.78	1.47
	Ind.	4	34	1.51	4.62
Ar: 90, O ₂ : 42.6	Cap.	3	10	2.16	3.58
	Ind.	4	36	1.48	4.64

although further work is needed to determine the consistency of this behaviour under other conditions. The accumulated energy and instantaneous power for argon-oxygen and argon-nitrogen are remarkably similar and may indicate the dominance of the argon component (due to its lower ionisation energy) in the capacitive-inductive transition when compared with the other species. By contrast, the addition of argon to nitrogen has a significant effect, by reducing both the accumulated energy and instantaneous power at the capacitive-induction transition.

For each dataset the difference between the capacitive and inductive characteristic frequency profiles provides evidence of strong plasma currents, while the small discrepancy between the measured and calculated magnetic field strengths provides evidence to the contrary. This contradiction is resolved by supposing that the plasma current is concentrated in a region relatively far from the magnetometer, such that the effect of the antenna current dominates due to its closer proximity and the strong decay of the magnetic field strength with increasing distance. Since the magnetometer was located on the injector head side of the plasma source, the plasma current must be located in the downstream region. This is a reasonable conclusion because particles in the downstream region have, in effect, had a longer residence time in close proximity to the antenna, therefore higher densities of electrons and ions are to be expected. The supposition is further supported by observed failures of the discharge tube, caused by thermal stress, occurring in the downstream region and experimental measurements of the chamber inner wall temperature that show the maximum also occurring in the downstream region (Chadwick et al., 2018).

2.3.1 Spatially resolved discharge cycles

In the previous plots, the radially resolved measurements, that is the axial magnetic field strength and the light emission, were averaged across the radial position in order to focus solely on the variation with respect to time. Subsequently, the radially resolved data are considered. The first point to note is that the magnetic field strength was uniform across the radial position. It was expected to see some radial distribution due to the highly localised plasma current; however, its absence is further evidence supporting the supposition that the plasma current is located at the far-end of the tube, away from the magnetometer. For this reason, the following results focus only on the radially resolved light emission measurements. Radial positions are reported as distance from the central axis of the plasma generator. Where a ring emission is discernible, δ_{vis} is equal to the discharge tube inner radius (43 mm) minus the radial position.

In figure 2.9, radial distributions of light emission are plotted for the inductive, 4 kV condition for pure nitrogen. Measurements were taken at 16 positions across the diameter of the IPG window, and diametrically opposing pairs of points were averaged to yield 8 radially located points. A cosine sum was chosen as the fitting function to

2 Transient behaviour

ensure continuity at the centre. The first of the curves is the mean over the duration of the discharge cycle: in other words, it is not time resolved. This corresponds to a slower-sampling-rate measurement such as a CCD-array might capture, or to what an observer would see by eye. This time-averaged curve is fairly uniform, with a small peak corresponding to the ring emission at 37 mm ($\delta_{\text{vis}} = 6$ mm). Two instantaneous distributions of emission are also plotted, corresponding to the occurrence of the minimum and maximum total emission. At the maximum total emission, there is a strong ring emission at 36.5 mm ($\delta_{\text{vis}} = 6.5$ mm). At the minimum total emission, the intensity is zero across the entire radius. Due to the relatively short duration of the inductive mode, the emission intensity decays quickly (that is, energetic, heavy species reduce in number).

In figure 2.10 (a) the coil current and its characteristic frequency are reproduced for reference. In figure 2.10 (b) the full light emission data are shown as a contour plot over the discharge cycle period and radial position. The antenna current and characteristic frequency are reproduced for reference (a). With the aid of this reference, it is clear that the onset of the ring emission occurs simultaneously with the onset of the inductive mode. The location of the maximum of the ring emission is plotted over the contour plot to show its movement over time. The absence of any central emission, and the relatively short duration of the light emission, are apparent. During the period of emission, the ring emission location is fairly constant at 36.5 ± 0.5 mm ($\delta_{\text{vis}} = 6.5 \pm 0.5$ mm), except for the initial onset, where it approaches from the discharge chamber wall.

The magnitudes of the emission along the centreline, and the maximum of the ring emission (when it is discernible), are plotted in figure 2.10 (c). The ring emission intensity increases rapidly up until the very end of the inductive coupling period, suggesting increasing ionisation up until that point, or, put differently, that the species populations in the plasma have not stabilised. A large inter-cycle variation is seen for the central region, which may be a product of unsteady non-axial flow in that region transporting light-emitting particles to or from the centre.

In figure 2.11 radial distributions of light emission are plotted for the inductive, 4 kV condition of the argon-nitrogen mixture. The time-averaged curve shows a ring emission occurring at 26.5 mm ($\delta_{\text{vis}} = 16.5$ mm). Three instantaneous distributions of emission are also plotted, corresponding to the occurrence of the minimum total emission, development of a stable ring emission, and maximum total emission. The stable ring emission profile shows a strong ring emission occurring at 31.0 mm ($\delta_{\text{vis}} = 12$ mm). In comparison, at the maximum total emission, the ring emission has a great intensity and has moved inwards to 25.5 mm ($\delta_{\text{vis}} = 17.5$ mm). The minimum total emission is non-zero, but comparatively negligible.

The evolution of the ring emission can be traced in figure 2.12 (b). The inductive mode starts at 0.6 ms according to the characteristic frequency, approximately coinciding with the minimum total emission at 0.64 ms. Subsequently, the emission increases

Figure 2.9: Emission intensity plotted against radial position at different times for pure nitrogen at 4 kV anode potential. The first plot is the mean over time; subsequent plots are instants in time corresponding to: minimum total emission, and maximum total emission.

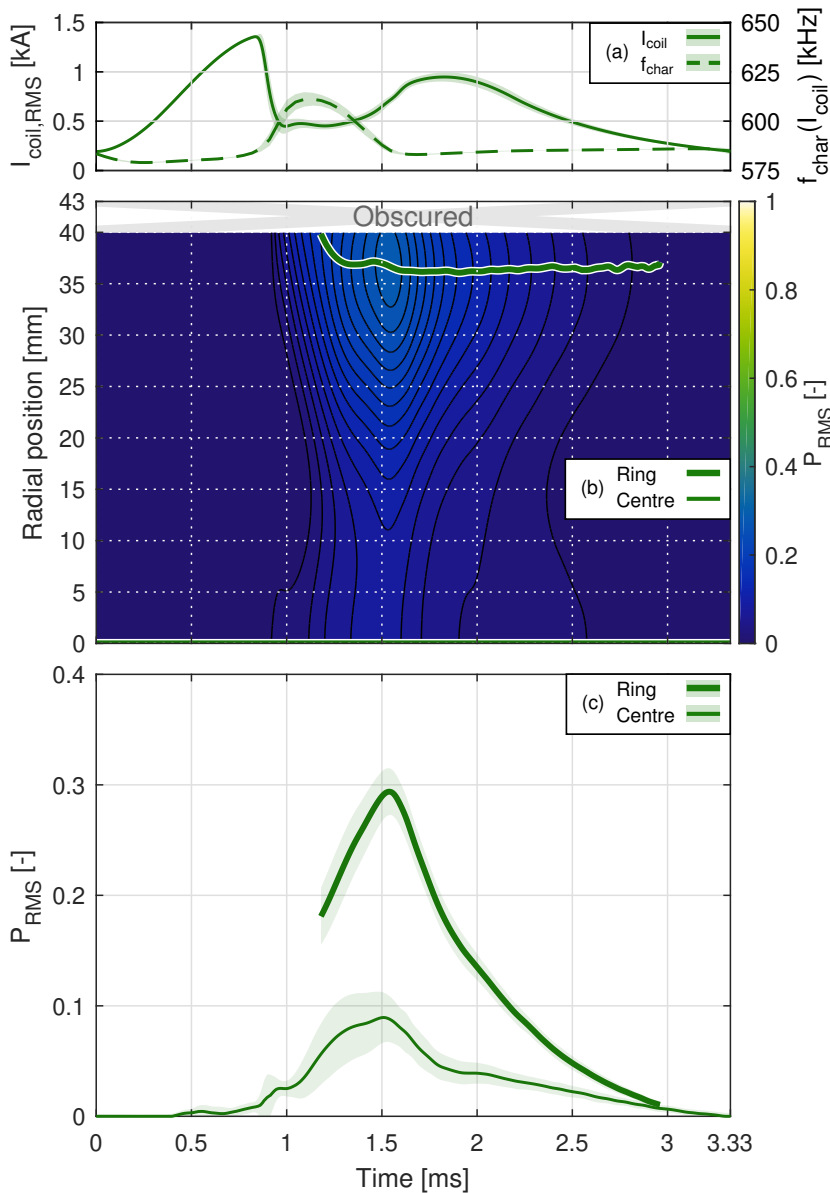
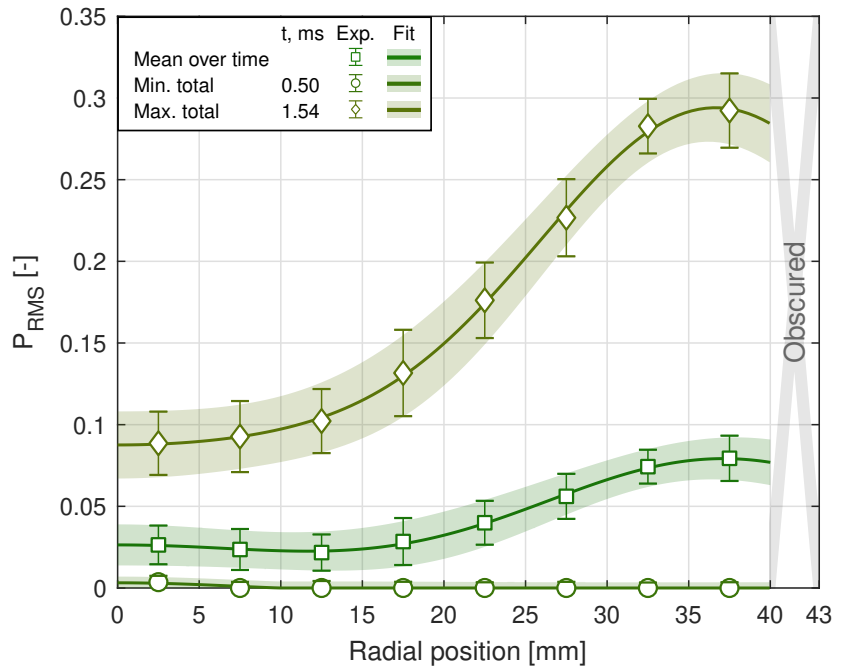


Figure 2.10: The radial and temporal distribution of emission intensity for pure nitrogen at 4 kV anode potential. The antenna current and characteristic frequency are shown again for reference (a). The radial and temporal distribution is shown in (b), with the location of the maximum ring emission shown as a thick line, and the centre-line as a thin line. The magnitudes under these lines are plotted in (c) against time.

2 Transient behaviour

rapidly, and the ring emission is identifiable at 1.2 ms, moving rapidly inwards and then stabilising momentarily. The ring emission moves inwards again before reaching the maximum total emission, where it remains and decays. There is no central emission, as was the case for pure nitrogen.

Referring to the trace of the ring emission intensity in figure 2.12 (c), it appears that the intensity plateaus briefly at the initial stabilisation. Given the lower energy required to ionise argon, as compared with that needed to dissociate and ionise molecular nitrogen, this may indicate a momentary equilibrium condition for the argon component, before there is appreciable light emission coming from the nitrogen component. The total maximum emission, therefore, represents the equilibrium of both the argon and the nitrogen components.

In figure 2.13, the radial distributions of light emission are plotted for the inductive, 4 kV condition of the argon-oxygen mixture. The time-averaged curve is mostly uniform, with only a small ring emission discernible at 28 mm ($\delta_{\text{vis}} = 15$ mm). The subsequent curves are snapshots of the emission profile at the time of minimum total emission, maximum central emission, maximum ring emission, and stabilisation of the ring emission after shifting inwards. Comparison of these curves shows several features that are not visible in the time-averaged profile. Firstly, there is a strong, transient central emission. Secondly, the ring emission is more pronounced and shifts position over the course of the cycle. Thirdly, for part of the cycle, the central and ring emissions disappear. Fourthly, the onset of the central and ring emissions occurs simultaneously with the frequency shift due to inductive coupling, however, the central emission maximum occurs 0.70 ms before the ring emission maximum.

A possible explanation for the central emission is alpha-capacitive coupling since it is associated with a centralised distribution of light emission. As explained in the methodology, the relatively high discharge chamber pressure permits a significant capacitive coupling in parallel to the inductive coupling. Referring to the antenna current and characteristic frequency in figure 2.14 (b), it is clear that the onset of the central and ring emissions occur simultaneously with the onset of the inductive mode; however, the ring emission develops at a slower rate. The ring emission location varies between 32 mm and 24 mm ($11 < \delta_{\text{vis}} < 19$ mm), with the minimum corresponding to the peak magnitude.

Referring to figure 2.14 (c), the intensity of the ring emission increases from its establishment at 1.05 ms until its maximum at 1.87 ms. The smoothness of the maximum suggests the attainment of a stable population of light-emitting species for that condition, namely for that plasma current, as indicated by the antenna current characteristic frequency. Following the maximum, the emission intensity decreases steadily, in step with the decreasing characteristic frequency and therefore plasma current. Once the mode transitions from inductive to capacitive at 2.65 ms, the rate of decrease for the emission intensity increases. This suggests that, for the period between 1.87 ms and

Figure 2.11: Emission intensity plotted against radial position at different times for an argon-nitrogen mixture at 4 kV anode potential. The first plot is the mean over time; subsequent plots are instants in time corresponding to: minimum total emission, stabilisation of the ring emission, and maximum total emission.

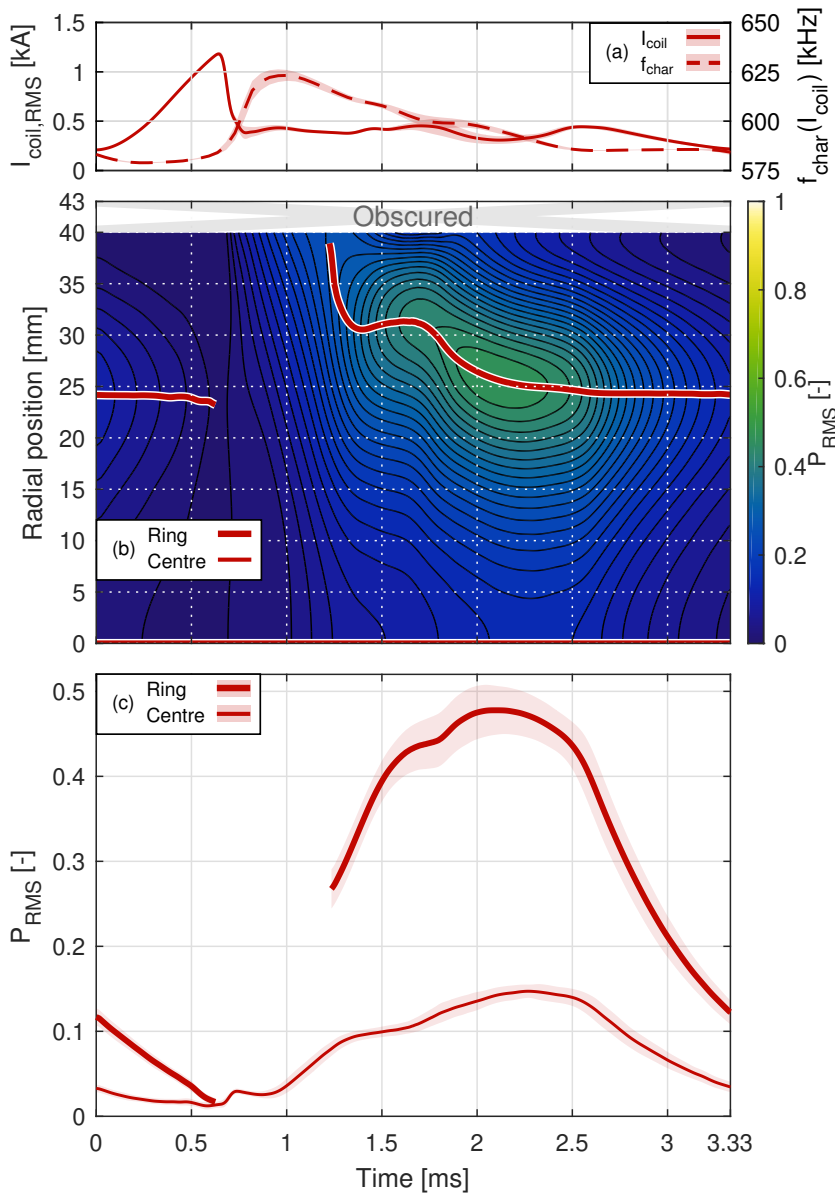
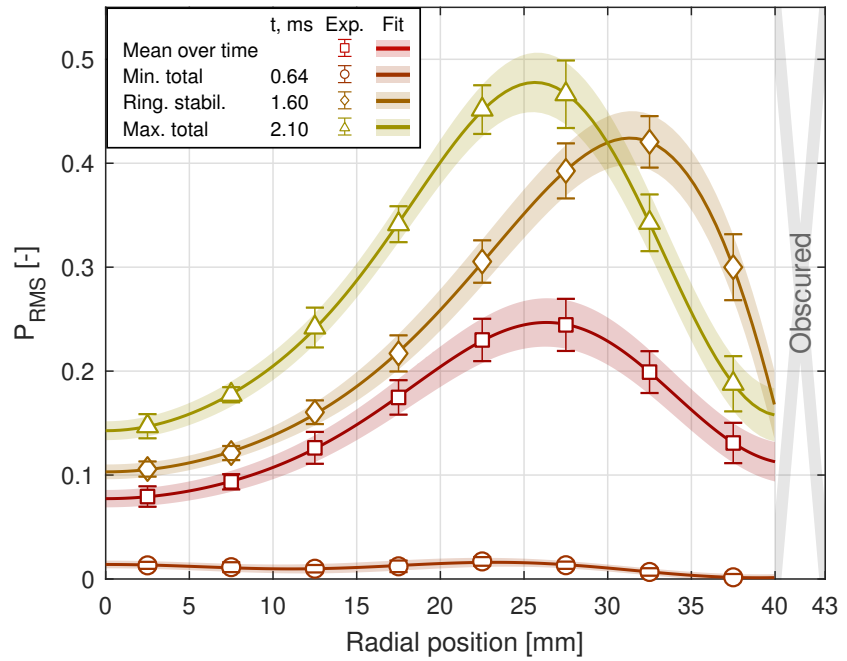


Figure 2.12: The radial and temporal distribution of emission intensity for an argon-nitrogen mixture at 4 kV anode potential. The antenna current and characteristic frequency are shown again for reference (a). The radial and temporal distribution is shown in (b), with the location of the maximum ring emission shown as a thick line, and the centre-line as a thin line. The magnitudes under these lines are plotted in (c) against time.

2 Transient behaviour

2.65 ms, the ring emission intensity represents a steady condition for each plasma current value in that period.

With these spatially-resolved data, the light emission profile in figure 2.8 can be explained as the sum of a central emission and a ring emission. The left skew of the overall emission is then seen as the sum of the left-skewed central emission and the no-skew ring emission. The profile of the ring emission is more comparable with the overall profile for the argon-nitrogen case. In other words, without the central emission, the argon-oxygen and argon-nitrogen cases are similar in most respects. As discussed in the previous section, the antenna current, magnetic field strength, and characteristic frequency profiles for the argon-oxygen and argon-nitrogen cases are nearly identical, therefore, the existence or non-existence of the central emission under these conditions is likely to be a result of the different propellant mixtures. Molecular nitrogen has higher dissociation and ionisation energies than molecular oxygen, which could explain why the central emission is seen at lower anode potential for argon-oxygen, compared with argon-nitrogen.

In this section the spatially-resolved datasets revealed the changing δ_{vis} over individual discharge cycles. In the case of argon-oxygen, it also revealed the existence of a central emission phenomenon, possibly the result of a strong alpha-capacitive coupling. Neither phenomenon is evident when considering the time-averaged data alone.

2.4 Conclusion

The simultaneous measurement of the antenna current, radially-resolved light emission, and radially-resolved axial magnetic field strength, at a sampling frequency sufficient to resolve the discharge cycle and driving frequency, is considered as a new, non-intrusive experimental technique to assess the discharge, the discharge modes and the discharge behaviour of an inductive plasma generator. The transition from capacitive to inductive-dominated coupling can be clearly identified by a sharp decrease in the antenna current ($\approx 50\%$) and a sharp increase in the characteristic frequency of the antenna current ($\approx 6\%$) in each 3.33 ms cycle. The characteristic frequency changes due to the formation of an azimuthal plasma current (inductive coupling) and gives some qualitative insight into the magnitude of that current and the resulting secondary effects that, for example, lead to both the reduction of the primary current as well as the shift of inductance. Measurements of the axial magnetic field strength match remarkably well to a simple analysis of the field induced by the antenna current without considering the plasma current. This suggests that the plasma current is localised in the downstream region.

Photodiode measurements show that the light emission starts to increase at the time that the characteristic frequency deviates (formation of plasma current), and peaks after the frequency does, indicating the delay between the power deposition and the emis-

Figure 2.13: Emission intensity plotted against radial position at different times for an argon-oxygen mixture at 4 kV anode potential. The first plot is the mean over time; subsequent plots are instants in time corresponding to: minimum total emission, maximum central emission, maximum ring emission, and stabilisation of the ring emission after shifting inwards.

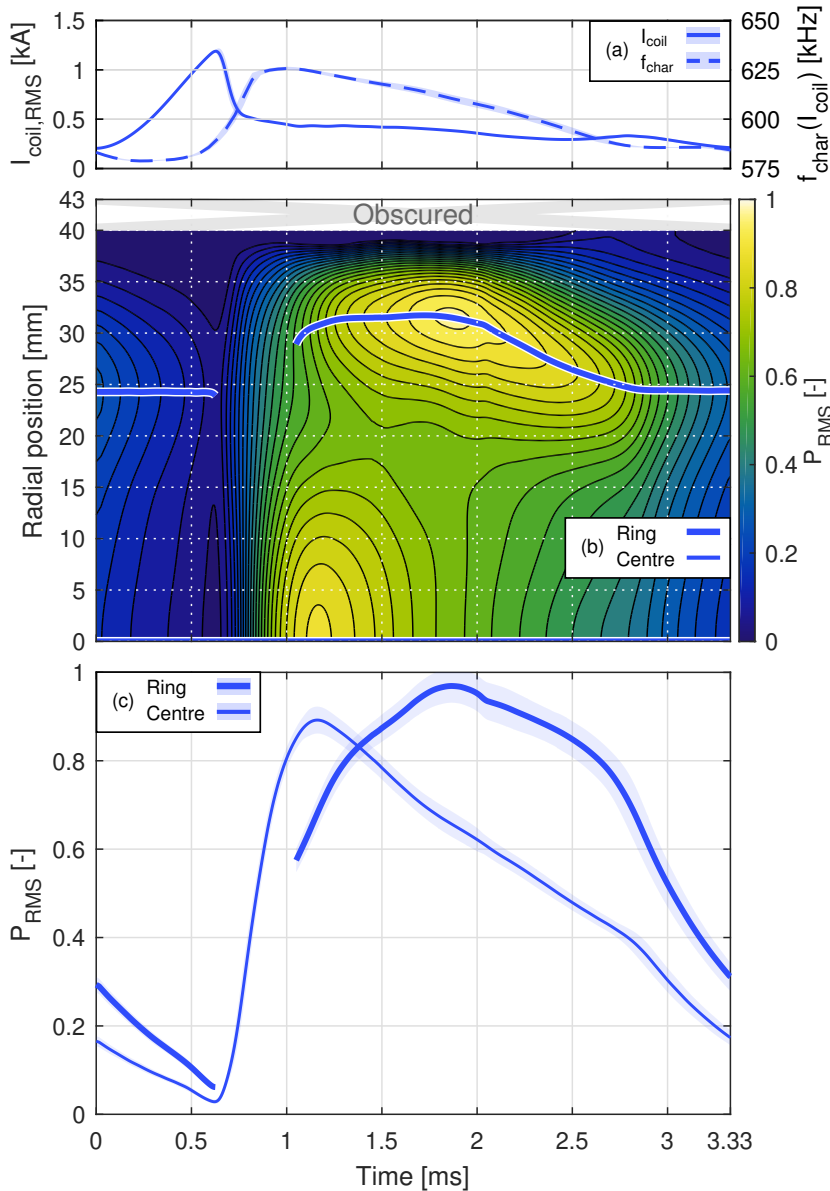
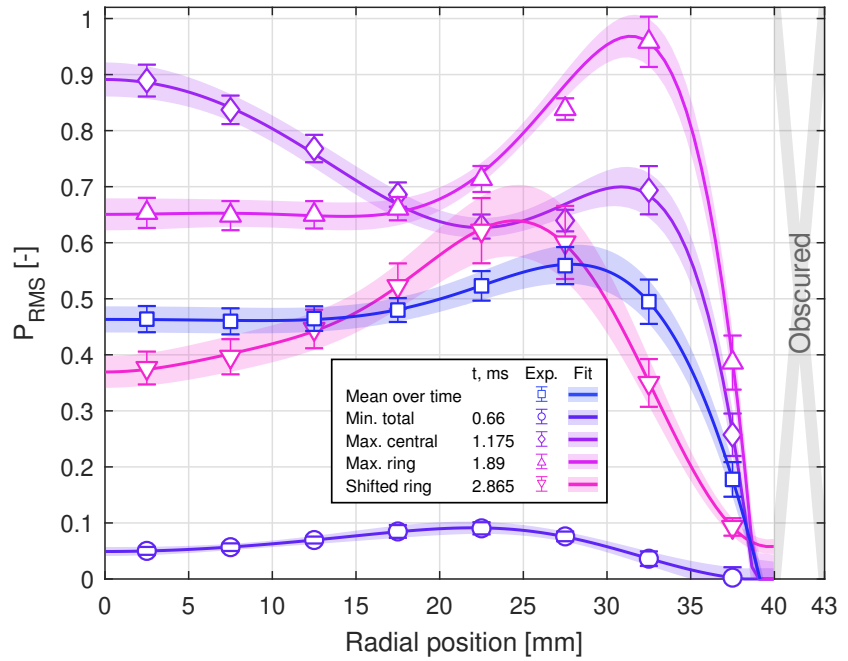


Figure 2.14: The radial and temporal distribution of emission intensity for an argon-oxygen mixture at 4 kV anode potential. The antenna current and characteristic frequency are shown again for reference (a). The radial and temporal distribution is shown in (b), with the location of the maximum ring emission shown as a thick line, and the centre-line as a thin line. The magnitudes under these lines are plotted in (c) against time.

2 *Transient behaviour*

sion caused by electrons dropping to lower energy states. Furthermore, the radially-resolved photodiode measurements show the depth at which maximum light emission occurs, δ_{vis} , and its evolution over time. For the nitrogen case, it is fairly consistent at 6.5 mm, for argon-oxygen it initially stabilises at 12 mm and later at 17.5 mm, and for argon-nitrogen it varies between 11 mm and 19 mm. The effect of adding argon to nitrogen is pronounced and produces a more prolonged period of inductive coupling and consequently a greater emission intensity. While alternative techniques such as phase-resolved optical emission spectroscopy (PROES) can certainly give more detailed insight into plasma parameters, it cannot tolerate mixtures as well as the method presented here. In the context of space propulsion mixtures are being investigated as a means to improve the performance of gases captured from the space environment.

The transient light emission profiles reveal several features that were hidden in the time-averaged profiles; namely, the existence of a central emission peak in the argon-oxygen case, and the changing location of the ring emission. Given the range of phenomena displayed in a single discharge cycle, such as capacitive coupling, the central emission (possibly a parallel alpha-capacitive coupling) and varying degrees of inductive ring emissions, it is clear that the discharge cannot be treated as a steady process using time-averaged values. This is also of concern for the parameters that can be measured in the plasma jet, an aspect that significantly increases the value of these results. Conventional plasma modelling approaches use a steady assumption, such that time-variance does not need to be considered, significantly reducing the model complexity at the cost of neglecting the transient phenomena. The experimental technique presented here provides evidence for the importance of transient modelling, as well as a method for collecting the data needed to build such a model.

Acknowledgements

The authors would like to thank the German Research Foundation for their financial contributions to the experimental campaign under Project HE 4563/3-1.

This research is supported by an Australian Government Research Training Program (RTP) Scholarship.

Research undertaken for this report has been assisted with a grant from the Sir Ross and Sir Keith Smith Fund (Smith Fund) (www.smithfund.org.au). The support is acknowledged and greatly appreciated. The Smith Fund, by providing funding for this project, does not verify the accuracy of any findings or any representations contained in it. Any reliance on the findings in any written report or information provided to you should be based solely on your own assessment and conclusions. The Smith Fund does not accept any responsibility or liability from any person, company or entity that may have relied on any written report or representations contained in this report if that person, company or entity suffers any loss (financial or otherwise) as a result.

References

- Anih, S., Pagan, A. S., Koch, H., Martinez, P., Laufer, R., & Herdrich, G. (2019). Waste for Energy and Volume Recovery (WEVR) using Inductively Heated Plasma Generator Samuel. *70th International Astronautical Congress*, IAC-19-B3, 7, 8, x54017.
- Auweter-Kurtz, M., & Wegmann, T. (1999). Overview of IRS plasma wind tunnel facilities. *RTO AVT Course on "Measurement Techniques for High Enthalpy and Plasma Flows"*.
- Bathgate, S. N., Bilek, M. M., & McKenzie, D. R. (2017). Electrodeless plasma thrusters for spacecraft: A review. *Plasma Science and Technology*, 19(8). <https://doi.org/10.1088/2058-6272/aa71fe>
- Böhrk, H., & Auweter-Kurtz, M. (2006a). Preliminary Results of TIHTUS Operation. *42nd AIAA/ASME/SAE/ASEE Joint Propulsion Conference & Exhibit*, AIAA 2006-5158. <https://doi.org/10.2514/6.2006-5158>
- Böhrk, H., & Auweter-Kurtz, M. (2006b). High Power Space Propulsion System TIHTUS - an Overview. *57th International Astronautical Congress*, IAC-06-C4.P.4.06. <https://doi.org/10.2514/6.IAC-06-C4.P.4.06>
- Chadwick, A. R. (2017). *Performance of Alternative Propellants in an Inductive Electric Propulsion System* (Ph.D. Thesis). The University of Adelaide. <http://hdl.handle.net/2440/119192>
- Chadwick, A. R., Herdrich, G., Kim, M., & Dally, B. B. (2016). Transient electromagnetic behaviour in inductive oxygen and argon-oxygen plasmas. *Plasma Sources Science and Technology*, 25(6). <https://doi.org/10.1088/0963-0252/25/6/065025>

- Chadwick, A. R., Janocha, T., Herdrich, G., Dally, B. B., & Kim, M. (2018). Wall Temperature Measurements Within a High-Power Inductive Plasma Discharge. *IEEE Transactions on Plasma Science*, 46(4), 1040–1046. <https://doi.org/10.1109/TPS.2018.2805473>
- Cunge, G., Crowley, B., Vender, D., & Turner, M. M. (1999). Characterization of the E to H transition in a pulsed inductively coupled plasma discharge with internal coil geometry: bi-stability and hysteresis. *Plasma Sources Science and Technology*, 8(4), 576–586. <https://doi.org/10.1088/0963-0252/8/4/309>
- Derby, N., & Olbert, S. (2010). Cylindrical Magnets and Ideal Solenoids. *American Journal of Physics*, 78(3), 229–235. <https://doi.org/10.1119/1.3256157>
- Godyak, V. A. (2003). Plasma phenomena in inductive discharges. *Plasma Physics and Controlled Fusion*, 45(12A), A399–A424. <https://doi.org/10.1088/0741-3335/45/12A/026>
- Godyak, V. A., & Khanneh, A. S. (1986). Ion Bombardment Secondary Electron Maintenance of Steady RF Discharge. *IEEE Transactions on Plasma Science*, 14(2), 112–123. <https://doi.org/10.1109/TPS.1986.4316513>
- Godyak, V. A., Piejak, R. B., & Alexandrovich, B. M. (2002). Electron energy distribution function measurements and plasma parameters in inductively coupled argon plasma. *Plasma Sources Science and Technology*, 11(4), 525–543. <https://doi.org/10.1088/0963-0252/11/4/320>
- Herdrich, G. (2004). *Construction, qualification and characterisation of an inductively heated plasma wind-tunnel system to simulate atmospheric entry (Aufbau, Qualifikation und Charakterisierung einer induktiv beheizten Plasmawindkanalanlage zur Simulation atmosphärischer)* (Ph.D. Thesis). Universität Stuttgart.
- Herdrich, G., & Auweter-Kurtz, M. (2006). Inductively heated plasma sources for technical applications. *Vacuum*, 80(11-12), 1138–1143. <https://doi.org/10.1016/j.vacuum.2006.01.044>
- Herdrich, G., Bauder, U., Boxberger, A., Gabrielli, R. A., Lau, M., Petkow, D., Pfeiffer, M., Syring, C., & Fasoulas, S. (2013). Advanced plasma (propulsion) concepts at IRS. *Vacuum*, 88(1), 36–41. <https://doi.org/10.1016/j.vacuum.2012.02.032>
- Herdrich, G., Chadwick, A. R., Dally, B. B., & Kim, M. (2015). Further Development of the TIHTUS Test Facility at IRS. *Joint Conference of 30th International Symposium on Space Technology and Science, 34th International Electric Propulsion Conference and 6th Nano-satellite Symposium*, IEPC–2015–90252/ISTS–2015–b–90252. http://electricrocket.org/IEPC/IEPC-2015-389%7B%5C_%7DISTS-2015-b-389.pdf
- Herdrich, G., Fertig, M., & Löhle, S. (2009). Experimental Simulation of High Enthalpy Planetary Entries. *The Open Plasma Physics Journal*, 2, 150–164. <https://doi.org/10.2174/1876534300902010150>
- Herdrich, G., & Petkow, D. (2008). High-enthalpy, water-cooled and thin-walled ICP sources characterization and MHD optimization. *Journal of Plasma Physics*, 74(3), 391–429. <https://doi.org/10.1017/S0022377807006927>

- Karrer, N., Hofer-Noser, P., Herdrich, G., & Auweter-Kurtz, M. (2003). Isolated current probe for continuous monitoring of AC currents of high amplitude and high frequency. *European Power Electronics Conference*.
- Karrer, N., Hofer-Noser, P., & Henrard, D. (1999). HOKA: a new isolated current measuring principle and its features. *Conference Record of the 1999 IEEE Industry Applications Conference. Thirty-Forth IAS Annual Meeting (Cat. No.99CH36370)*, 3, 2121–2128. <https://doi.org/10.1109/IAS.1999.806028>
- Kaupe, J., Coenen, D., & Mitic, S. (2018). Phase-resolved optical emission spectroscopy of a transient plasma created by a low-pressure dielectric barrier discharge jet. *Plasma Sources Science and Technology*, 27(10). <https://doi.org/10.1088/1361-6595/aada9e>
- Kaupe, J., Riedl, P., Coenen, D., & Mitic, S. (2019). Temporal evolution of electron density and temperature in low pressure transient Ar/N₂ plasmas estimated by optical emission spectroscopy. *Plasma Sources Science and Technology*, 28(6). <https://doi.org/10.1088/1361-6595/ab252d>
- Kralkina, E. A., Nekliudova, P. A., Pavlov, V. B., Petrov, A. K., & Vavilin, K. V. (2017). Features of RF low-pressure discharge with inductive and capacitive channels. *Plasma Sources Science and Technology*, 26(5), 055006. <https://doi.org/10.1088/1361-6595/aa61e6>
- Kralkina, E. A., Nekliudova, P., Pavlov, V., Vavilin, K., Zadiriev, I., & Zhao, C. (2020). Experimental study of a low-pressure hybrid RF discharge. *Plasma Science and Technology*, 22(5), 055405. <https://doi.org/10.1088/2058-6272/ab69bd>
- Kralkina, E. A., Rukhadze, A. A., Pavlov, V. B., Vavilin, K. V., Nekliudova, P. A., Petrov, A. K., & Alexandrov, A. F. (2016). RF power absorption by plasma of a low-pressure inductive discharge. *Plasma Sources Science and Technology*, 25(1), 015016. <https://doi.org/10.1088/0963-0252/25/1/015016>
- Lieberman, M. A., & Lichtenberg, A. J. (2005). *Principles of Plasma Discharges and Materials Processing*. John Wiley & Sons, Inc. <https://doi.org/10.1002/0471724254>
- Loehle, S., Zander, F., Eberhart, M., Hermann, T., Meindl, A., Massuti-Ballester, B., Leiser, D., Hufgard, F., Pagan, A. S., Herdrich, G., & Fasoulas, S. (2022). Assessment of high enthalpy flow conditions for re-entry aerothermodynamics in the plasma wind tunnel facilities at IRS. *CEAS Space Journal*, 14(2), 395–406. <https://doi.org/10.1007/s12567-021-00396-y>
- Manente, M., Trezzolani, F., Magarotto, M., Fantino, E., Selmo, A., Bellomo, N., Toson, E., & Pavarin, D. (2019). REGULUS: A propulsion platform to boost small satellite missions. *Acta Astronautica*, 157(December 2018), 241–249. <https://doi.org/10.1016/j.actaastro.2018.12.022>
- Massuti-Ballester, B., Marynowski, T., & Herdrich, G. (2013). New Inductively Heated Plasma Source IPG7. *Frontier of Applied Plasma Technology*, 6(2).

- Navarro-Cavallé, J., Wijnen, M., Fajardo, P., & Ahedo, E. (2018). Experimental characterization of a 1 kW Helicon Plasma Thruster. *Vacuum*, *149*, 69–73. <https://doi.org/10.1016/j.vacuum.2017.11.036>
- Projekt Elektronik. (2016). Teslameter FM 302 for AS-active-probes. <https://www.projekt-elektronik.com/wp-content/uploads/sites/3/2018/03/data-sheet-Teslameter-FM-302-0204-18.pdf>
- Romano, F., Herdrich, G., Roberts, P. C. E., Boxberger, A., Chan, Y.-A., Traub, C., Fasoulas, S., Smith, K., Edmondson, S., Haigh, S., Crisp, N., Abrao Oiko, V. T., Lyons, R., Worrall, S. D., Livadiotti, S., Huyton, C., Sinpetru, L., Outlaw, R., Becedas, J., ... Pavarin, D. (2019). Inductive Plasma Thruster (IPT) for an Atmosphere-Breathing Electric Propulsion System: Design and Set in Operation. *36th International Electric Propulsion Conference, IEPC-2019-A-488*. <http://electricrocket.org/2019/488.pdf>
- Romano, F., Massuti-Ballester, B., Binder, T., Herdrich, G., Fasoulas, S., & Schönherr, T. (2018). System analysis and test-bed for an atmosphere-breathing electric propulsion system using an inductive plasma thruster. *Acta Astronautica*, *147*, 114–126. <https://doi.org/10.1016/j.actaastro.2018.03.031>
- Schulze, J., Schüngel, E., Donkó, Z., Luggenhölscher, D., & Czarnetzki, U. (2010). Phase resolved optical emission spectroscopy: A non-intrusive diagnostic to study electron dynamics in capacitive radio frequency discharges. *Journal of Physics D: Applied Physics*, *43*(12). <https://doi.org/10.1088/0022-3727/43/12/124016>
- Sou, H., Takao, Y., Noutsuka, T., Mori, Y., Uemura, K., & Nakashima, H. (2000). Study of plasma propulsion system with RF heating. *Vacuum*, *59*(1), 73–79. [https://doi.org/10.1016/S0042-207X\(00\)00256-6](https://doi.org/10.1016/S0042-207X(00)00256-6)
- ThorLabs. (2005). DET210 - High-speed Silicon Detector. https://www.thorlabs.com/drawings/c211fb03837ae854-5BC544DD-D335-5B5D-EDE39DAB8DC2D912/DET210%7B%5C_%7DM-SpecSheet.pdf
- Turner, M. M., & Lieberman, M. A. (1999). Hysteresis and the E-to-H transition in radiofrequency inductive discharges. *Plasma Sources Science and Technology*, *8*(2), 313–324. <https://doi.org/10.1088/0963-0252/8/2/312>
- Wang, Y., Chen, J., Wang, Y., & Xiong, W. (2018). The influence of oxygen ratio on the plasma parameters of argon RF inductively coupled discharge. *Vacuum*, *149*, 291–296. <https://doi.org/10.1016/j.vacuum.2018.01.008>
- Zaka-ul-Islam, M., O'Connell, D., Graham, W. G., & Gans, T. (2015). Electron dynamics and frequency coupling in a radio-frequency capacitively biased planar coil inductively coupled plasma system. *Plasma Sources Science and Technology*, *24*(4). <https://doi.org/10.1088/0963-0252/24/4/044007>



Power efficiency estimation

Power efficiency estimation of an inductive plasma generator using propellant mixtures of oxygen, carbon-dioxide and argon

The second article is a deeper investigation into antenna current measurements taken for oxygen, carbon dioxide and mixtures of both with argon, at various input powers and flow rates, along with how they relate to propulsion figures of merit such as power efficiencies. To quantify the amplitude and frequency shifts of the antenna current, two quantities are defined—the ‘inductive duty cycle’ and the ‘inductive frequency shift’. These quantities are then compared with system-level power efficiencies to understand how the antenna current behaviour is linked to the propulsion figures of merit such as thermal efficiency. In particular, high thermal efficiencies (approximately 84 %) are achieved under high ‘inductive frequency shift’ conditions.

Statement of authorship

Title Power efficiency estimation of an inductive plasma generator using propellant mixtures of oxygen, carbon-dioxide and argon

Publication Published: Georg, R., Chadwick, A. R., Dally, B. B., & Herdrich, G. (2021). Power efficiency estimation of an inductive plasma generator using propellant mixtures of oxygen, carbon-dioxide and argon. *Acta Astronautica*, 179(November 2020), 536–545. <https://doi.org/10.1016/j.actaastro.2020.11.020>

Principal author contribution

This paper reports on original research I conducted during the period of my Higher Degree by Research candidature and is not subject to any obligations or contractual agreements with a third party that would constrain its inclusion in this thesis. I am the primary author of this paper.

Principal author R. Georg

Contribution I contributed approximately 80 % to the authorship of this paper. Excluding the experimental component, I was primarily responsible for the conception of the paper. I drafted the manuscript including all tables and figures. I conducted the majority of the analysis. I acted as the corresponding author.

My contribution satisfies all authorship criteria of the *Australian Code for the Responsible Conduct of Research*.

_____ 8 July 2022

Co-author contributions

By signing the statement of authorship, each co-author certifies that: i. the candidate's stated contribution to the publication is accurate (as detailed above); ii. permission is granted for the candidate to include the publication in the thesis; and iii. the sum of all co-author contributions is equal to 100 % less the candidate's stated contribution.

Co-author A. R. Chadwick

Contribution Collected the experimental data that is analysed in the paper. Provided knowledge and assisted with analysis and revising the manuscript. Involved in the conception of the paper, particularly the experimental component.

_____ 8 July 2022

Co-author B. B. Dally

Contribution Provided knowledge and assisted with analysis and revising the manuscript.

_____ 8 July 2022

Co-author G. Herdrich

Contribution Provided knowledge and assisted with analysis and revising the manuscript. Involved in the conception of the paper, particularly the experimental component.

_____ 8 July 2022

Abstract

A promising aspect of inductive plasma generators for space propulsion applications is their electrodeless nature that leads to a high propellant compatibility and opens the door to in-situ resource utilisation propellants. To further develop inductive plasma generators as a space propulsion technology it is important to understand the relationship between system inputs (e.g. input power and propellant material) and system outputs (e.g. power efficiencies) to aid design and control. In this work, methodologies are developed for non-intrusively assessing the inductive coupling from antenna current measurements in terms of the ‘instantaneous ignition power’, the ‘inductive duty cycle’ and the ‘inductive frequency shift’. Experimental results are presented for IPG7, a high-power (up to 180 kW) 5.5-turn helical antenna inductive plasma generator. Potential in-situ resource utilisation materials oxygen and carbon-dioxide, and their respective mixtures with argon, are assessed in terms of their inductive coupling characteristics and resulting power efficiencies. Oxygen is shown to be an attractive propellant material, especially when supplemented with argon. In particular, high thermal efficiency ($\sim 84\%$) can be achieved at high input powers. A basis is provided for understanding the power efficiencies of an inductive plasma generator in terms of non-intrusive antenna current measurements, to aid power supply sizing and to develop monitoring and control techniques for thruster applications.

3.1 Introduction

The ongoing development of electrodeless electric propulsion technology offers great promise for the expansion of human activity in space. The separation of electrical components from the high-enthalpy propellant flow (hence ‘electrodeless’) strongly mitigates the life-limiting factor of erosion and allows the use of a variety of propellants. Advanced electrodeless propulsion systems are under development at the University of Stuttgart’s Institute for Space Systems (IRS) for applications such as in-situ resource utilisation (ISRU) including atmosphere-breathing electric propulsion (ABEP). In particular, IPT (radiofrequency helicon-based inductive plasma thruster) is in active development for ABEP applications within the Discoverer project, employing technologies such as optimised antenna design and respective resonances to enhance both power coupling and propellant acceleration (Romano et al., 2018; Romano et al., 2020). A parallel program focuses on developing a basic understanding of the dynamic power coupling modes and the impact of variations in propellant blends (Chadwick et al., 2016; Chadwick et al., 2020; Georg et al., 2020 (chapter 2)), of which the work presented here is the latest part. Conventional electric technologies, such as gridded ion thrusters and Hall-effect thrusters, typically rely on the less-reactive noble gases to par-

3 Power efficiency estimation

tially mitigate the factor of erosion (Brown & Walker, 2020), making them unsuitable for ISRU. Potential ISRU materials that could be used as propellants include oxygen, water, carbon dioxide, or syngas from waste gasification and pyrolysis processes (Anih et al., 2019). The development of a thruster which can ingest these materials with minimal erosion and with desirable performance characteristics would open the door to ‘refuelling’ with material collected in space (ISRU), and/or continuous operation in very low orbit (ABEP). Both concepts represent new capabilities for human space activity.

There are numerous groups working on advanced electric propulsion technologies as outlined in a recent review paper by Levchenko et al. (2020). Electrodeless propulsion technologies form a prominent subset of these, and are outlined in greater detail in another review paper by Bathgate et al. (2017). One electrodeless technology that continues to receive a great deal of attention in the literature is the inductive plasma generator (IPG). The inductive plasma generator gets its name from the inductive coupling that occurs when the radiofrequency antenna current induces an azimuthal current in the plasma. This can be understood by analogy with an electrical transformer, where the antenna forms the primary winding and the plasma forms the second winding (single loop). In this regime, power is transferred to the plasma effectively. Inductive coupling occurs at high input powers; at low powers, capacitive coupling is dominant. The transition between the two regimes exhibits hysteresis (Turner & Lieberman, 1999) and is sensitive to many factors including the matching conditions (Cunge et al., 1999), plasma geometry, antenna geometry, pressure and plasma parameters (active and equivalent plasma resistances) (Kralkina et al., 2017; Kralkina et al., 2020). Further complicating the matter, the two coupling modes are not mutually exclusive and it possible to have varying degrees of parallel capacitive and inductive coupling. Therefore it becomes important to not only assess the dominant regime, but also quantify its dominance. In the context of space propulsion, establishing and maintaining a strong inductive coupling is important to maximise the power transfer into the propellant in an IPG.

Including helicon plasma sources as a special case of IPG, there are numerous groups working on developing this technology for space propulsion (Romano et al., 2020; Sou et al., 2000; Herdrich et al., 2013; Isayama et al., 2018; Navarro-Cavallé et al., 2018; Vitucci, 2019; Manente et al., 2019; Takahashi, 2019; Tsifakis et al., 2020). In addition to the radiofrequency excitation, helicon sources also use an applied magnetic field to establish the necessary boundary conditions for the formation of helicon waves within the plasma discharge. Several mechanisms have been demonstrated or proposed for the acceleration of the quasi-neutral plasma discharge, three of which are mentioned here. Firstly, the discharge can undergo gas-dynamic expansion, for example through a physical de Laval nozzle. Secondly, diverging magnetic field lines (such as the applied magnetic field of a helicon source) can produce a ‘magnetic nozzle’ effect; key benefits

are the lack of erosion and the ability to adjust the nozzle in-flight when compared to the physical alternative (Merino & Ahedo, 2016). Thirdly, an $E \times B$ drift velocity can be produced with the necessary field configuration (Kaganovich et al., 2020). Each of these mechanisms has an equal effect on electrons and ions, therefore a neutralising electron beam is not needed. Furthermore, the mechanisms are not necessarily mutually exclusive, for example, the previously mentioned IPT project at IRS employs both magnetic nozzle and $E \times B$ drift velocity effects (Romano et al., 2018; Romano et al., 2020).

Despite propellant-flexibility being a key motivator for electrodeless propulsion, to-date there has been limited work on studying and comparing the performance of different propellant compositions in IPGs. Charles et al. investigates the effect of molecular propellants by measuring the exhaust velocities over pressure for N_2 , CH_4 , NH_3 and N_2O in their helicon double layer thruster (HDLT) (Charles et al., 2008); these species were chosen because of their different molecular structures rather than any relevancy to ISRU. Chadwick et al. reported thrust measurements and associated figures of merit over input power for O_2 , N_2 , CO_2 and respective mixtures with Ar in a high-powered IPG (Chadwick et al., 2020); the base species were chosen for their relevance for ISRU while the argon mixtures were chosen to augment their propulsive properties. This work showed promising results for the argon mixtures including a synergistic behaviour between the two components due to the low ionisation energy of argon and the high thermal conductivity of the molecular component.

This work presents several figures of merit over a range of conditions and propellants for an IPG as a potential space propulsion technology. When interpreting these figures, it is important to understand their role in the spacecraft design process. Maximisation of a spacecraft's payload mass fraction ($m_{PL}^* = m_{PL}/m_{total\ initial}$) is typically the primary design goal when selecting a propulsion system. The rocket equation can be reformulated to yield an expression for the payload mass fraction

$$m_{PL}^* = \left(1 + v_e^{*2}\right) \exp\left(-\Delta V^*/v_e^*\right) - v_e^{*2} \quad (3.1)$$

where $v_e^* = v_e/v_c$ is the normalised exhaust velocity and $\Delta V^* = \Delta V/v_c$ is the normalised velocity increment (Humble et al., 1995). The normalising quantity is the 'energy characteristic velocity', defined as

$$v_c = \sqrt{2\eta_F \xi \tau} \quad (3.2)$$

where $\eta_F = P_{jet}/P_{input}$ is the thrust efficiency, $\xi = P_{input}/m_W$ is the power-to-mass ratio of the propulsion system including electrical systems and τ is the propulsion duration.

It can be seen from equations (3.1) and (3.2) that selecting a propulsion system is a multidisciplinary problem depending on propulsion parameters v_e , η_F and ξ , and

3 Power efficiency estimation

mission parameters m_{PL}^* , ΔV and τ . Moreover, these parameters are not fully independent; for example, v_e typically increases with η_F and ξ , and the required combination of ΔV and τ will change depending on the chosen trajectory, which is affected by the propulsion parameters. The interconnected nature of these parameters means that a propulsion system should have a range of possible operating conditions so that a range of values for v_e , η_F and ξ are available. This would make the propulsion system applicable to a greater number of mission specifications and also more tolerant to iterative design changes. Therefore, in the development of new propulsion technologies it is important to assess a range of operating conditions rather than simply the maximum case. Furthermore, an understanding of the system inputs (propellant choice, flow rate, applied power) that produce desirable operating conditions is needed.

The majority of electrodeless electric propulsion technologies in development can be considered as low-power devices, producing thrusts in the order of milli-Newtons (mN) (Bathgate et al., 2017). The choice to target low powers is primarily motivated by a reduction of development costs and complexity, and a desire to target small satellite applications. According to equation (3.2), increasing the propulsion duration τ has the same effect as increasing the jet-power-to-mass ratio $\eta_F \times \xi$. The latter is more difficult from a technical point of view, which favours low-power devices with long propulsion durations. One application for high-power electrodeless electric propulsion is for interplanetary missions where a reduction of travel time is valuable, the spacecraft mass is large, and propellant material can be restocked (e.g. CO_2 from crew or material collected from destination). An additional application is provided by ABEP, where the thrust must be sufficient to offset the atmospheric drag.

Typically, intrusive methods are used to assess the internal (e.g. Langmuir probe) and external (e.g. baffle plate) parameters of an IPG. However, their intrusive nature means that the plasma plume is disturbed, and they could not be used in-flight for monitoring or control. Therefore, the development of non-intrusive methods suitable for use in-flight is important for the development of this technology, particularly if these methods can identify regime transitions within the IPG. Optical emission spectroscopy and laser-induced fluorescence are well-established non-intrusive methods, however, they are highly dependent on the particular propellant gas used, and do not handle gas mixtures well. A non-intrusive technique was proposed by Chadwick (2017) for a high-powered IPG with oxygen and argon-oxygen mixtures using high-sampling-frequency measurements of the antenna current which helped distinguish transient regime transitions. A follow-on work from Georg et al. (2020) (chapter 2) used the same technique in tandem with time- and radially-resolved measurements of light emission, another non-intrusive method, for nitrogen, argon-nitrogen and argon-oxygen propellant mixtures. Important features of this technique are its low cost, its relative simplicity, and its ability to be used with various propellant mixtures. Furthermore, while this technique has been developed and demonstrated for a high-power IPG, it is in principle equally

applicable for low-power IPGs as well.

In the present work, the transient antenna current technique is developed further and used specifically to understand the factors contributing to the thrust efficiency. Understanding the relationship between the electrical systems and the propulsive output is critical to develop monitoring and control techniques for an IPG-based thruster. Furthermore, by better understanding the electrical requirements of the system, it becomes possible to more accurately size the power supply and conditioning system, which would also improve the power-to-mass ratio. Note that the power in this ratio corresponds to a useful operating condition rather than simply the maximum output of the power supply. Potential ISRU materials oxygen, carbon-dioxide and respective mixtures with argon are assessed in terms of their inductive coupling characteristics and resulting power efficiencies.

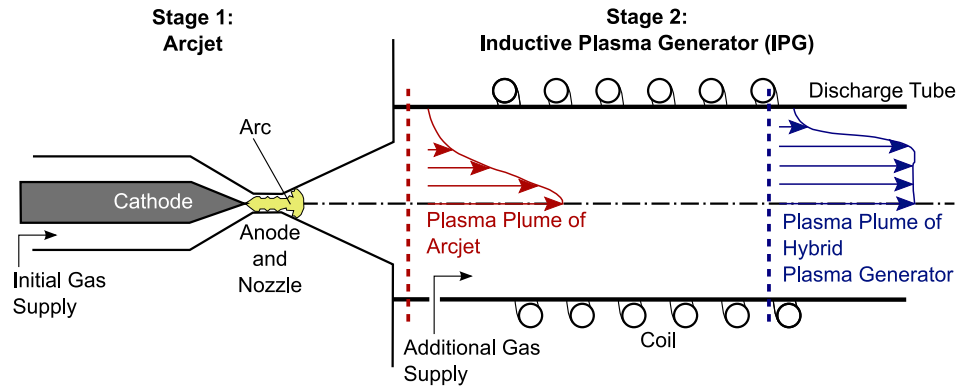
3.2 Methodology

3.2.1 Experimental setup

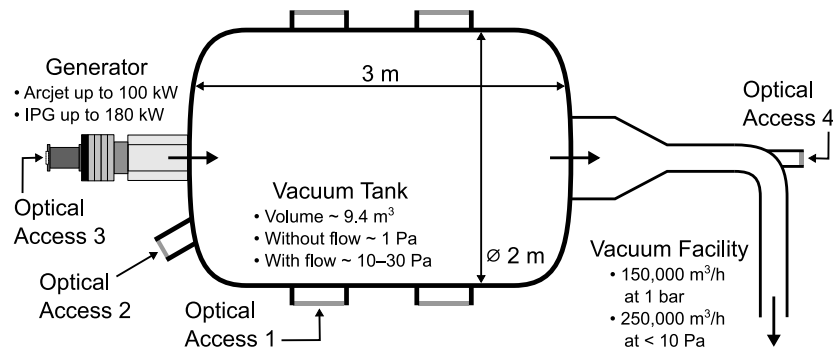
Experimental work was carried out in the TIHTUS (Thermal-Inductive Heated Thruster of the University of Stuttgart) facility of the Institute for Space Systems (IRS), University of Stuttgart, Germany. TITHUS is an experimental thruster consisting of a first-stage arcjet and a second-stage inductive plasma generator (IPG) (Böhrk & Auweter-Kurtz, 2006). The thruster is shown schematically in figure 3.1 (a). The arcjet, HIPARC-W, is fed by an initial gas supply and deposits energy in the central region of the plasma plume. The IPG is fed by this plume and an additional gas supply, and deposits energy in the outer region of the plasma plume. The separation of the two gas supplies means that the arcjet can be fed with non-reactive gases, while the IPG can be fed with reactive gases. Consequently, the propellant flexibility of the IPG is maintained while ensuring low degradation of the arcjet cathode. The IPG can operate under a wide range of powers due to the ionised flow provided by the arcjet. Propellant utilisation is maximised by creating a more uniform distribution of enthalpy in the plasma plume. The test facility is shown schematically in figure 3.1 (b). In this work only the inductive plasma generator stage, IPG7 (Massuti-Ballester et al., 2013), is considered.

Figure 3.2 presents a simplified sectional view of IPG7, which consists of a quartz tube surrounded by a 5.5 turn helical coil antenna. Propellant enters the tube through tangential gas inlets in the injector head. In the absence of additional applied fields, the primary acceleration mechanism of IPG7 is gas-dynamic expansion of the plasma plume as it exits the tube. In a future work a physical de Laval nozzle or magnetic nozzle may be implemented, however, no such nozzle was used in the present work. In the full TIHTUS configuration, the first-stage arcjet would connect to the injector header, however, in this configuration the injector head instead has an axially-aligned window

3 Power efficiency estimation



(a) TIHTUS operating principle (adapted from Böhrk and Auweter-Kurtz (2006)).



(b) TIHTUS test facility (adapted from Herdrich et al. (2015)).

Figure 3.1: TIHTUS (Thermal-Inductive Heated Thruster of the University of Stuttgart).

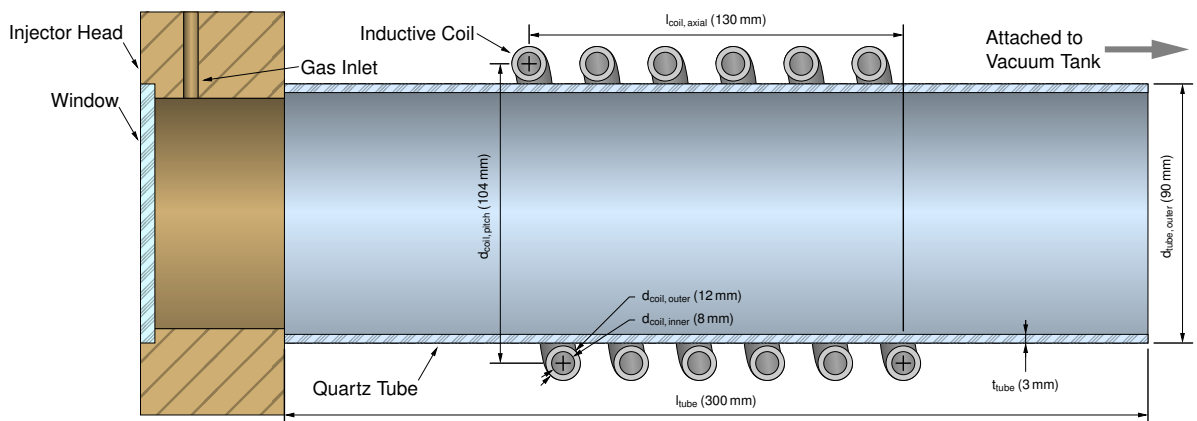


Figure 3.2: Sectional view of IPG7 with dimensions (adapted from Georg et al. (2020) (chapter 2)). A jacket encloses the coil, forming channels for cooling water (not shown).

for optical diagnostics enabling basic investigations related to TIHTUS' second stage (Chadwick, 2017; Georg et al., 2020 (chapter 2)). Two mass flow controllers are used to control and measure the quantities of the propellant components before mixing and injecting into the tube. Due to its high maximum anode power of 180 kW, IPG7 has an enclosing jacket that forms channels through which water flows to cool the tube and, in particular, the coil. Calorimetry is performed on this cooling water to determine the tube cooling power P_{tube} . The plasma jet heating can be assessed by placing a cavity calorimeter (Chadwick et al., 2020; Herdrich & Petkow, 2008) within the vacuum tank to determine the jet power P_{jet} . The position of the calorimeter is chosen to capture the entire plume and ensure that the IPG operation is not affected by back-pressure.

The various powers presented and discussed in this work are related by a number of efficiencies that are defined as follows. The electrical efficiency is defined as $\eta_{\text{elec}} = (P_{\text{jet}} + P_{\text{tube}})/P_{\text{anode}}$, representing the portion of electrical input power that is converted into thermal power in the IPG7 as heating of the discharge or heating of the coil. It is a function mainly of losses in the resonant circuit. The thermal efficiency is defined as $\eta_{\text{therm}} = P_{\text{jet}}/(P_{\text{jet}} + P_{\text{tube}})$, representing the portion of the sum thermal power that exits the IPG in the plume. The nozzle efficiency is defined as $\eta_{\text{nozzle}} = P_{\Delta F}/P_{\text{jet}}$, representing the conversion of plume thermal power into added kinetic power. Added kinetic power is defined as $P_{\Delta F} = (F - F_{\text{cold}})/2\dot{m}$, where F is thrust, F_{cold} is thrust without applied power and \dot{m} is propellant flow rate. Finally, the added thrust efficiency is defined as $\eta_{\Delta F} = \eta_{\text{elec}} \times \eta_{\text{therm}} \times \eta_{\text{nozzle}}$. It is related to the thrust efficiency in equation (3.2) by $\eta_{\Delta F} = \eta_F(1 - 2\alpha + \alpha)^2$ where $\alpha = F_{\text{cold}}/F$. The goal of maximising $\eta_{\Delta F}$ (and therefore η_F) can be achieved by improving the constituent electrical, thermal and nozzle efficiencies.

The antenna coil is driven by a Meissner oscillator (also known as Armstrong oscillator) resonant circuit without matching network, shown in figure 3.3 (left). The transformer model is used to represent the inductively-coupled coil/plasma system (Piejak et al., 1992; Gudmundsson & Lieberman, 1997). The circuit is fed by full-wave rectified facility power at the anode of the triode. The anode potential is set to control the power input to the system. Both the anode current and potential are measured and yield the anode power P_{anode} . The losses in the RS 3300 CJ metal-ceramic triode are estimated as $25\% \times P_{\text{anode}}$ (Herdrich, 2004). An oscillating current i_c passes through the coil, where R_c is the resistance of the coil and its leads, and L_c is its self-inductance. On the plasma side, the plasma current i_p is a loop current that generates self-inductance L_p , and has a resistance R_p and an additional inductance L_e representing the electron inertia. The mutual inductance is defined as $M = k\sqrt{L_c L_p}$, where the coupling coefficient k represents the proportion of flux linkage between the two inductors and satisfies $0 \leq k \leq 1$.

The circuit can be reduced to a lumped element equivalent, shown in figure 3.3

3 Power efficiency estimation

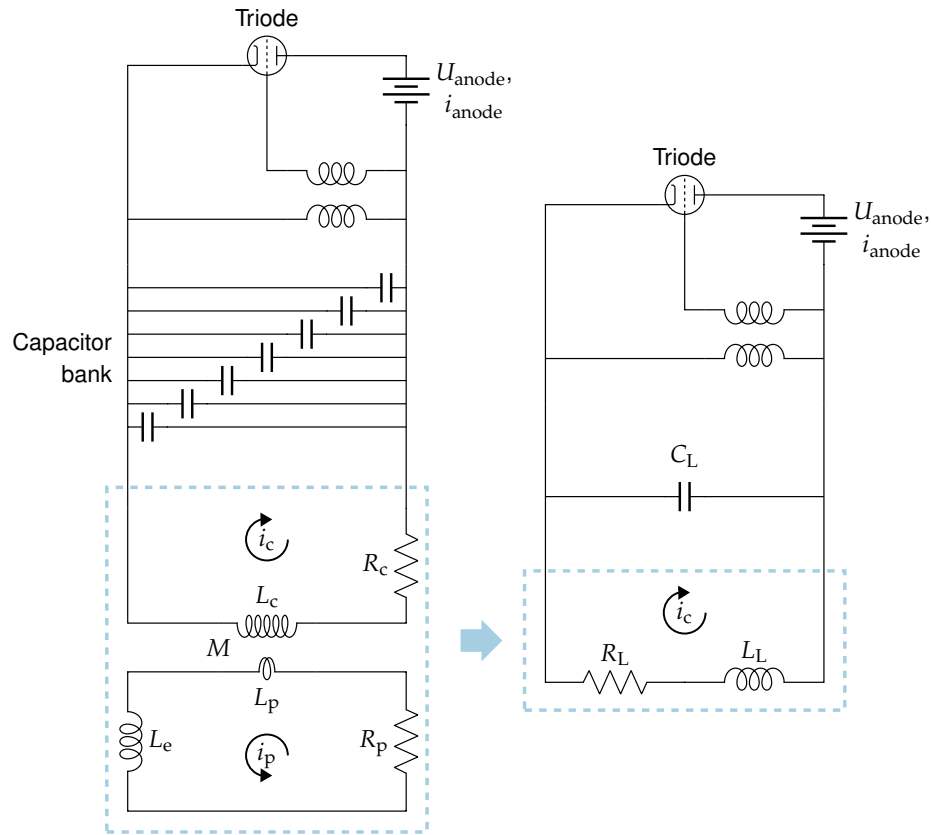


Figure 3.3: Resonant circuit with transformer model of the coil/plasma system (left) and lumped element equivalent circuit (right).

(right), where the characteristic frequency can be approximated by $\omega = 1/\sqrt{L_L C_L}$. Therefore, excluding fixed parameters (the IPG geometry and the capacitor bank), the characteristic frequency is a function only of the geometric and electrical properties of the plasma current. The nominal frequency can be altered by changing the coil geometry and by changing the number of capacitors connected in the capacitor bank (Herdrich & Petkow, 2008); however, in this work both parameters are fixed: a 5.5 turn helical coil and 5×6 nF capacitors were used. Monitoring the transient behaviour of the characteristic frequency can therefore give qualitative insight into the transient behaviour of the plasma current. Nishida *et al.* studied a similar circuit model of the antenna and matching circuit of a 100 kW, 2 MHz IPG, with the aim of matching the driving frequency to the resonant frequency (this differs from IPG7, whose resonant frequency determines the driving frequency) (Nishida *et al.*, 2014). They concluded that, as the electron density increases, the lumped inductance decreases and consequently the resonant frequency increases.

The antenna current is measured via its magnetic field by a Hofer-Noser Karrer

(HOKA) probe designed by Kametech AG (Karrer et al., 1999; Karrer et al., 2003). The probe was selected for its ability to tolerate prolonged exposure to the high current due to its non-ferrous design, and for its high sampling frequency (up to 4 MHz). A fast-Fourier-transform algorithm was used to determine f_{char} , the characteristic frequency of the antenna current.

3.2.2 Measuring inductive coupling

The full-wave rectification of the 50 Hz three-phase facility power results in a 300 Hz modulated direct-current input to the resonant circuit. This modulates the antenna current to the degree that each 3.33 ms cycle forms a discharge cycle in the plasma. A method was developed to collate the cycles for further analysis, outlined in figure 3.4 (a). By applying this method to the antenna current and its characteristic frequency it is possible to distinguish the capacitive and inductive coupling modes within the time-scale of the discharge cycles, as shown in figure 3.4 (b). For a purely capacitive condition, the antenna power resembles as positive-skewed, smooth distribution, while the characteristic frequency is relatively stable and smooth, with a small dip when the antenna power initially increases. For a mixed capacitive/inductive condition, the transition to inductive coupling is marked by a sharp decrease in antenna power and a sharp increase in characteristic frequency (Chadwick et al., 2016; Herdrich & Petkow, 2008; Auweter-Kurtz & Wegmann, 1999).

While the mode transition is seen in both the antenna power and the characteristic frequency, the latter gives a more consistent response across different conditions and is therefore better suited for identifying periods of inductive coupling. By comparing the characteristic frequency curves of a purely capacitive condition and a mixed capacitive/inductive condition it is possible to quantify the degree of inductive coupling in the latter in one of two ways. The ‘inductive duty cycle’ is the inductive coupling period relative to the discharge cycle period

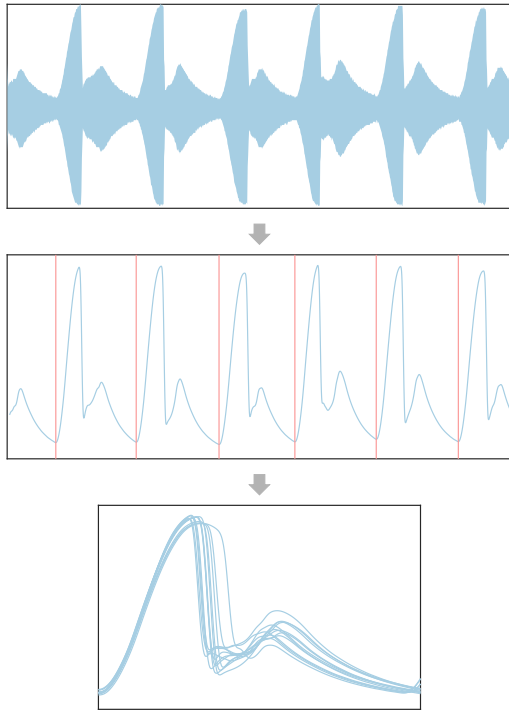
$$\tau_{\text{ind}}^* = \frac{\tau_{\text{ind}}}{\tau_{\text{cap}} + \tau_{\text{ind}}} \quad (3.3)$$

where τ_{cap} and τ_{ind} are the capacitive and inductive coupling periods respectively, as shown in figure 3.4 (b). The ‘inductive frequency shift’ is the difference between the two time-integrated antenna frequency curves, relative to the purely capacitive curve

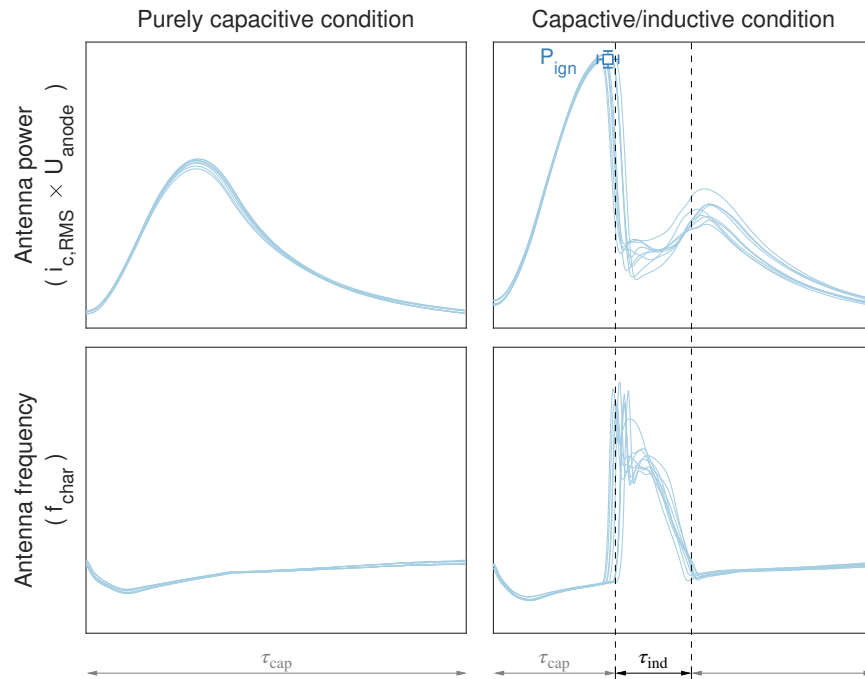
$$\Delta f_{\text{ind}}^* = \frac{[\int f_{\text{char}} dt]_{\text{cap/ind}} - [\int f_{\text{char}} dt]_{\text{pure cap}}}{[\int f_{\text{char}} dt]_{\text{pure cap}}} \quad (3.4)$$

Both measures of inductive coupling are presented and compared in this work. They are calculated for each discharge cycle and presented as the mean and standard deviation of all cycles in a particular measurement.

3 Power efficiency estimation



(a) Method used to collate the discharge cycles. Starting with the raw signal, a moving-window RMS is calculated and the cycles are identified by minima; finally the individual cycles are collated.



(b) Identification of transient capacitive-inductive transition from antenna current measurements. Using the collated cycles, periods of inductive coupling are identified by a sharp decrease in antenna power and a simultaneous sharp increase in antenna frequency, relative to a reference purely capacitive condition.

Figure 3.4: Processing of antenna current measurements.

Additionally, the ‘ignition power’ P_{ign} , shown with error bars in the upper-right quadrant of figure 3.4 (b), can be defined as the maximum antenna power occurring before a capacitive-to-inductive mode transition, where the antenna power is defined as the product of the root-mean-square antenna current and the anode potential. The anode potential is used as a substitute for antenna potential since they are of the same order (Herdrich & Petkow, 2008) and the latter was not measured.

3.3 Results & discussion

In this study, results from IPG7 experiments using a variety of propellants at various flowrates are presented and discussed. Those propellants include pure oxygen and pure carbon-dioxide, as well as their respective mixtures with argon, as described in table 3.1. For each propellant configuration, measurements were taken in a series of increasing anode powers until either the tube was at risk of fracturing under the thermal load (P_{tube} approaching 9 kW), there was a risk of exceeding the 180 kW anode power limit, or there was significant instability in the anode power. Tube pressure was not measured due to the intrusive nature of those measurements. Previous experimental work showed that the tube pressure increases with the flow rate and the anode power and, for the conditions presented here, it can be expected to range between 200 Pa and 1500 Pa. Initially, results from the antenna current measurements are presented and analysed in terms of the transient antenna current behaviour within each individual discharge cycle. Subsequently, calorimetry results are presented to quantify both the heat transfer through the tube wall and the enthalpy of the plasma jet. Together, both sets of results form a basis to help link the transient antenna current behaviour to the macroscopic plasma behaviour.

3.3.1 Antenna current

Presented in figure 3.5 are the instantaneous antenna powers at capacitive-inductive transition (P_{ign}) for various propellant configurations against normal volumetric flow rate (equivalent to particle flow rate). The datasets 02-105-00%a and 02-105-00%b represent two measurements of the same propellant configuration, and therefore can be used to assess the repeatability of the measurements. They are in relatively good agreement with the range of the former being completely contained within the range of latter. Considering this pair as a single data point, the ignition power increases monotonically with respect to flow rate for the O_2 configurations. This is a predictable result since a simple conservation of mass analysis shows that an increasing flow rate must decrease the average particle residence time in the tube. The Ar- O_2 configurations appear to fit into the same trend as the O_2 configurations, meaning that the substitution

3 Power efficiency estimation

Table 3.1: Overview of experimental conditions organised by propellant configuration. A number of conditions were tested for each configuration over increasing anode powers. Each configuration has a unique identifier that follows the format of ‘(non-argon species)-(volumetric flow rate)-(argon component by volume)’. Volumetric flow rates were measured at the gas inlets in units of normal litres per minute. The particle and mass flow rates were calculated from the ideal gas law, therefore volumetric and molar fractions are equivalent.

Propellant configuration				Non-argon			Argon		Range of conditions tested		
Identifier	\dot{V} L/min	\dot{n} mol/s	\dot{m} g/s	Species	x %	w %	x %	w %	N	P_{anode} kW	P_{tank} Pa
○ 02-076-00%	76	0.0519	1.66	O ₂	100	100	–	–	9	0.9 → 96.4	19.7 → 20.5
□ 02-105-00%a	105	0.0714	2.28	O ₂	100	100	–	–	5	1.0 → 51.2	25.6 → 26.5
◇ 02-105-00%b	105	0.0715	2.29	O ₂	100	100	–	–	8	1.0 → 105.8	25.4 → 27.0
☆ 02-142-00%	142	0.0967	3.10	O ₂	100	100	–	–	8	0.9 → 88.5	32.7 → 34.3
△ 02-128-58%	128	0.0873	3.20	O ₂	42	36	58	64	8	0.9 → 113.3	23.9 → 25.8
▽ 02-134-68%	134	0.0916	3.43	O ₂	32	27	68	73	9	0.9 → 122.0	24.2 → 26.3
● C02-080-00%	80	0.0546	2.40	CO ₂	100	100	–	–	7	1.0 → 56.3	28.4 → 31.0
■ C02-102-00%	102	0.0698	3.07	CO ₂	100	100	–	–	7	0.9 → 50.3	37.8 → 40.6
▲ C02-123-74%	123	0.0835	3.42	CO ₂	26	28	74	72	11	1.0 → 136.4	23.3 → 28.0
▼ C02-130-69%	130	0.0888	3.66	CO ₂	31	33	69	67	11	0.9 → 154.5	26.9 → 32.4

of 58% or 68% of O₂ with Ar does not significantly affect the ignition power. Therefore, the behaviour of oxygen and argon in terms of ignition power appears to be similar. The two Ar-O₂ configurations have approximately the same ignition power, despite 02-128-58% having a lower flow rate and 02-134-68% having a higher argon fraction. Given the low uncertainty for both data points, this suggests that the differences in flow rate and argon fraction have approximately equal and opposite influences on the ignition power.

The two CO₂ data points, like the O₂ points, increase with respect to flow rate. Comparing the CO₂ points with the adjacent (in terms of flow rate) O₂ points, CO₂ requires more power to ignite, and the trend is steeper. The addition of Ar to CO₂ causes the ignition power to drop dramatically, even if the total flow rate increases. C02-102-00% ignites at 6.2 MW while C02-123-74% ignites at only 1.9 MW: a 3 times reduction of ignition power by replacing 74 % CO₂ with Ar, even as total flow rate increases by 21 L/min. Comparing the two Ar-CO₂ configurations, C02-130-69% has a higher flow rate and a lower argon fraction than C02-123-74%, and both differences contribute to a higher ignition power.

For the pure propellants, CO₂ requires more power to ignite than O₂, yet for the

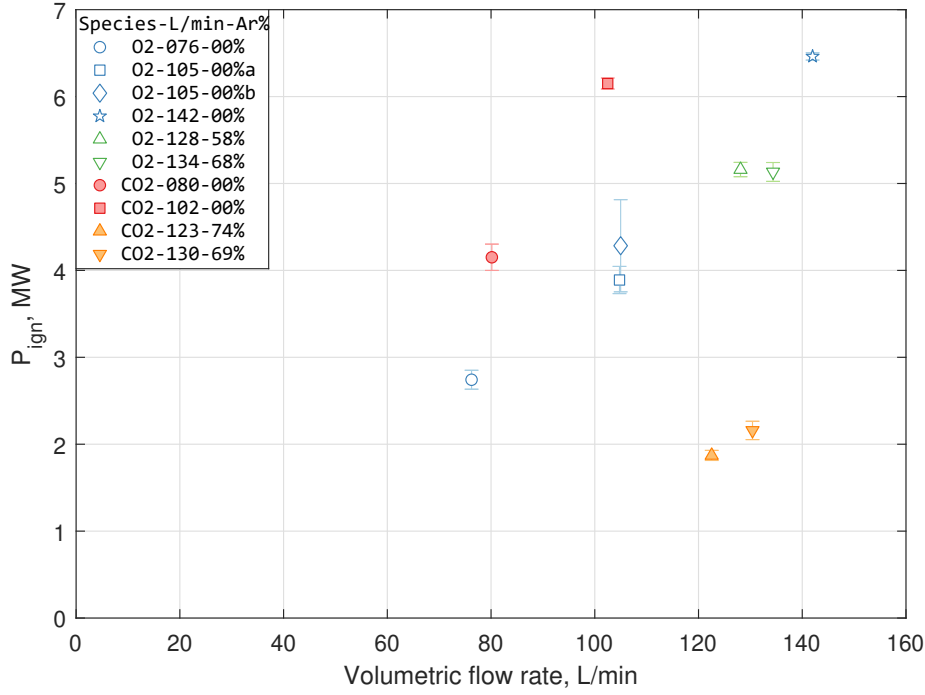


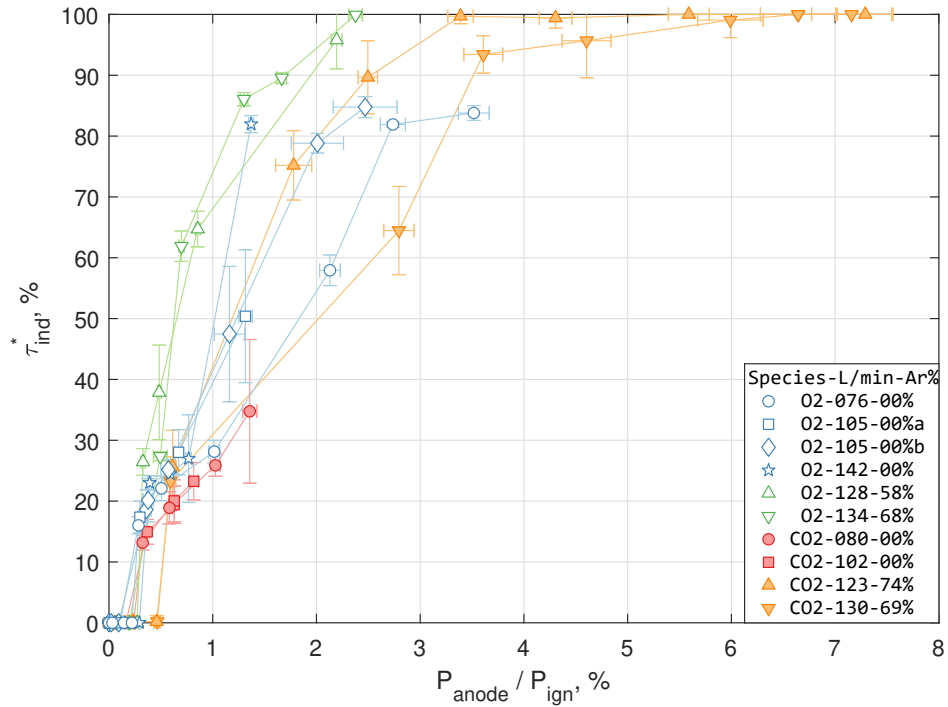
Figure 3.5: Antenna power causing capacitive–inductive transition (ignition) for various propellant configurations.

mixtures, Ar-O₂ requires more power than Ar-CO₂. Therefore, the addition of Ar has a significantly stronger effect for CO₂ than for the O₂, which can only be explained by the occurrence of a different interaction between the two species. The decrease of ignition power with increasing Ar fraction is expected, since Ar is monatomic and therefore imparted energy goes only to ionisation and excitation, while for the molecular gases there are the additional energy sinks including dissociation, vibration and rotation.

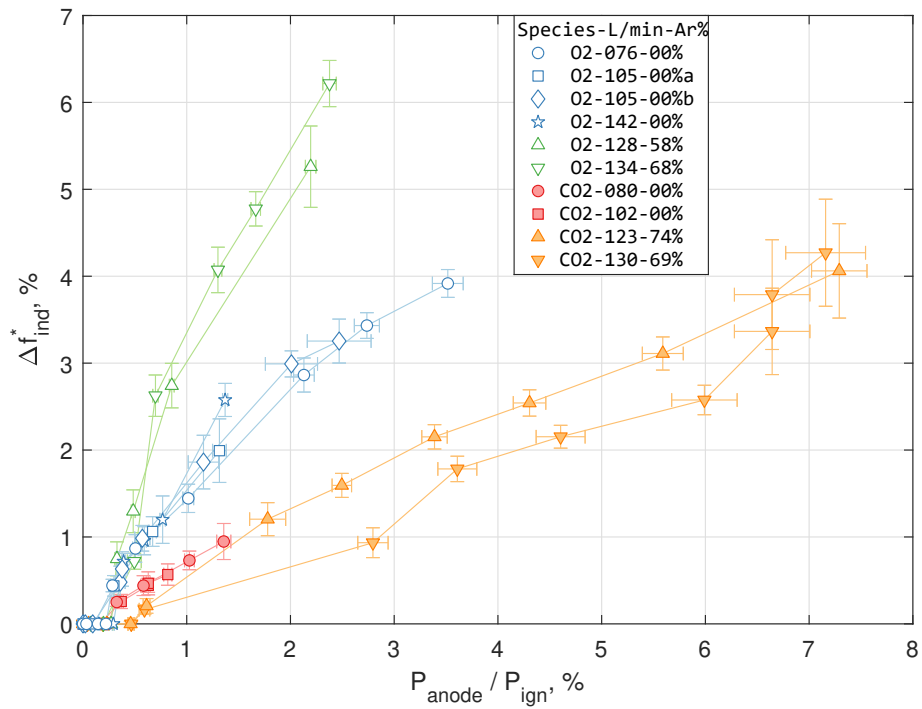
In figure 3.6, two proposed measures of inductive coupling are presented for increasing anode power, the ‘inductive duty cycle’ τ_{ind}^* (a) and the ‘inductive frequency shift’ Δf_{ind}^* (b), as defined by equations (3.3) and (3.4) respectively. The anode power is normalised by the ignition power to account for the behaviour seen in figure 3.5. Remembering that P_{anode} is the time-averaged power applied to the circuit and P_{ign} is the maximum instantaneous power applied to the coil, P_{anode}/P_{ign} has a value in the range of 0 % to 8 %. For each propellant configuration, there are several initial data points for which $\tau_{ind}^* = \Delta f_{ind}^* = 0$, indicating purely capacitive coupling. Therefore, the first non-zero data point for each configuration represents the lowest anode power that triggers inductive ignition.

Considering the first non-zero points in figure 3.6(a), there is a discrete jump from $\tau_{ind}^* = 0\%$ to $\sim 20\%$, indicating a discrete jump as inductive coupling is established. The size of this jump appears to grow as the flow rate increases. Each propellant configuration trends upward, although somewhat erratically. The CO₂ datasets end early

3 Power efficiency estimation



(a) Inductive duty cycle.



(b) Inductive frequency shift.

Figure 3.6: Measures of inductive coupling for various propellant configurations.

due to high heating through the tube wall (shown later) and the associated high risk of fracture. For O_2 , 02-076-00% and 02-105-00% appear to be flattening at $\tau_{ind}^* = 85\%$. The addition of argon causes steeper trends compared to the respective pure propellants. CO_2 's inability to achieve high inductive coupling is resolved with the inclusion of Ar, which together produce the highest inductive coupling of any configuration presented here. In particular, C02-123-74% reaches $\tau_{ind}^* = 100\%$ at 3.4 % power ratio and maintains that value up to 7.3 % power ratio. This highlights an issue with using τ_{ind}^* as a measure of inductive coupling in that it cannot be used to demarcate between different continuously inductive conditions. An additional issue is the relatively large error bars for some conditions which indicate a high level of variation between sequential discharge cycles.

Comparing figure 3.6(b) with(a) reveals that the inductive frequency shift produces much more consistent and linear trends for each propellant type. The trends of each propellant type are now separated and can be put in order of increasing Δf_{ind}^* for a particular value of P_{anode}/P_{ign} : Ar- CO_2 , CO_2 , O_2 then Ar- O_2 . Here the increasing inductive coupling of Ar- CO_2 can be observed past the point where $\tau_{ind}^* = 100\%$, however, it is actually Ar- O_2 that achieves the highest Δf_{ind}^* , even at a significantly lower relative power. Repeating the same argument of dissociation and ionisation energies, the expected ordering is CO_2 , Ar- CO_2 , O_2 then Ar- O_2 , yet experimentally Ar- CO_2 has equivalent or lower values of Δf_{ind}^* compared to CO_2 . For Ar- CO_2 the inductive mode is easy to ignite but difficult to increase past initial levels. Qualitatively, lower values of Δf_{ind}^* for the same τ_{ind}^* indicate a shallower profile of f_{char} or a weaker inductive coupling, while higher values indicate a steeper profile or a stronger inductive coupling. Consequently, Ar- O_2 has a much stronger inductive coupling than Ar- CO_2 for the same τ_{ind}^* or for the same P_{anode}/P_{ign} .

3.3.2 Calorimetry

Figure 3.8 contains calorimetric measurements of P_{tube} and P_{jet} . The jet power is comprised of energy deposited into the plasma, while the tube power is comprised of deposited energy that is transferred through the tube wall, and resistive heating from the antenna. While values for P_{tube} were obtained for all datasets, time constraints did not permit P_{jet} to be captured for all gas configurations. In figure 3.8 (a) the tube power is plotted against anode power. Each configuration shows a smooth, monotonically increasing trend with the exception of 02-105-00%, 02-142-00%, 02-128-58% and 02-134-68%. For each of these, there is a critical point where the slope of the line decreases significantly, either becoming negative or in one case flattening. This behaviour has been consistently observed in literature and is linked to an additional operating mode occurring after the capacitive and inductive modes (Herdrich & Petkow, 2008; Chadwick et al., 2016). For convenience, we refer to this condition as 'mode 3'.

3 Power efficiency estimation

This mode was not observed for CO₂ nor Ar-CO₂, however, for O₂ and Ar-O₂, the anode power of the critical point decreases as the flow rate increases and also as the Ar fraction increases. This behaviour has important implications for propulsion since the tube power is wasted power. In fact, it is worse than that, since additional resources must be spent to remove this wasted power so that the tube does not fracture (and in a practical system, to prevent overheating of the spacecraft). Therefore, this operating condition with comparatively very low tube power is highly useful.

Figure 3.8 (b) presents the sum of tube and jet calorimetric powers for each configuration against anode power. A roughly proportional relationship is seen, which can be explained by considering that both the anode power and the sum of tube and jet powers should be roughly proportional to the lumped resistance of the equivalent circuit. The electrical efficiency, defined earlier as $\eta_{elec} = (P_{tube} + P_{jet})/P_{anode}$, represents the portion of input electrical power that is deposited into the tube and the plasma. Fitting a proportional relationship yields $\eta_{elec} = 18 \%$. This low efficiency reflects the experimental nature of the facility and could certainly be improved with an optimised design containing a matching network. As previously noted, the triode alone dissipates some 25 % of the anode power.

Figure 3.8 (c) shows the thermal efficiency, defined earlier as $\eta_{therm} = P_{jet}/(P_{tube} + P_{jet})$, noting that this neglects other thermal losses, for example, through the tank lid or the injector head. The thermal efficiency represents the useful plume enthalpy as a portion of the total thermal power produced (assuming the mentioned neglected losses are insignificant). Each configuration starts with a high thermal efficiency, in the order of 82 %, since each starts with purely capacitive coupling that tends to deposit energy into the centre of the plume. Although this is a relatively efficient use of power, it is worth remembering that the flow rate is held constant for each configuration, and therefore this is a very inefficient use of propellant, and an undesirable operating point. As the anode power increases, the losses increase and the thermal efficiency decreases. The CO₂ case plateaus at approximately 40 % and remains there even as anode power increases. Cases 02-142-00%, 02-128-58% and 02-134-68% exhibit a reversal of their trends such that the final thermal efficiencies are approximately 84 %. These conditions match ‘mode 3’ conditions observed in figure 3.8 (a). Cases 02-128-58% and 02-134-68% show that, after the 84 % relative jet power is achieved, there is a range of anode powers which produce the same figure or better, or in other words, this highly efficient ‘mode 3’ is accessible for a range of throttle positions.

Figure 3.8 (d) shows the thermal efficiency plotted against inductive frequency shift. Once again the purely capacitive conditions are confined to the axis and the first non-zero point for each configuration represents the first condition with inductive coupling. With this, it is easier to see the range of initial inductive conditions, that being thermal efficiency between 34 % and 47 %. Considering those 3 configurations which exhibit ‘mode 3’, they each have approximately 50 % thermal efficiency at $\Delta f_{ind}^* = 1.2 \%$ and

84 % thermal efficiency at $\Delta f_{\text{ind}}^* = 2.6$ %. Oxygen as a propellant is significantly more abundant in the space environment than argon, however, it requires higher flow rate and/or P_{anode} to achieve ‘mode 3’. Therefore, supplementing space-collected oxygen with argon from Earth could be considered to expand the range of desirable ‘mode 3’ operating conditions for an oxygen-based system.

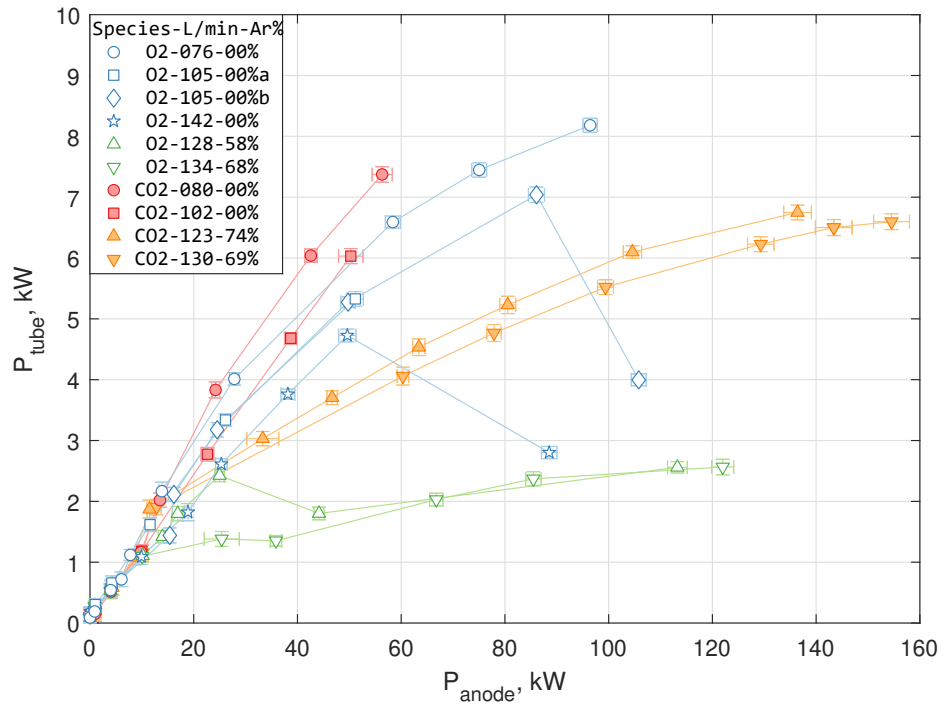
The inductive frequency shift Δf_{ind}^* appears to be a good predictor for ‘mode 3’, and is itself a function of the electrical and geometric parameters of the plasma current, as discussed earlier. The large discrete shift of Δf_{ind}^* coinciding with the onset of ‘mode 3’ could be explained by a large shift inward of the plasma current radius. Previous work has identified conditions where IPG7 exhibits inductive coupling simultaneously with a significant central distribution of light emission; a possible explanation is inductive and alpha-capacitive coupling occurring in parallel, with the latter being responsible for the central deposition of power (Georg et al., 2020 (chapter 2)). Modelling of the equivalent circuit may reveal more about the relationship between the characteristic frequency and plasma current, and whether the inductive frequency shift can be wholly or partially accounted for by a radial contraction of the plasma current.

The results for each propellant configuration at the maximum anode power achieved under each regime are summarised in table 3.2. The table contains data reproduced from a publication by Chadwick et al. (2020), where they studied the propulsive characteristics of several propellant configurations in IPG7 including baffle plate measurements of thrust. Equivalent conditions from that study are identified and compared by matching both the propellant configuration and the anode power. Exhaust velocity is calculated as $v_e = F/\dot{m}$ and added thrust efficiency as $\eta_{\Delta F} = (F - F_{\text{cold}})^2 / (2 \dot{m} P_{\text{anode}})$, where F is thrust. For conditions where both sets of results are complete, the nozzle efficiency is calculated as $\eta_{\text{nozzle}} = \eta_{\Delta F} / (\eta_{\text{elec}} \times \eta_{\text{therm}})$.

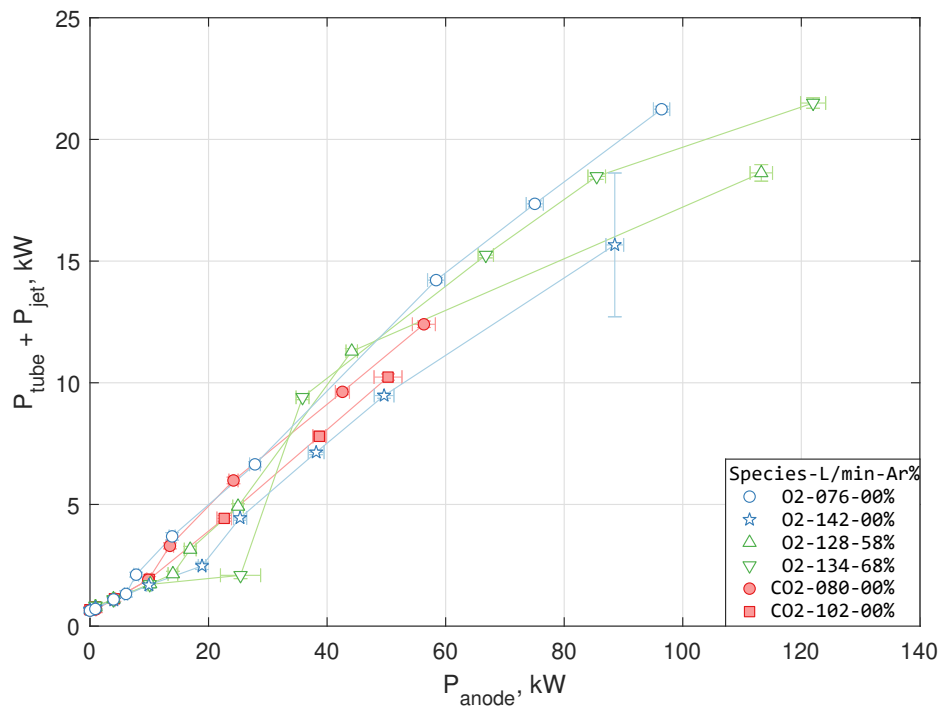
From table 3.2, it is clear that the electrical efficiency is fairly consistent across the different propellant configurations and regimes, approximately 18 %, with the exception of the inductive condition for 02-134-68%, which has $\eta_{\text{elec}} = 8$ %. The uncertainty for P_{anode} (shown in figure 3.8) for that condition is relatively high compared to other data points. A possible explanation for both could be a poor impedance matching and therefore a higher portion of reflected power; in any case this condition should be considered as an outlier. For each propellant configuration the thermal efficiency increases in order of capacitive, inductive and ‘mode 3’, with the exception of the 02-134-68% outlier condition just mentioned.

The measured thrusts consist of a component due to the pressure gradient between the injector head and the vacuum facility, and a component due to the gas-dynamic expansion of the discharge. The former is constant with increasing anode power ($F_{\text{cold}} \approx 1$ N) while the latter increases monotonically with anode power for the same propellant configuration. An ideal operating point would have a high v_e , representing effective use of propellant mass, and a high $\eta_{\Delta F}$, representing effective use of input power. There-

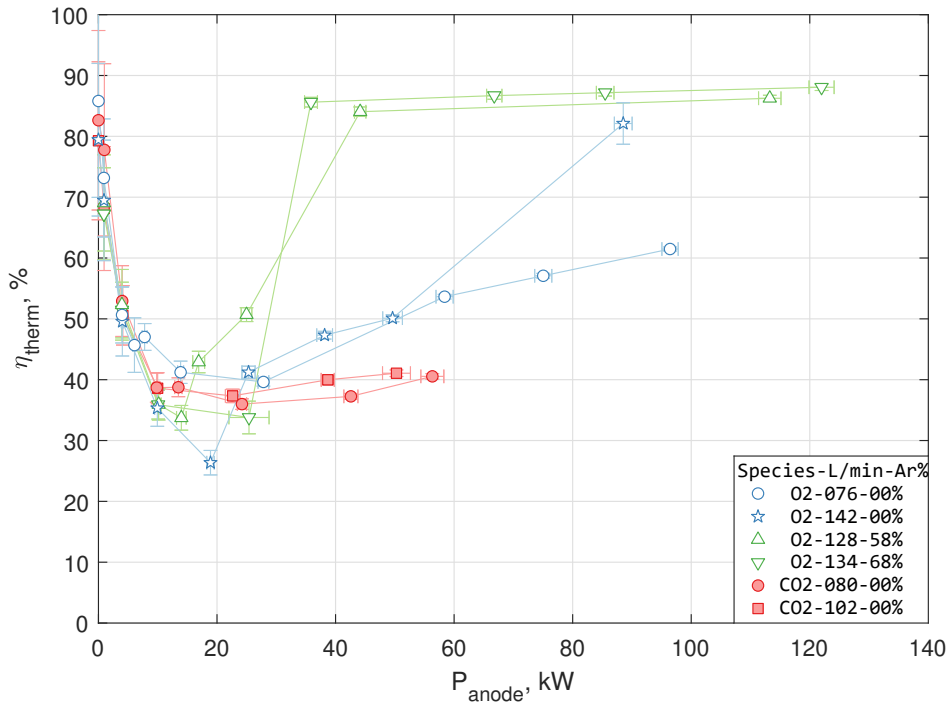
3 Power efficiency estimation



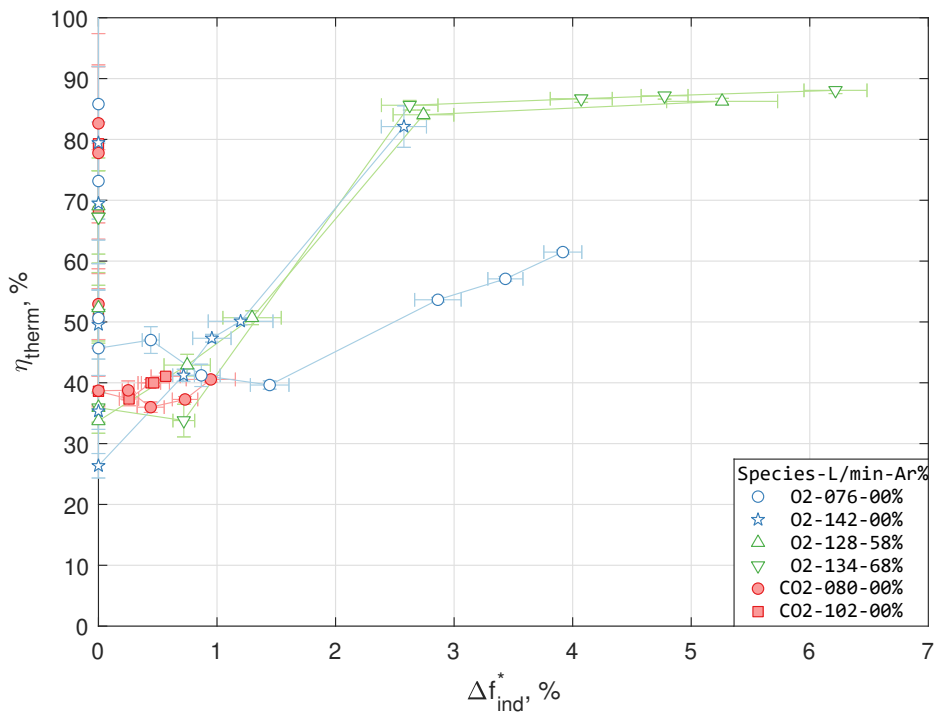
(a) Tube power.



(b) Sum of tube and jet powers.



(c) Thermal efficiency.



(d) Thermal efficiency against inductive frequency shift.

Figure 3.8: Tube and jet calorimetric powers. Jet power is not available for some conditions.

3 Power efficiency estimation

fore, the best operating points are the 02-128-58% and 02-134-68% ‘mode 3’ conditions, and the C02-123-74% inductive condition. These three conditions also have high values of Δf_{ind}^* . It must be conceded, however, that $\eta_{\Delta F}$ in the order of 4 % is quite low. This is a result of the poor electrical efficiencies ($\sim 18\%$) and the poor nozzle efficiencies ($\sim 25\%$). The latter can be seen as an encouraging aspect because, with the addition of a properly designed nozzle, it should be possible to recover much of the $\sim 75\%$ wasted thermal power, increasing thrust, exhaust velocity and thrust efficiency. Furthermore, the poor electrical efficiency can be largely attributed to the experimental nature of the power supply system. The power supply design was chosen to maximise flexibility and serviceability, at the expense of electrical efficiency. In the present work, desirable ‘mode 3’ conditions and respective inputs have been identified, which constrains the requirements for an optimised power supply. An optimised power supply design based on solid-state electronics and informed by the present work is expected to significantly improve the electrical efficiency. Importantly, the thermal efficiency (the efficiency that relates to propellant configuration) is high for high flow rate oxygen and argon-oxygen.

Finally, it is worth noting that with more experimental data points, it would be possible to empirically determine Δf_{ind}^* as a function of the propellant configuration and P_{anode} . This is particularly so, since figure 3.5 shows that P_{ign} is well defined by the propellant flow rate and Ar fraction, and figure 3.6 (b) shows that Δf_{ind}^* is well defined by $P_{\text{anode}}/P_{\text{ign}}$. Therefore, the correlation between Δf_{ind}^* and P_{anode} would allow an operator to accurately control the level of inductive coupling (Δf_{ind}^*) by adjusting P_{anode} . For example, it would allow the operator to control Δf_{ind}^* such that the highly efficient ‘mode 3’ is achieved. Additionally, this knowledge can be used in the design of a practical system to ensure that the power supply matches but does not exceed the output necessary to achieve the range of inductive coupling and the range of operating points that are desired for the particular application.

3.4 Conclusion

This paper presented experimental measurements of a high-power inductive plasma generator fed by oxygen, carbon-dioxide, and respective mixtures with argon at various flow rates and mixture ratios. Measurements of the transient coil current were analysed to identify the conditions at which capacitive-inductive transition occurs and the degree of subsequent inductive coupling that does occur. The relevant technique was developed as an extension of the technique introduced by Chadwick (2017). Consequently, the qualitative assessment of inductive coupling degree has been developed into a quantitative assessment. Additionally, the technique has been demonstrated over a range of propellant configurations and input powers.

Table 3.2: Summary of results. For each propellant configuration, results are presented corresponding to the maximum anode power achieved under capacitive, inductive and ‘mode 3’ regimes respectively. Each configuration is labelled in the format of ‘(non-argon species)-(volumetric flow rate)-(argon component by volume)’. Power efficiencies are not available for those configurations for which jet power was not measured. Thrust data at equivalent conditions are shown where available based on the battle plate measurements of Chadwick et al. (2020). †Denotes an outlier condition, as explained in text.

Results from this work							Thrust data at equivalent conditions					
Propellant configuration	Regime	$P_{\text{anode, max}}$ kW	τ_{ind}^* %	Δf_{ind}^* %	η_{elec} %	η_{therm} %	Propellant configuration	P_{anode} kW	F N	v_e m/s	$\eta_{\Delta F}$ %	η_{nozzle} %
○ 02-076-00%	Cap.	6	0	0.0	22	46	–	–	–	–	–	–
	Ind.	96	84	3.9	22	61	–	–	–	–	–	–
◇ 02-105-00% ^b	Cap.	4	0	0.0	–	–	02-105-00%	4	1.20	482	0.0	–
	Ind.	106	85	3.3	–	–		100	4.86	1946	2.8	–
☆ 02-142-00%	Cap.	19	0	0.0	13	26	–	–	–	–	–	–
	Ind.	50	27	1.2	19	50		–	–	–	–	–
	Mode 3	89	82	2.6	18	82		–	–	–	–	–
△ 02-128-58%	Cap.	14	0	0.0	15	34	02-128-59%	10	1.75	503	0.1	1
	Ind.	25	38	1.3	20	51		35	4.00	1148	2.5	25
	Mode 3	113	96	5.3	16	86		119	7.17	2055	3.8	27
▽ 02-134-68%	Cap.	10	0	0.0	17	36	02-133-68%	4	1.48	400	0.0	0
	Ind. [†]	25 [†]	27 [†]	0.7 [†]	8 [†]	34 [†]		36	4.12	1116	2.8	100 [†]
	Mode 3	122	100	6.2	18	88		123	7.27	1969	3.8	24
● 02-080-00%	Cap.	10	0	0.0	19	39	02-080-00%	10	1.40	531	0.4	5
	Ind.	56	35	0.9	22	41		56	2.49	944	0.8	9
■ 02-102-00%	Cap.	10	0	0.0	19	39	–	–	–	–	–	–
	Ind.	50	23	0.6	20	41		–	–	–	–	–
▲ 02-123-74%	Cap.	9	0	0.0	–	–	02-122-74%	4	1.56	477	0.0	–
	Ind.	136	100	4.1	–	–		101	6.73	2051	4.1	–
▼ 02-130-69%	Cap.	10	0	0.0	–	–	–	–	–	–	–	–
	Ind.	155	100	4.3	–	–		–	–	–	–	–

3 Power efficiency estimation

Calorimetric measurements were presented, exhibiting a third, highly efficient mode that occurs at some high-power conditions for oxygen and argon-oxygen propellants. In this ‘mode 3’, $\sim 84\%$ of the thermal power produced by the coil exits the discharge chamber as plasma jet enthalpy. This thermal power efficiency remains stable as anode (input) power increases, meaning that the high efficiency of ‘mode 3’ can be accessed over a range of operating conditions. Using carbon-dioxide as a propellant resulted in low input powers due to its tendency to deposit heat into the tube wall, risking fracture. The addition of argon, however, significantly reduces the instantaneous ignition power and reduces the power lost to the tube cooling system.

The occurrence of ‘mode 3’ can be understood in terms of the frequency shift observed in the coil current caused by the changing effective inductance of the coil/plasma system, itself a function of the electrical and geometric properties of the plasma current. This phenomenon is consistent with a radial contraction of the plasma current, although further work is needed to assess this hypothesis. Nonetheless, a basis is provided for understanding the ‘mode 3’ operating points, as is an approach for determining the optimal power supply sizing. With the efficiency of the coil/plasma system established, the nozzle and the unoptimised laboratory power supply are the main sources of inefficiency remaining. The nozzle efficiency peaks at 25% , which indicates a significant opportunity to increase thrust, exhaust velocity and thrust efficiency through a suitable nozzle design. An optimised design based on principles explored here could yield an efficient, high-power propulsion system that can use oxygen harvested from the space environment, perhaps augmented with a small supply of argon from Earth to extend the range of ‘mode 3’ operating points.

Acknowledgements

The authors would like to thank the German Research Foundation for their financial contributions to the experimental campaign under Project HE 4563/3-1.

This research is supported by an Australian Government Research Training Program (RTP) Scholarship.

Research undertaken for this report has been assisted with a grant from the Sir Ross and Sir Keith Smith Fund (Smith Fund) (www.smithfund.org.au). The support is acknowledged and greatly appreciated. The Smith Fund, by providing funding for this project, does not verify the accuracy of any findings or any representations contained in it. Any reliance on the findings in any written report or information provided to you should be based solely on your own assessment and conclusions. The Smith Fund does not accept any responsibility or liability from any person, company or entity that may have relied on any written report or representations contained in this report if that person, company or entity suffers any loss (financial or otherwise) as a result.

References

- Anih, S., Pagan, A. S., Koch, H., Martinez, P., Laufer, R., & Herdrich, G. (2019). Waste for Energy and Volume Recovery (WEVR) using Inductively Heated Plasma Generator Samuel. *70th International Astronautical Congress, IAC-19-B3*, 7, 8, x54017.
- Auweter-Kurtz, M., & Wegmann, T. (1999). Overview of IRS plasma wind tunnel facilities. *RTO AVT Course on "Measurement Techniques for High Enthalpy and Plasma Flows"*.
- Bathgate, S. N., Bilek, M. M., & McKenzie, D. R. (2017). Electrodeless plasma thrusters for spacecraft: A review. *Plasma Science and Technology*, 19(8). <https://doi.org/10.1088/2058-6272/aa71fe>
- Böhrk, H., & Auweter-Kurtz, M. (2006). Preliminary Results of TIHTUS Operation. *42nd AIAA/ASME/SAE/ASEE Joint Propulsion Conference & Exhibit*, AIAA 2006-5158. <https://doi.org/10.2514/6.2006-5158>
- Brown, N. P., & Walker, M. L. (2020). Review of plasma-induced hall thruster erosion. *Applied Sciences (Switzerland)*, 10(11). <https://doi.org/10.3390/app10113775>
- Chadwick, A. R. (2017). *Performance of Alternative Propellants in an Inductive Electric Propulsion System* (Ph.D. Thesis). The University of Adelaide. <http://hdl.handle.net/2440/119192>
- Chadwick, A. R., Dally, B. B., Herdrich, G., & Kim, M. (2020). High-power inductive electric propulsion operation with alternative propellants. *The Aeronautical Journal*, 124(1272), 151–169. <https://doi.org/10.1017/aer.2019.141>

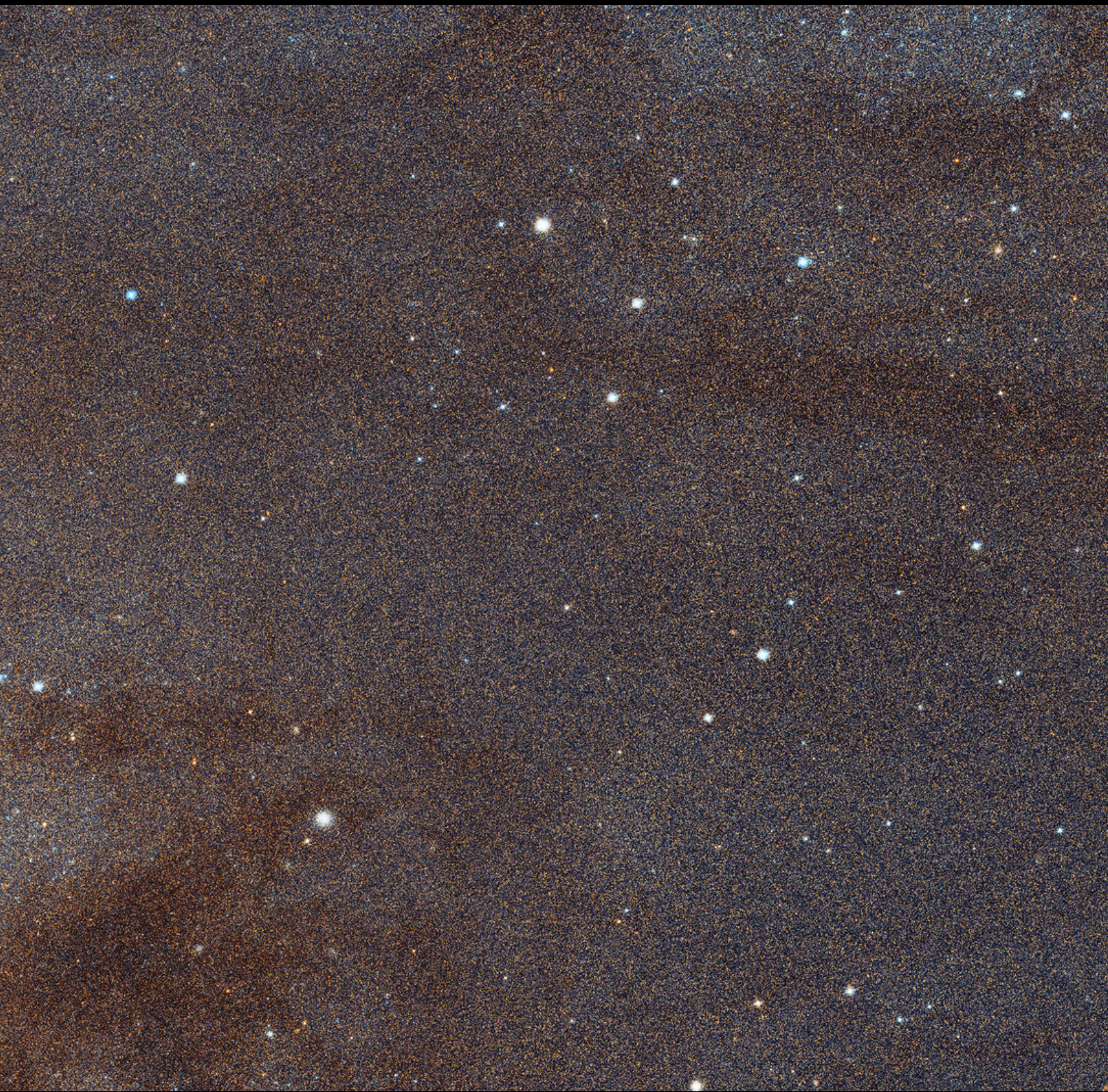
3 Power efficiency estimation

- Chadwick, A. R., Herdrich, G., Kim, M., & Dally, B. B. (2016). Transient electromagnetic behaviour in inductive oxygen and argon-oxygen plasmas. *Plasma Sources Science and Technology*, 25(6). <https://doi.org/10.1088/0963-0252/25/6/065025>
- Charles, C., Boswell, R. W., Laine, R., & MacLellan, P. (2008). An experimental investigation of alternative propellants for the helicon double layer thruster. *Journal of Physics D: Applied Physics*, 41(17). <https://doi.org/10.1088/0022-3727/41/17/175213>
- Cunge, G., Crowley, B., Vender, D., & Turner, M. M. (1999). Characterization of the E to H transition in a pulsed inductively coupled plasma discharge with internal coil geometry: bi-stability and hysteresis. *Plasma Sources Science and Technology*, 8(4), 576–586. <https://doi.org/10.1088/0963-0252/8/4/309>
- Georg, R., Chadwick, A. R., Dally, B. B., & Herdrich, G. (2020). Resolving transient discharge cycle behaviour in modulated inductive plasmas. *Vacuum*. <https://doi.org/10.1016/j.vacuum.2020.109636>
- Gudmundsson, J. T., & Lieberman, M. A. (1997). Magnetic induction and plasma impedance in a cylindrical inductive discharge. *Plasma Sources Science and Technology*, 6(4), 540–550. <https://doi.org/10.1088/0963-0252/6/4/012>
- Herdrich, G. (2004). *Construction, qualification and characterisation of an inductively heated plasma wind-tunnel system to simulate atmospheric entry (Aufbau, Qualifikation und Charakterisierung einer induktiv beheizten Plasmawindkanalanlage zur Simulation atmosphärischer)* (Ph.D. Thesis). Universität Stuttgart.
- Herdrich, G., Bauder, U., Boxberger, A., Gabrielli, R. A., Lau, M., Petkow, D., Pfeiffer, M., Syring, C., & Fasoulas, S. (2013). Advanced plasma (propulsion) concepts at IRS. *Vacuum*, 88(1), 36–41. <https://doi.org/10.1016/j.vacuum.2012.02.032>
- Herdrich, G., Chadwick, A. R., Dally, B. B., & Kim, M. (2015). Further Development of the TIHTUS Test Facility at IRS. *Joint Conference of 30th International Symposium on Space Technology and Science, 34th International Electric Propulsion Conference and 6th Nano-satellite Symposium, IEPC–2015–90252/ISTS–2015–b–90252*. http://electricrocket.org/IEPC/IEPC-2015-389%7B%5C_%7DISTS-2015-b-389.pdf
- Herdrich, G., & Petkow, D. (2008). High-enthalpy, water-cooled and thin-walled ICP sources characterization and MHD optimization. *Journal of Plasma Physics*, 74(3), 391–429. <https://doi.org/10.1017/S0022377807006927>
- Humble, R. W., Henry, G. N., & Larson, W. J. (1995). *Space propulsion analysis and design* (1st ed.). McGraw-Hill.
- Isayama, S., Shinohara, S., & Hada, T. (2018). Review of helicon high-density plasma: Production mechanism and plasma/wave characteristics. *Plasma and Fusion Research*, 13, 1–27. <https://doi.org/10.1585/PFR.13.1101014>

- Kaganovich, I. D., Smolyakov, A., Raitses, Y., Ahedo, E., Mikellides, I. G., Jorns, B., Taccogna, F., Gueroult, R., Tsikata, S., Bourdon, A., Boeuf, J.-P., Keidar, M., Powis, A. T., Merino, M., Cappelli, M., Hara, K., Carlsson, J. A., Fisch, N. J., Chabert, P., ... Fruchtman, A. (2020). Perspectives on Physics of ExB Discharges Relevant to Plasma Propulsion and Similar Technologies.
- Karrer, N., Hofer-Noser, P., Herdrich, G., & Auweter-Kurtz, M. (2003). Isolated current probe for continuous monitoring of AC currents of high amplitude and high frequency. *European Power Electronics Conference*.
- Karrer, N., Hofer-Noser, P., & Henrard, D. (1999). HOKA: a new isolated current measuring principle and its features. *Conference Record of the 1999 IEEE Industry Applications Conference. Thirty-Forth IAS Annual Meeting (Cat. No.99CH36370)*, 3, 2121–2128. <https://doi.org/10.1109/IAS.1999.806028>
- Kralkina, E. A., Nekliudova, P. A., Pavlov, V. B., Petrov, A. K., & Vavilin, K. V. (2017). Features of RF low-pressure discharge with inductive and capacitive channels. *Plasma Sources Science and Technology*, 26(5), 055006. <https://doi.org/10.1088/1361-6595/aa61e6>
- Kralkina, E. A., Nekliudova, P., Pavlov, V., Vavilin, K., Zadiriev, I., & Zhao, C. (2020). Experimental study of a low-pressure hybrid RF discharge. *Plasma Science and Technology*, 22(5), 055405. <https://doi.org/10.1088/2058-6272/ab69bd>
- Levchenko, I., Xu, S., Mazouffre, S., Lev, D., Pedrini, D., Goebel, D., Garrigues, L., Taccogna, F., & Bazaka, K. (2020). Perspectives, frontiers, and new horizons for plasma-based space electric propulsion. *Physics of Plasmas*, 27(2). <https://doi.org/10.1063/1.5109141>
- Manente, M., Trezzolani, F., Magarotto, M., Fantino, E., Selmo, A., Bellomo, N., Tesson, E., & Pavarin, D. (2019). REGULUS: A propulsion platform to boost small satellite missions. *Acta Astronautica*, 157(December 2018), 241–249. <https://doi.org/10.1016/j.actaastro.2018.12.022>
- Massuti-Ballester, B., Marynowski, T., & Herdrich, G. (2013). New Inductively Heated Plasma Source IPG7. *Frontier of Applied Plasma Technology*, 6(2).
- Merino, M., & Ahedo, E. (2016). Magnetic nozzles for space plasma thrusters. In J. Shohet (Ed.), *Encyclopedia of plasma technology vol 2* (pp. 1329–51). Taylor & Francis.
- Navarro-Cavallé, J., Wijnen, M., Fajardo, P., & Ahedo, E. (2018). Experimental characterization of a 1 kW Helicon Plasma Thruster. *Vacuum*, 149, 69–73. <https://doi.org/10.1016/j.vacuum.2017.11.036>
- Nishida, K., Mochizuki, S., Ohta, M., Yasumoto, M., Lettry, J., Mattei, S., & Hatayama, A. (2014). Equivalent circuit of radio frequency-plasma with the transformer model. *Review of Scientific Instruments*, 85(2), 4–7. <https://doi.org/10.1063/1.4832060>

3 Power efficiency estimation

- Piejak, R. B., Godyak, V. A., & Alexandrovich, B. M. (1992). A simple analysis of an inductive RF discharge. *Plasma Sources Science and Technology*, 1(3), 179–186. <https://doi.org/10.1088/0963-0252/1/3/006>
- Romano, F., Chan, Y.-A., Herdrich, G., Traub, C., Fasoulas, S., Roberts, P., Smith, K., Edmondson, S., Haigh, S., Crisp, N., Oiko, V., Worrall, S., Livadiotti, S., Huyton, C., Sinpetru, L., Straker, A., Becedas, J., Domínguez, R., González, D., ... Heißerer, B. (2020). RF Helicon-based Inductive Plasma Thruster (IPT) Design for an Atmosphere-Breathing Electric Propulsion system (ABEP). *Acta Astronautica*, 176(January), 476–483. <https://doi.org/10.1016/j.actaastro.2020.07.008>
- Romano, F., Massuti-Ballester, B., Binder, T., Herdrich, G., Fasoulas, S., & Schönherr, T. (2018). System analysis and test-bed for an atmosphere-breathing electric propulsion system using an inductive plasma thruster. *Acta Astronautica*, 147, 114–126. <https://doi.org/10.1016/j.actaastro.2018.03.031>
- Sou, H., Takao, Y., Noutsuka, T., Mori, Y., Uemura, K., & Nakashima, H. (2000). Study of plasma propulsion system with RF heating. *Vacuum*, 59(1), 73–79. [https://doi.org/10.1016/S0042-207X\(00\)00256-6](https://doi.org/10.1016/S0042-207X(00)00256-6)
- Takahashi, K. (2019). Helicon-type radiofrequency plasma thrusters and magnetic plasma nozzles. *Reviews of Modern Plasma Physics*, 3(1), 3. <https://doi.org/10.1007/s41614-019-0024-2>
- Tsifakis, D., Charles, C., & Boswell, R. (2020). An Inductively-Coupled Plasma Electrothermal Radiofrequency Thruster. *Frontiers in Physics*, 8(February), 1–10. <https://doi.org/10.3389/fphy.2020.00034>
- Turner, M. M., & Lieberman, M. A. (1999). Hysteresis and the E-to-H transition in radiofrequency inductive discharges. *Plasma Sources Science and Technology*, 8(2), 313–324. <https://doi.org/10.1088/0963-0252/8/2/312>
- Vitucci, J. J. (2019). *Development and test of a superconducting helicon plasma thruster* (Ph.D. Thesis). University of Maryland.



Circuit model

Model for estimating time-varying properties of an inductively coupled plasma

In the third article, a high-power plasma generator is modelled as an electrical circuit, such that the antenna-plasma coupled system is reduced to a complex impedance through the transformer model. The impedance can be estimated from experimental measurements of the antenna current. The real part is related to the current amplitude and the imaginary part is related to the current frequency. Power series of oxygen plasmas at two different flow rates are investigated and used to demonstrate the technique. Time-resolved plasma properties, including skin depth, plasma volume, electrical conductivity and plasma current, are calculated.

Statement of authorship

Title Model for estimating time-varying properties of an inductively coupled plasma

Publication Published: Georg, R., Chadwick, A. R., Dally, B. B., & Herdrich, G. (2022a). Model for Estimating Time-Varying Properties of an Inductively Coupled Plasma. *IEEE Transactions on Plasma Science*. <https://doi.org/10.1109/TPS.2022.3166162>

Principal author contribution

This paper reports on original research I conducted during the period of my Higher Degree by Research candidature and is not subject to any obligations or contractual agreements with a third party that would constrain its inclusion in this thesis. I am the primary author of this paper.

Principal author R. Georg

Contribution I contributed approximately 80 % to the authorship of this paper. Excluding the experimental component, I was primarily responsible for the conception of the paper. I drafted the manuscript including all tables and figures. I conducted the majority of the analysis. I acted as the corresponding author.

My contribution satisfies all authorship criteria of the *Australian Code for the Responsible Conduct of Research*.

_____ 8 July 2022

Co-author contributions

By signing the statement of authorship, each co-author certifies that: i. the candidate's stated contribution to the publication is accurate (as detailed above); ii. permission is granted for the candidate to include the publication in the thesis; and iii. the sum of all co-author contributions is equal to 100 % less the candidate's stated contribution.

Co-author A. R. Chadwick

Contribution Collected the experimental data that is analysed in the paper. Provided knowledge and assisted with analysis and revising the manuscript. Involved in the conception of the paper, particularly the experimental component.

_____ 8 July 2022

Co-author B. B. Dally

Contribution Provided knowledge and assisted with analysis and revising the manuscript.

_____ 8 July 2022

Co-author G. Herdrich

Contribution Provided knowledge and assisted with analysis and revising the manuscript. Involved in the conception of the paper, particularly the experimental component.

_____ 8 July 2022

Abstract

A developing application of inductively coupled plasmas is in the field of electrodeless (propellant-flexible) electric propulsion. A significant issue facing this application is the need for diagnostic techniques that do not disturb the plasma (are non-intrusive), are propellant-agnostic, can resolve time-variance and are suitable for use in-flight. A new technique meeting these criteria is presented in this work. The technique makes use of the transformer model of inductive coupling to estimate the plasma impedance from the antenna current and resonant frequency, both of which can be measured non-intrusively. Having an estimate of the plasma impedance, it is possible to estimate a variety of plasma properties under the assumption of a uniform tubular plasma volume. Starting with a circuit representation of a high-power inductive plasma source, governing equations are derived and a solution method is described. Experimental data from the plasma source showing transient behaviour (fluctuations within 300 Hz cycle) in oxygen plasmas with various input powers and flow rates are analysed to demonstrate the technique and investigate trends. The technique produces results that are self-consistent and align well with previous theoretical work.

4.1 Introduction

Inductively coupled plasmas have a wide range of established applications for industrial plasma processing. One potential application is in electric propulsion for space vehicles. In its simplest form, inductive heating is used to heat a propellant material which then expands through a nozzle to produce thrust. Additional, secondary thrust mechanisms are also possible, such as magnetic nozzles and $E \times B$ drift velocity. Compared to conventional electric propulsion techniques, the main advantage is the separation of electrical components from high-enthalpy propellant flow, hence reducing the impact of erosion and improving the operating life. A follow-on effect is that a wide range of propellant materials are possible, including, for example, oxygen, nitrogen, carbon-dioxide, iodine, water and syngases. Hence, this technique can be termed ‘electrodeless’ or ‘propellant-flexible’ electric propulsion. This propellant flexibility is needed for advanced applications such as the TIHTUS hybrid thruster (Böhrk & Auweter-Kurtz, 2006), in-situ resource utilisation (ISRU) and atmosphere-breathing electric propulsion (ABEP).

In its simplest form, a propulsion system using inductively coupled plasma consists of a tubular discharge chamber made of a dielectric material (e.g. quartz). Propellant material flows from inlets at one side of the chamber to the outlet. Positioned around the discharge chamber and therefore separated from the flow is a radiofrequency antenna, typically a helical coil, that inductively heats the propellant material and generates a

plasma. Including helicon plasmas as a special case of inductive plasma, there are several groups worldwide that are actively developing this technology for space propulsion (Romano et al., 2020; Sou et al., 2000; Herdrich et al., 2013; Isayama et al., 2018; Navarro-Cavallé et al., 2018; Vitucci, 2019; Magarotto & Pavarin, 2020; Takahashi, 2019; Tsifakis et al., 2020; Kralkina et al., 2020).

The need to measure and understand fundamental processes within the antenna–plasma system is a prominent problem within the field. For the specific application of electrodeless electric propulsion systems, it is desirable to develop techniques with the following attributes: *non-intrusive*—such that the operation of the system is not affected and erosion is limited; *real-time*—such that outputs could be used for monitoring and control; *high-sampling frequency*—to capture transient phenomena; and *propellant agnostic*—to maintain flexibility of propellant choice, including mixtures. Non-intrusive techniques used in literature include optical emission spectroscopy (OES) and laser-induced fluorescence (LIF). Both techniques are optical in nature, necessitating optical access to the discharge chamber, and the resulting measurements are integrated along the line-of-sight. In principle, real-time and high-sampling frequency requirements could be met with these techniques. High-sampling frequencies have been demonstrated for OES in literature (so-called phase-resolved OES or “PROES”). A common challenge for both techniques is tolerating different propellants and mixtures, since both rely on identifying characteristic atomic spectra, which is confounded by the presence of multiple species. The limitations of extant non-intrusive techniques when used with mixtures are discussed further in Georg et al. (2020) (chapter 2).

To satisfy the above criteria, analysis of the transient antenna current has been investigated as a potential non-intrusive technique through several works. Initially, Chadwick et al. (2016) identified that distinct perturbations to the coil current amplitude and frequency could be observed and used to qualitatively assess the inductive coupling. Subsequently, Georg et al. (2020) (chapter 2) considered a range of propellant gases as well as simultaneous measurements of the emitted light intensity, though these assessments were still qualitative in nature. Most recently, Georg et al. (2021) (chapter 3) considered a range of propellants, flow rates and input powers and drew a connection between the transient current phenomena and the system power efficiencies. Finally, in this work, a quantitative relationship is developed. The results are of a ‘global’ or ‘zero-dimensional’ nature, unlike the results of OES or LIF which are spatially resolved.

The complex impedance of the antenna–plasma system is determined from high-sampling-frequency measurements of the antenna current and a simple transformer model of the antenna–plasma inductive coupling. The real part of the impedance is determined from the current amplitude and the imaginary part (related to inductance) from the current frequency. Knowing the variation of the impedance over time, various plasma parameters can be determined through the aid of the transformer model, such as the induced plasma current, the plasma volume geometry (defined later), and

its electrical conductivity. A limitation of this technique is that it can only be applied to systems where the excitation is produced by an oscillating circuit whose resonant frequency depends on the effective inductance of the antenna. In such circuits the excitation frequency matches the resonant frequency, and changes as a symptom of inductive coupling (Auweter-Kurtz & Wegmann, 1999; Herdrich & Petkow, 2008; Chadwick et al., 2016).

4.2 Experimental setup

Experiments were conducted at the Institute for Space Systems (IRS) of the University of Stuttgart, Germany. IRS has an extensive history with large-scale inductively coupled plasmas through various iterations of their inductive plasma generators, primarily for re-entry simulation. The device considered in this work is IPG7 (Massuti-Ballester et al., 2013), which consists of a 300 mm long, 90 mm diameter quartz tube discharge chamber with 3 mm wall thickness (in this configuration). The antenna is a 5.5-turn helical coil with tubular cross section. The axial length of the coil is 130 mm and its pitch diameter is 104 mm. The coil cross section is formed by an outer diameter of 12 mm and an inner diameter of 8 mm. One end of the tube is attached to an injector head that injects the propellant material with swirl. The other end of the tube is attached to a vacuum tank, 3 m long and 2 m diameter. With flow, the vacuum tank pressure is approximately 10 to 30 Pa.

The antenna coil is driven by a Meissner oscillator (also known as Armstrong oscillator) resonant circuit without matching network. The circuit is driven by a 300 Hz modulated DC source and contains an RS 3300 CJ metal–ceramic triode vacuum tube. The circuit oscillates at a frequency determined by the LC tank formed by the inductance of the coil and the capacitance of a capacitor bank. The frequency can be changed by connecting or disconnecting individual capacitors, or by exchanging the coil with one with a different number of turns, however, in this work the coil is fixed at 5.5 turns and the capacitance at $5 \times 6\text{nF}$. The 300 Hz modulated DC input is generated by the full-wave rectification of the 50 Hz three-phase facility power. The level of modulation is such that transition to and from inductive coupling occurs in each 300 Hz cycle. This complex transient behaviour makes it possible to study repeated mode transitions, however, it also necessitates advanced diagnostic techniques.

IPG7 was designed as a propellant-flexible device and has been extensively tested with oxygen, carbon-dioxide, nitrogen and argon, as well as mixtures of the other propellants with argon (Chadwick et al., 2020). In this work, oxygen at various flow rates and various input powers is considered. Although in principle the method presented here is agnostic to the particular propellant used, oxygen gas was chosen because of the availability of previous modelling results which allows for comparison with our results.

4 Circuit model

The maximum input power of IPG7 is 180 kW at the plate of the triode, and the quartz tube is water-cooled to prevent failure. Calorimetry is performed on this water to calculate the power transfer through the tube wall, P_{tube} . A cavity calorimeter is placed in the vacuum tank to capture the plasma jet and estimate its power, P_{jet} (Chadwick et al., 2020; Herdrich & Petkow, 2008). The sum of the two provides an estimate for the power deposited in the plasma via the relation $P_{\text{plasma}} \gtrsim P_{\text{tube}} + P_{\text{jet}}$. Within the context of this work, these measurements provide a verification for the powers resulting from the model.

It will be shown in section 4.3.3 that all necessary model inputs can be obtained simply by measuring the coil current at a sufficiently high sampling frequency. A Hofer-Noser Karrer (HOKA) probe designed by Kametech AG (Karrer et al., 1999; Karrer et al., 2003) was used to measure the coil current. This probe was specially designed and selected to tolerate prolonged exposure to the high current and to support high sampling frequencies. A sampling frequency of 25 MHz was used over a capture period of 50 ms to facilitate accurate calculation of the characteristic frequency via short-time Fourier transform analysis. The coil current has a characteristic frequency in the range of 0.55 to 0.70 MHz and can reach an RMS value of approximately 1.5 kA. A moving-window RMS calculation was performed to obtain the RMS coil current as a function of time, $i_c(t)$. A short-time Fourier transform analysis was performed to obtain the characteristic frequency as a function of time, $f_{\text{char}}(t)$.

4.3 Circuit model

The following is a derivation of the circuit model used in this analysis. Some aspects of this derivation are specific to the experimental setup outlined in the previous section, e.g. the tubular shape of the plasma chamber and the helical shape of the antenna, however, it is possible to adapt the derivation to different circumstances. Hence, the particular equations developed here are relevant only for members of IRS's "IPG" family, but, the method is generally applicable to any inductively coupled plasma source driven by an oscillating circuit. For example, Melazzi and Lancellotti (2015) use their numerical tool to compare the impedance and power deposition of three antenna types seen in literature (denoted single-loop, Nagoya type-III and fractional helix). To account for one of these antenna types in the model presented here, one would need to determine the resistance and inductance of the antenna, either analytically, numerically or experimentally. Therefore, the model is reasonably adaptable to different experimental setups.

A simplified diagram of the resonant circuit is shown in figure 4.1 (left), wherein the transformer model is used to represent the inductively-coupled antenna-plasma system (Piejak et al., 1992; Gudmundsson & Lieberman, 1997). The current and potential at

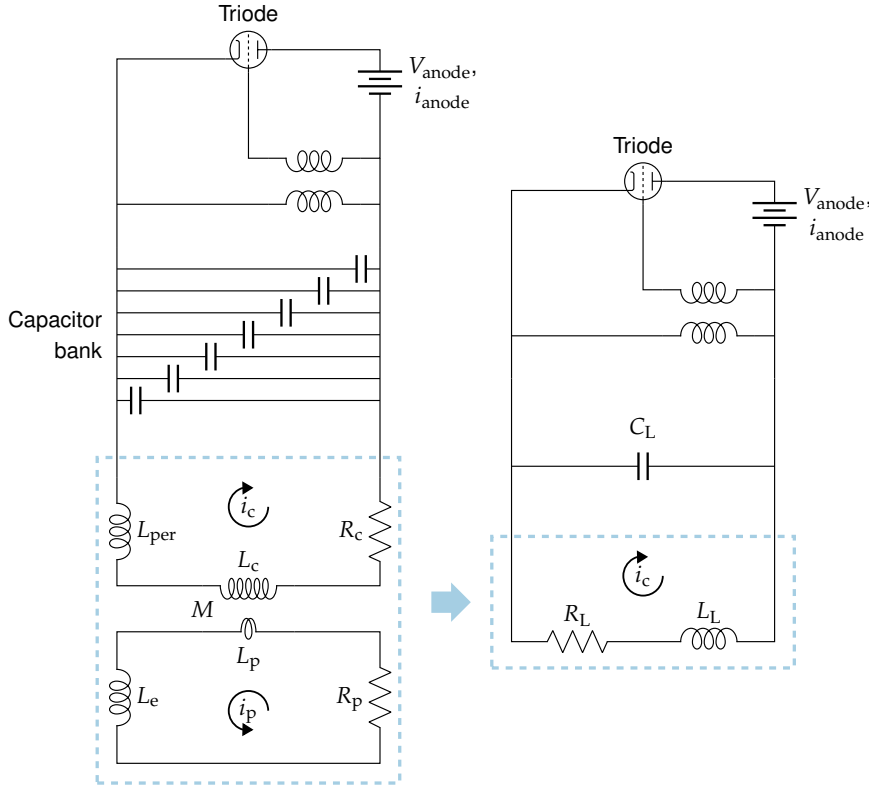


Figure 4.1: Resonant circuit with transformer model of the coil/plasma system (left) and lumped element equivalent circuit (right).

the anode of the triode are measured and yield the anode power P_{anode} . An oscillating current i_c passes through the coil, where R_c is the resistance of the coil and L_c is its self-inductance. On the plasma side, the plasma current i_p is a loop current that generates self-inductance L_p , and has a resistance R_p and an additional inductance L_e representing the electron inertia. Both currents oscillate at an angular frequency of ω , which is related to the experimental characteristic frequency by $\omega = 2\pi f_{\text{char}}$. For consistency, ω is used for the model parameter and f_{char} for the experimental measurement.

The circuit can be reduced to a lumped element equivalent, shown in figure 4.1 (right). The potential across the coil inductor is

$$\tilde{V}_c = j\omega L_c \tilde{i}_c + j\omega M \tilde{i}_p \quad (4.5)$$

The potential across the plasma inductor is

$$\tilde{V}_p = j\omega M \tilde{i}_c + j\omega L_p \tilde{i}_p = -\tilde{i}_p (R_p + j\omega L_e), \quad (4.6)$$

4 Circuit model

which can be rearranged to yield the normalised plasma current amplitude

$$i_p^* = \frac{|i_p|}{|i_c|} = \frac{M}{\sqrt{(R_p)^2 + (L_p + L_e)^2}}. \quad (4.7)$$

Substituting equation (4.6) into equation (4.5) and simplifying with equation (4.7), the equivalent impedance across the coil can be determined as

$$Z_c = \frac{\tilde{V}_c}{\tilde{i}_c} = j\omega L_c + (i_p^*)^2 (R_p - j\omega(L_p + L_e)). \quad (4.8)$$

Incorporating the series coil resistance R_c and peripheral inductance L_{per} yields the lumped equivalent impedance

$$Z_L = R_c + j\omega(L_c + L_{per}) + (i_p^*)^2 (R_p - j\omega(L_p + L_e)). \quad (4.9)$$

Equating equation (4.9) with $Z_L = R_L + j\omega L_L$, the lumped equivalent resistance and lumped equivalent inductance can be determined as

$$R_L = R_c + R_{p,eff} \quad (4.10)$$

and

$$L_L = L_c + L_{per} - L_{p,eff}, \quad (4.11)$$

where

$$L_{p,eff} = (i_p^*)^2 (L_p + L_e), \quad (4.12)$$

and

$$R_{p,eff} = (i_p^*)^2 R_p. \quad (4.13)$$

With lumped capacitance C_L equal to the sum of the individual capacitances, the frequency of the equivalent circuit can be determined by

$$\omega = \frac{1}{\sqrt{L_L C_L}}. \quad (4.14)$$

Grover (1962) provides a method for calculating L_c by first calculating the inductance of an infinitely-long cylindrical current sheet and then applying corrections for end effects and for large conductor cross-section (method shown in section 4.A). For

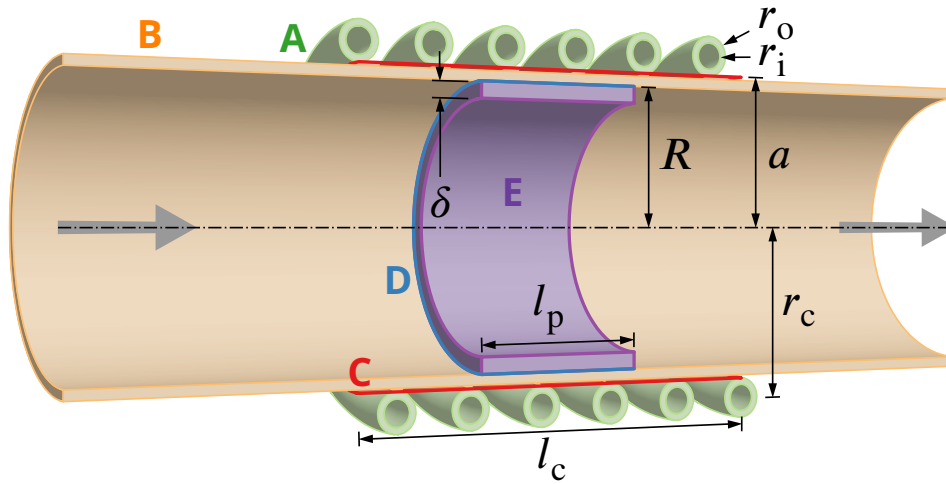


Figure 4.2: Sectional view of IPG7 showing the **5.5–turn helical coil (A)**, the **quartz tube discharge chamber (B)**, the **coil current represented as a zero-thickness current sheet (C)**, the **plasma current represented as a zero-thickness current sheet (D)** and the **plasma current represented as a uniform tubular volume (E)**. The current sheet representations are used to determine the plasma inductance (equation (4.24)) and the mutual inductance (equation (4.25)). The two different representations of the plasma current are used in different parts of the model as explained in-text. The labelled dimensions are all constant values with the exception of δ and l_p , which change as the plasma volume changes.

the coil geometry shown in figure 4.2, this yields $L_c = 1.788 \mu\text{H}$, which is 72.0 % of the uncorrected value. This is in close agreement with previous experimental measurements yielding $1.8 \mu\text{H}$ (Auweter-Kurtz & Wegmann, 1999; Herdrich, 2004). Previous analysis of experimental frequencies over a range of capacitances and with two different coil geometries yielded a series peripheral inductance $L_{\text{per}} = 0.75 \mu\text{H}$ (Herdrich & Petkow, 2008).

The capacitors in the capacitor bank may be connected or disconnected to alter the lumped capacitance, and therefore the frequency. In this work, 5 capacitors are connected, yielding $C_L = 5 \times 6 \text{ nF} = 30 \text{ nF}$. For a fully capacitive condition, $L_{p,\text{eff}} \rightarrow 0$, and equation (4.11) becomes $L_L = L_c + L_{\text{per}}$. Evaluating equation (4.14) with $L_L = 2.538 \mu\text{H}$ and $C_L = 30 \text{ nF}$ gives a frequency of 577 kHz. Experimental measurements of the frequency using FFT of the coil current under purely capacitive conditions yielded $585 \pm 2 \text{ kHz}$ (Georg et al., 2021 (chapter 3)).

To calculate the effective resistance of the coil, one must first calculate the direct-current resistance and then apply a correction factor to account for the skin effect losses at high-frequencies to get the alternating-current resistance (Stoll, 1974); this process is outlined in section 4.B. For the conditions under consideration and at a frequency

4 Circuit model

of 585 kHz, $R_{c,AC} = 17.3 \text{ m}\Omega$, which is 3497 % the value of $R_{c,DC}$. Although the frequency is not constant, its variation does not have a significant effect on the resistance, and therefore the constant value $R_c = 17.3 \text{ m}\Omega$ is used.

Integrating the azimuthal electric field \tilde{E}_θ around the plasma current loop gives the potential

$$\tilde{V}_p = 2 \pi R \tilde{E}_\theta . \quad (4.15)$$

Considering the plasma current as a uniform current density occurring in a tubular volume with length l_p and thickness δ , its magnitude can be calculated as

$$\tilde{i}_p = \sigma_p \tilde{E}_\theta l_p \delta , \quad (4.16)$$

where the plasma conductivity σ_p is given by

$$\sigma_p = \frac{\epsilon_0 \omega_{pe}^2}{\nu_{\text{eff}} + j \omega} , \quad (4.17)$$

and where ν_{eff} is an effective collisional and stochastic heating frequency, and the plasma frequency ω_{pe} satisfies

$$\omega_{pe}^2 = \frac{e^2 n}{\epsilon_0 m} . \quad (4.18)$$

Sequentially substituting equations (4.16) to (4.18) into equation (4.15) will eventually give

$$Z_p = \frac{\tilde{V}_p}{\tilde{i}_p} = \frac{2 \pi m}{l_p^* \delta^* e^2 n R} (\nu_{\text{eff}} + j \omega) , \quad (4.19)$$

where $l_p^* = l_p/R$ and $\delta^* = \delta/R$. This can be equated to $Z_p = R_p + j \omega L_e$ to give expressions for the plasma resistance and electron inertia inductance

$$R_p = \frac{2 \pi m \nu_{\text{eff}}}{l_p^* \delta^* e^2 n R} \quad (4.20)$$

$$L_e = \frac{2 \pi m}{l_p^* \delta^* e^2 n R} . \quad (4.21)$$

Noting that $R_p = L_e \nu_{\text{eff}}$ and defining $\nu_{\text{eff}}^* = \nu_{\text{eff}}/\omega$ means that $R_p = L_e \nu_{\text{eff}}^* \omega$, which can be substituted into equation (4.7) such that

$$i_p^* = \frac{M}{\sqrt{(L_e \nu_{\text{eff}}^*)^2 + (L_p + L_e)^2}} , \quad (4.22)$$

removing the dependence on ω . Substituting equation (4.11) into equation (4.14) gives an expression for ω which can be normalised by the capacitive ($L_{p,\text{eff}} = 0$) case to give

$$\omega^* = \frac{\omega}{\omega_{\text{cap}}} = \left(1 - \frac{L_{p,\text{eff}}}{L_c + L_{\text{per}}}\right)^{-\frac{1}{2}}. \quad (4.23)$$

For a cylindrical current sheet approximation of the plasma current, the axial magnetic field at the centre is $H_{z,p} = i_p/l_p$ where l_p is the axial length of the plasma current. Assuming the plasma current is located close to the tube wall (radius of R) and assuming uniform $H_{z,p}$, the plasma inductance defined in terms of magnetic flux through the plasma current becomes

$$L_p = \frac{\phi_{pp}}{i_p} = \frac{\mu_0 \pi R}{l_p^*}. \quad (4.24)$$

Assuming uniform $H_{z,c}$, the mutual inductance found as the inductance of the plasma due to the coil is

$$M = L_c \frac{\pi R^2 N_p}{\pi a^2 N_c} = \frac{L_c}{N_c} \frac{1}{(a^*)^2}, \quad (4.25)$$

where a is the radial location of the inner coil surface ($a^* = a/R$), N_p is the number of plasma current turns ($= 1$) and N_c is the number of coil turns.

The set of equations developed so far have a unique solution when the constant parameters and four free parameters (δ^* , l_p^* , v_{eff}^* and n) are provided. The number of free parameters can be reduced by assuming either collisionless or collisional regime and using the relevant equation for the skin depth δ . This process is shown below for both collisionless and collisional regimes for completeness, although only the collisional regime is relevant to the results shown later.

4.3.1 Collisionless

Under collisionless conditions ($v_{\text{eff}}^* \ll 1$) the skin depth is given by

$$\delta = \left(\frac{m}{e^2 \mu_0 n}\right)^{\frac{1}{2}} \quad (\text{Lieberman \& Lichtenberg, 2005}), \quad (4.26)$$

which, along with equations (4.20), (4.21) and (4.24), reduces equation (4.22) to

$$i_p^* = \frac{M}{L_p \sqrt{(2 \delta^* v_{\text{eff}}^*)^2 + (1 + 2 \delta^*)^2}}, \quad (4.27)$$

4 Circuit model

equation (4.12) to

$$L_{p,\text{eff}} = \frac{M^2 (1 + 2 \delta^*)}{L_p ((2 \delta^* v_{\text{eff}}^*)^2 + (1 + 2 \delta^*)^2)}, \quad (4.28)$$

and equation (4.13) to

$$R_{p,\text{eff}} = \frac{M^2 \omega (2 \delta^* v_{\text{eff}}^*)}{L_p ((2 \delta^* v_{\text{eff}}^*)^2 + (1 + 2 \delta^*)^2)}. \quad (4.29)$$

Note that $L_{p,\text{eff}}$ is a function only of l_p^* , δ^* and v_{eff}^* , and the latter can even be removed under the assumption of $v_{\text{eff}}^* \ll 1$ using $2 \delta^* v_{\text{eff}}^* \rightarrow 0$, although this will not work for $R_{p,\text{eff}}$. Therefore ω^* is a function of only two free parameters.

4.3.2 Collisional

Under collisional conditions ($v_{\text{eff}}^* \gg 1$) the skin depth is given by

$$\delta = \left(\frac{2 m v_{\text{eff}}^*}{e^2 \mu_0 n} \right)^{\frac{1}{2}} \quad (\text{Lieberman \& Lichtenberg, 2005}). \quad (4.30)$$

This, along with equations (4.20), (4.21) and (4.24), reduces equation (4.22) to

$$i_p^* = \frac{M}{L_p \sqrt{(\delta^*)^2 + (1 + \delta^*/v_{\text{eff}}^*)^2}}, \quad (4.31)$$

equation (4.12) to

$$L_{p,\text{eff}} = \frac{M^2 (1 + \delta^*/v_{\text{eff}}^*)}{L_p ((\delta^*)^2 + (1 + \delta^*/v_{\text{eff}}^*)^2)}, \quad (4.32)$$

and equation (4.13) to

$$R_{p,\text{eff}} = \frac{M^2 \omega (\delta^*)}{L_p ((\delta^*)^2 + (1 + \delta^*/v_{\text{eff}}^*)^2)}. \quad (4.33)$$

In this case, with the assumption of $v_{\text{eff}}^* \gg 1$, $\delta^*/v_{\text{eff}}^* \rightarrow 0$ can be used to eliminate v_{eff}^* completely so that both $L_{p,\text{eff}}$ and $R_{p,\text{eff}}$ are functions only of l_p^* and δ^* . The solution space for these assumptions is plotted in figure 4.3 over a range of l_p^* and δ^* .

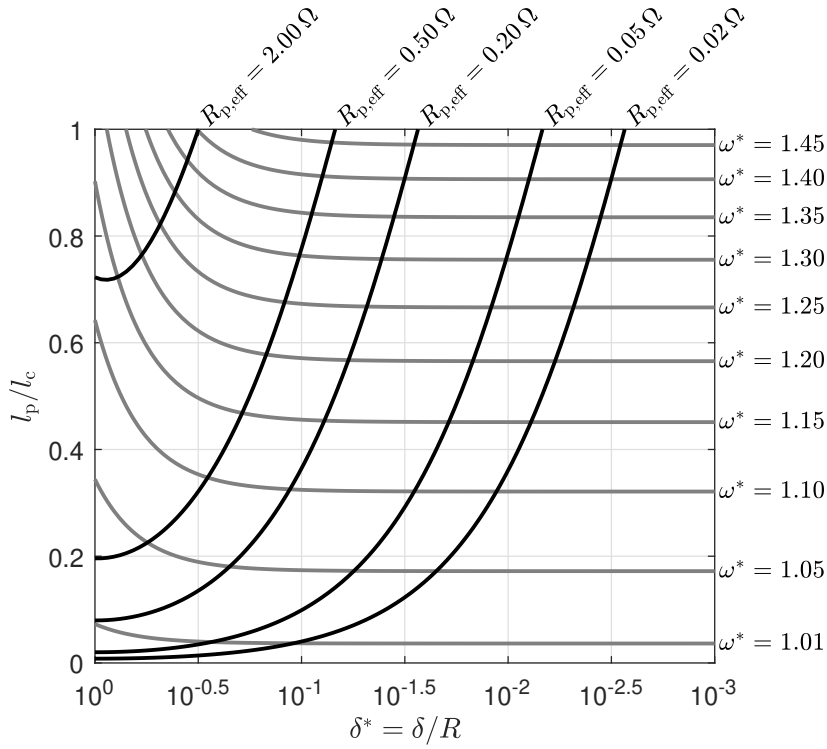


Figure 4.3: Solution space for the model under the assumption of a collisional regime using equations (4.23) to (4.25) and equations (4.32) and (4.33) with $\delta^*/v_{eff}^* \rightarrow 0$, showing that each point in $\omega-R_{p,eff}$ space maps to a point in $I_p-\delta$ space.

4.3.3 Solution method

A summary of the model constants, inputs and outputs is provided by table 4.1. The model solution method is shown diagrammatically by figure 4.4, including which outputs are calculable for which inputs. A useful feature of the collisional assumption is the fact that almost all outputs can be calculated without knowledge of v_{eff} , which is a relatively difficult parameter to estimate. A collisional regime is assumed for the remainder of this work since it corresponds to the experimental conditions (high pressure in the discharge chamber).

Since the model has been reduced to only two free parameters, I_p and δ , two input variables are needed to define a unique solution. For this purpose, the relative frequency shift of the coil current $\omega^*(t)$ is used along with the plasma effective resistance $R_{p,eff}(t)$. A short-time Fourier transform analysis was conducted to obtain $f_{char}(t)$ from the experimental measurements of the coil current. Fitting was also conducted to obtain $f_{char,cap}(t)$, which is the predicted coil current frequency if there were no fluctuation

Table 4.1: Summary of model parameters classified as either constant, input or output.

Parameter	Symbol	Units	Non-dimensional
Constant			
– Inner radius of quartz tube	R	m	—
– Inner radius of coil	a	m	$a^* = a/R$
– Number of coil turns	N_c	—	—
– Coil self-inductance	L_c	H	—
– Peripheral inductance	L_{per}	H	—
– Lumped capacitance	C_L	F	—
– Coil resistance	R_c	Ω	—
Input			
– Skin depth	δ	m	$\delta^* = \delta/R$
– Plasma current axial length	l_p	m	$l_p^* = l_p/R$
– Effective collisional and stochastic heating frequency	ν_{eff}	rad s^{-1}	$\nu_{eff}^* = \nu_{eff}/\omega$
Output			
– Plasma self-inductance	L_p	H	—
– Characteristic frequency	ω	rad s^{-1}	$\omega^* = \omega/\omega_{cap}$
– Plasma loop current	i_p	A	$i_p^* = i_p/i_c$
– Electron number density	n	m^{-3}	—
– Plasma resistance	R_p	Ω	—
– Electron inertia inductance	L_e	H	—
– Plasma conductivity	σ	S m^{-1}	—
– Lumped potential	V_L	V	—

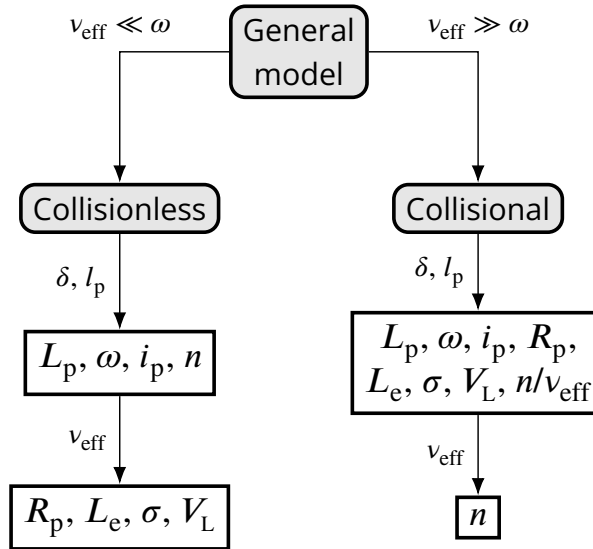


Figure 4.4: Model solution method. Firstly, either collisionless or collisional assumption must be made. Secondly, δ and l_p must be provided to solve for ω and other outputs. Finally, for a complete solution ν_{eff} must be provided.

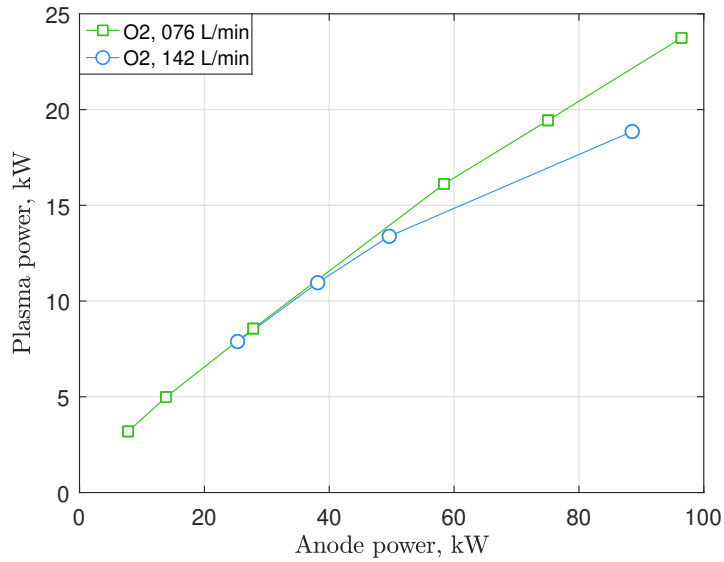


Figure 4.5: Plasma power against anode (input) power. Plasma power was calculated by summing the experimental calorimetric powers (jet and tube) (Chadwick, 2017).

due to inductive coupling. The relative frequency shift is then calculated according to

$$\omega^*(t) = \frac{f_{\text{char}}(t)}{f_{\text{char, cap}}(t)}. \quad (4.34)$$

$R_{\text{p,eff}}(t)$ was obtained by considering the current drop that is observed when the dominant coupling regime transitions from capacitive to inductive coupling. The power supply was modelled as a voltage source that provides a particular profile of $V_L(t)$ at a particular value of V_{anode} . The effective plasma resistance was found by

$$R_{\text{p,eff}}(t) = \frac{V_L(t)}{i_c(t)} - R_c. \quad (4.35)$$

For each condition, $V_L(t)$ was determined such that the average absorbed plasma power over time equalled the experimental calorimetric power, where the absorbed plasma power is given by $P_{\text{plasma}}(t) = R_{\text{p,eff}}(t) i_c^2(t)$. The experimental calorimetric powers are shown in figure 4.5.

It can be seen in figure 4.3 that each isoline of ω^* intersects each isoline of $R_{\text{p,eff}}$ exactly once. Therefore, the curves of $\omega^*(t)$ and $R_{\text{p,eff}}(t)$ can be transformed into curves of $l_p(t)$ and $\delta^*(t)$, which completely defines the free parameters of the model. This process was used to produce the results in the following section.

Table 4.2: Summary of experimental conditions considered in this work (collected by Chadwick (2017)). Values are averaged over time. Volumetric flow rate \dot{V} is for standard conditions 0 °C and 1 atm.

Legend	Propellant			Anode			Coil		Calorimetry	
	\dot{V} L min ⁻¹	\dot{m} g s ⁻¹	\dot{n} mol s ⁻¹	U_{anode} kV	I_{anode} A	P_{anode} kW	$i_{\text{c,RMS}}$ kA	f_{char} kHz	P_{tube} kW	P_{jet} kW
	76	1.81	0.057	2.5	3.1	7.8	0.418	587	2.20	0.99
	3.1	4.5	13.9	0.466	590	3.47	1.52
	4.1	6.9	27.8	0.609	593	5.93	2.63
	5.0	11.7	58.4	0.641	601	8.49	7.63
	5.5	13.7	75.0	0.680	604	9.53	9.91
	6.0	16.1	96.4	0.720	607	10.68	13.06
	142	3.38	0.106	4.3	5.9	25.3	0.718	586	6.06	1.83
	5.0	7.7	38.2	0.764	589	7.58	3.38
	5.5	9.1	49.6	0.821	591	8.63	4.75
	6.0	14.8	88.5	0.755	599	5.99	12.86

4.4 Results & discussion

Two experimental datasets collected by Chadwick (2017) were analysed using the method discussed in section 4.3.3. In each dataset, pure oxygen propellant gas was used and the anode potential (which defines the input power) was increased incrementally. The system was allowed to stabilise at each new anode potential before data acquisition. The two datasets differ by the flow rate of propellant gas. The first dataset has a flow rate of 76 L min⁻¹ and anode potentials of 2.5 kV, 3.1 kV, 4.1 kV, 5.0 kV, 5.5 kV and 6.0 kV, and the second has a flow rate of 142 L min⁻¹ and anode potentials of 4.3 kV, 5.0 kV, 5.5 kV and 6.0 kV. The lowest anode potential in each set corresponds to the lowest input power at which inductive coupling was observed as evidenced by the fluctuation of the coil current and frequency. The experimental conditions considered are summarised in table 4.2.

The model input parameters over time are shown in figure 4.6. For each condition, curves of ω and $R_{\text{p,eff}}$ were produced from the coil current measurements, and are shown in subfigures (a1–2), and (b1–2), respectively. These curves were transformed into curves of I_{p} and δ , which are shown in subfigures (c1–2), and (d1–2), respectively.

Finally, the volume of the plasma (as defined in figure 4.2) is shown in subfigures (e1–2).

At the lowest anode potentials, the curves of ω show a small peak occurring at approximately 1.3 ms. The peak increases and spreads as the anode potential increases through 2.5 kV, 3.1 kV, 4.1 kV and 5.0 kV for 76 L min^{-1} and through 4.3 kV, 5.0 kV and 5.5 kV for 142 L min^{-1} . For subsequent anode potentials, the curves of ω stop increasing and instead increase and spread significantly, so the period of inductive coupling becomes much longer, approaching 60 % of the cycle period.

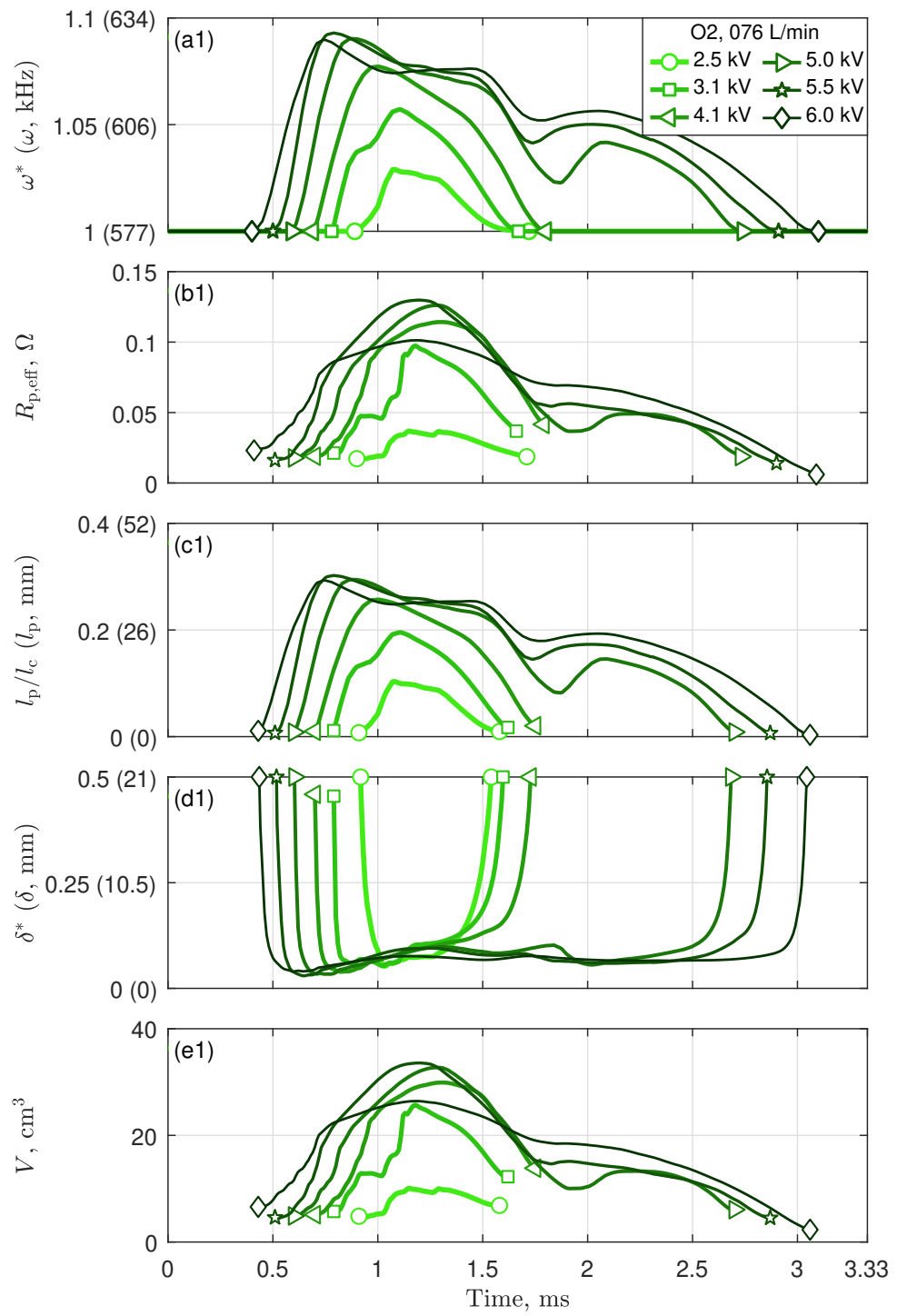
The curves of $R_{p,\text{eff}}$ exhibit similar trends, although they are defined only for periods of inductive coupling. The undefined periods are due to a breakdown of the model assumptions. Namely, the assumption of strong inductive coupling between the coil and plasma leading to $\delta^* \ll 1$ and a thin, tubular plasma volume with thickness δ is not satisfied. For this reason, all subsequent model parameters are defined only when $R_{p,\text{eff}}$ is defined. This is seen clearly for the curves of l_p which match those of ω in appearance. The cause of the aforementioned undefined periods is shown clearly by the curves of δ , which tends towards infinity at the start and end of inductive coupling, with a relatively stable finite value in between. Interestingly, for the 142 L min^{-1} , 5.5 kV condition, there are two periods of inductive coupling in quick succession, with the latter having a lesser intensity. The curves of V result from the l_p and δ curves, and closely resemble those of $R_{p,\text{eff}}$. For comparison, the portion of the discharge chamber that is enclosed by the coil has a volume of 720 cm^3 , and 5 % of that value is 36 cm^3 . Because δ is fairly stable over the inductive period, changes in V are strongly dependent on l_p . Practically, this means that the plasma volume elongates and shortens, but does not encroach on the central region, hence the portion of flow that passes through that volume (and becomes heated) will always be relatively small.

The model outputs parameters over time are shown in figure 4.7. The quantity n/v_{eff}^* results from equation (4.30) and is shown in subfigures (a1–2). The real electrical conductivity is shown in subfigures (b1–2). The ratio of induced plasma current to coil current, i_p^* , is shown in subfigures (c1–2). Finally, absorbed power in the plasma is shown in subfigures (d1–2).

For each condition, n/v_{eff}^* quickly reaches its maximum value before slowly reducing back to zero. For both flow rates, the maximum value increases with anode potential, with the exception of the last conditions. While it is not possible to determine n or v_{eff}^* separately without an additional input, it is possible to estimate the range of v_{eff}^* with the aid of some reasonable assumptions, and therefore verify that the results are consistent with the earlier assumption of a collisional regime ($v_{\text{eff}}^* \gg 1$). The ionisation degree of the plasma volume can be defined as

$$\psi = \frac{n}{n_0} = \frac{n/v_{\text{eff}}^*}{n_0} v_{\text{eff}}^*, \quad (4.36)$$

4 Circuit model



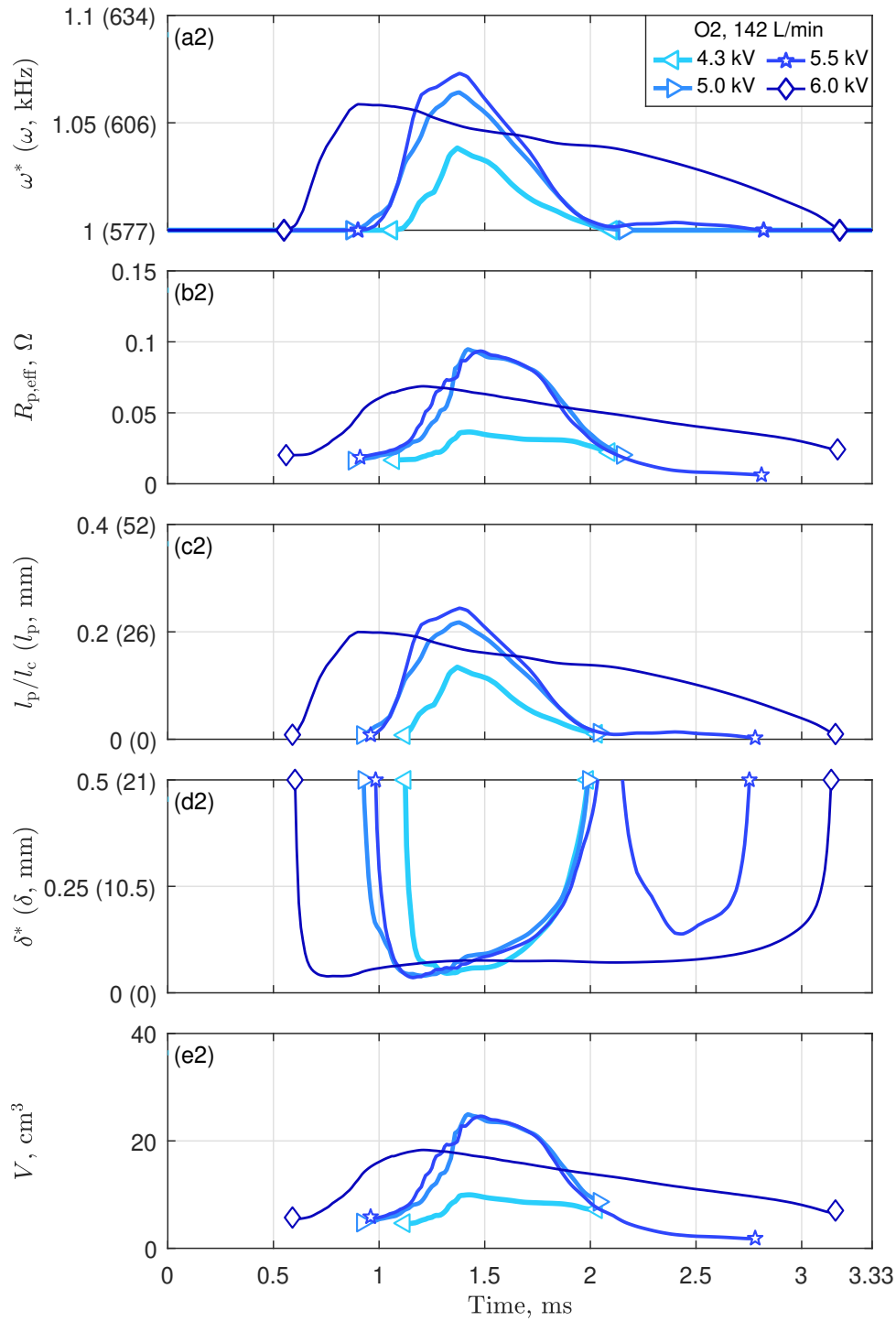
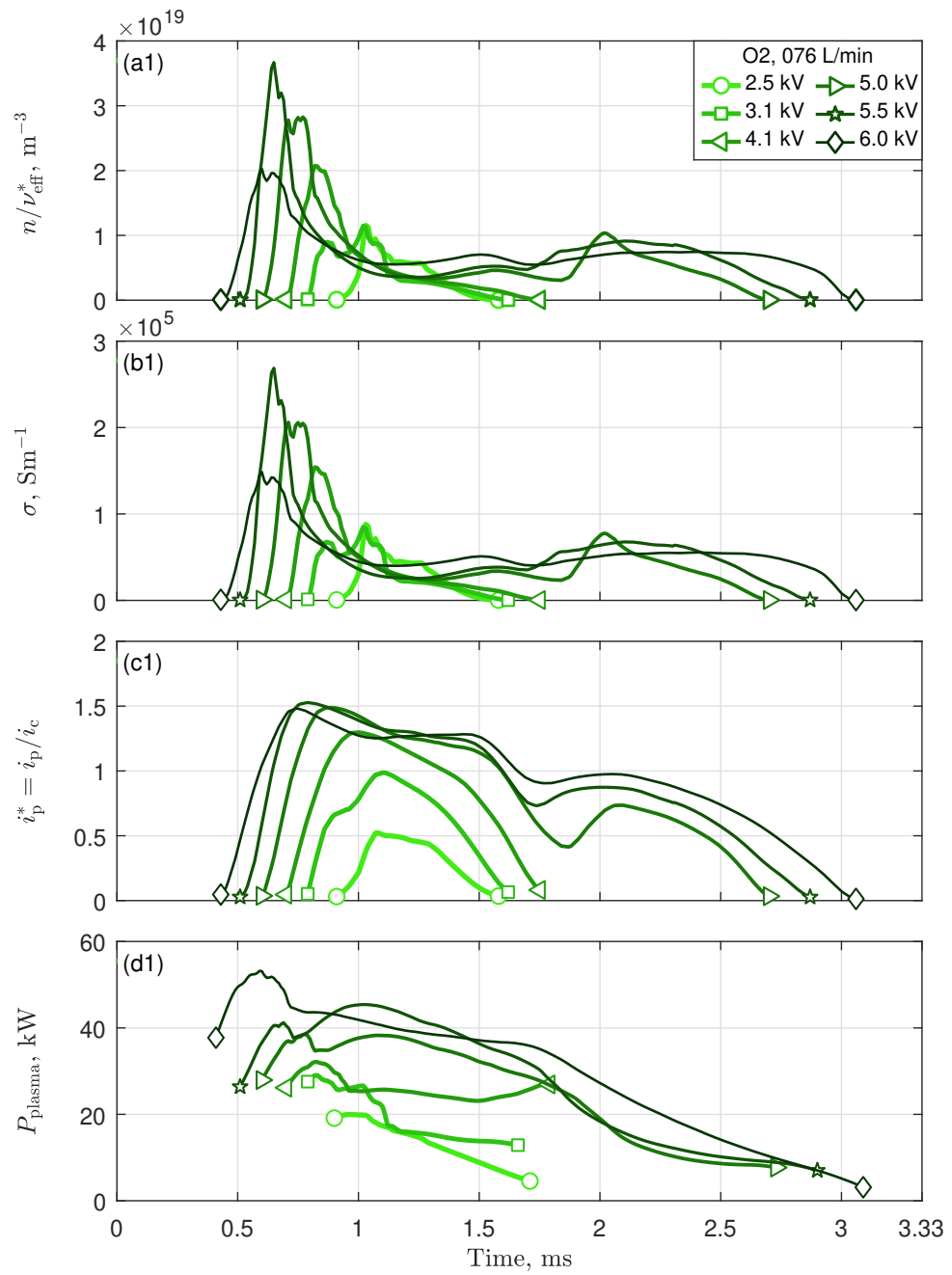


Figure 4.6: Time series of model input parameters over the period of a 300 Hz cycle for oxygen at various anode potentials (input powers) and flow rates. ω is the antenna current characteristic frequency, $R_{p,\text{eff}}$ is the effective plasma resistance, l_p is the axial length of the plasma volume, δ is the skin depth, and V is the volume of the plasma volume (function of l_p and δ).

4 Circuit model



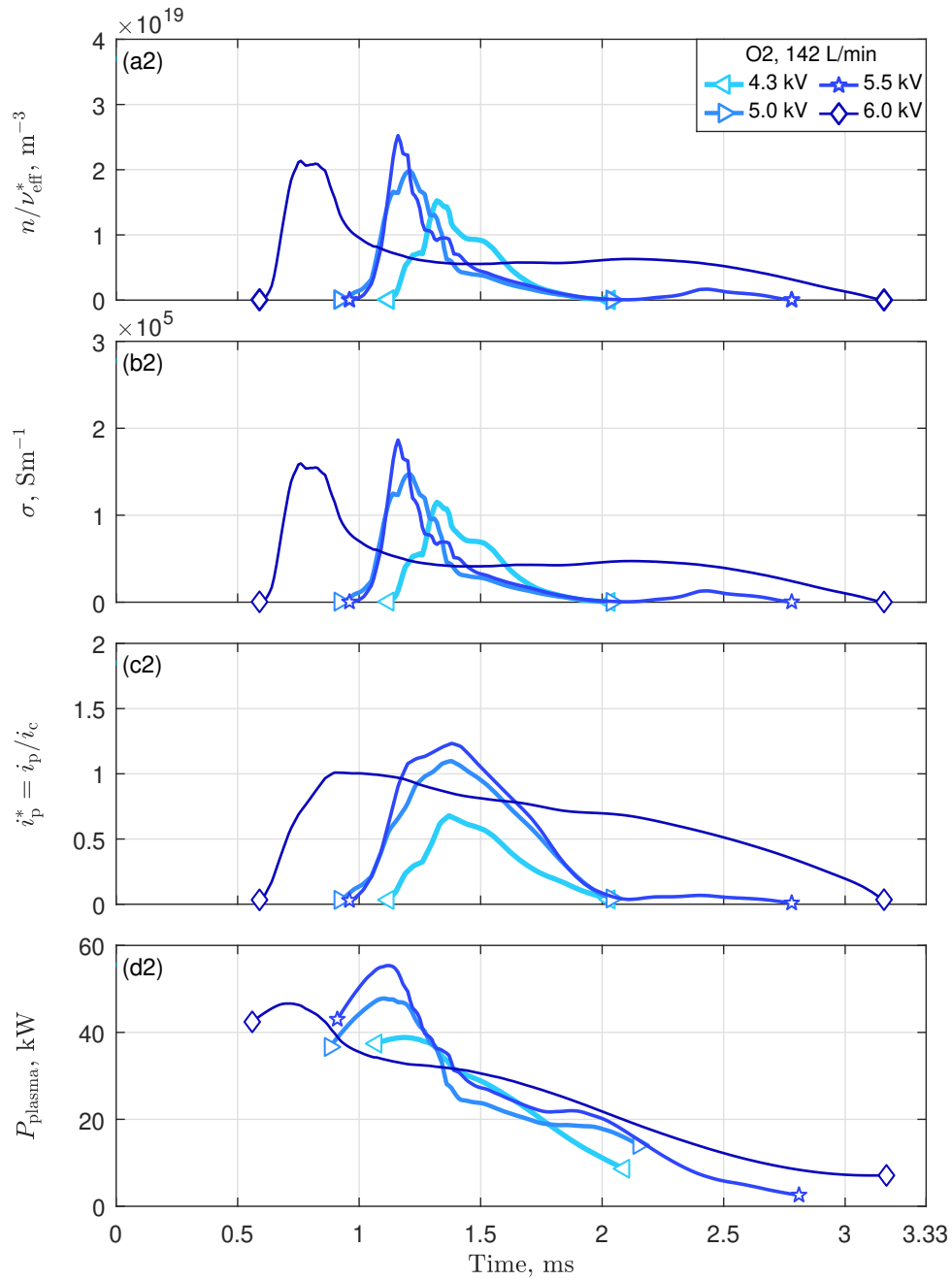


Figure 4.7: Time series of model output parameters over the period of a 300 Hz cycle for oxygen at various anode potentials (input powers) and flow rates. n/v_{eff}^* is the electron density over the normalised collision frequency, σ is the plasma electrical conductivity, i_p^* is the plasma current normalised by the antenna current, and P_{plasma} is the power deposited into the plasma (function of $R_{p,\text{eff}}$ and i_c).

Table 4.3: Comparison of parameter extrema for lowest and highest input powers at each flow rate. The lowest power conditions correspond to the lowest input power (anode potential) which produced stable inductive coupling. The anode potential of the lowest power condition is dependent on flow rate, hence here they take different values (2.4 kV for 76 L min⁻¹ and 4.3 kV for 142 L min⁻¹). The maximum value for each parameter is shown, with the exception of δ , for which the minimum is shown.

Parameter		Lowest power condition		Highest power condition	
		76 L min ⁻¹	142 L min ⁻¹	76 L min ⁻¹	142 L min ⁻¹
		(2.4 kV)	(4.3 kV)	(6.0 kV)	(6.0 kV)
ω^*	—	1.03	1.04	1.09	1.06
$R_{p,\text{eff}}$	m Ω	36.9	36.5	101	68.7
l_p	mm	13.5	17.5	38.1	26.0
δ	mm	2.21	1.93	1.67	1.63
V	cm ³	10.1	9.96	26.4	18.3
n/v_{eff}^*	$\times 10^{19}$ m ⁻³	1.16	1.52	2.03	2.14
σ	$\times 10^5$ S m ⁻¹	0.88	1.15	1.49	1.60
i_p	kA	0.40	0.68	1.24	0.99
P_{plasma}	kW	20.0	38.8	53.2	46.6

where n_o is the atomic oxygen density. Assuming full dissociation of the molecular oxygen, the atomic oxygen density can be estimated by applying the ideal gas law with a pressure of 500 to 1500 Pa and a temperature of 1×10^3 to 1×10^4 K to yield n_o of 3.6×10^{21} to 1.1×10^{23} m⁻³. The maxima of n/v_{eff}^* lie in the range 1×10^{19} to 4×10^{19} m⁻³. Assuming significant ionisation (ψ of 0.5 to 1), according to equation (4.36) v_{eff}^* lies in the range of 45 to 11,000, which satisfies the collisional assumption.

The curves of the electrical conductivity of the plasma, σ , resemble those of n/v_{eff}^* . The maxima increase as the anode potential increases, with the exception of the highest anode potential conditions. According to Figure 6.3-1 from Herdrich (2004), the electrical conductivity of an oxygen plasma in a near-identical plasma generator lies in the range of 3×10^3 to 5×10^3 S m⁻¹ under comparable conditions. Since that work considered the plasma discharge as a steady phenomenon, comparisons must be made with time-averaged values. The range of time-averaged σ for the model results is 2.7×10^4 to 5.4×10^4 S m⁻¹. The relative difference is one order of magnitude, which is a relatively good agreement considering the significant differences between the two

modelling approaches—i.e. the steady state assumption and 20 mm thermal boundary layer used in that other work (Herdrich, 2004).

The relative induced plasma current i_p^* increases with anode potential, similar to ω . At higher powers the value of i_p^* exceeds 1, which indicates that at those times the plasma current exceeds the coil current in amplitude. The curves of P_{plasma} take a distinctive form since i_c and $R_{p,\text{eff}}$ are both non-zero at the start and end of inductive coupling. This is a symptom of the model's inability to capture the transition from no inductive coupling to $\delta^* \ll 1$. The curves clearly show that the peak power deposition occurs at the early part of the inductive coupling.

Some results from figures 4.6 and 4.7 are shown in table 4.3, which presents the extrema of the model parameters for the lowest and highest anode potentials (input powers) at each flow rate. It can be said of ω , $R_{p,\text{eff}}$, l_p , V and i_p that the maxima increase with increasing anode potential, but decrease with flow rate at the high anode potential. The minima of δ are relatively stable across flow rate and only decrease slightly as the anode potential increases. For n/v_{eff}^* and σ the maxima increase with higher anode potential and lower flow rate (this is evident more from the figure 4.7 rather than from table 4.3). Finally, P_{plasma} is unique in that it increases strongly as a function of anode potential for the lower flow rate but less strongly for the higher flow rate.

4.5 Conclusion

In this work the transient antenna current method has been expanded to yield time-varying properties of an inductively coupled oxygen plasma. The technique presented is propellant-agnostic and can in principle be applied to other monatomic and molecular propellants. The technique is based on the transformer model of an inductive plasma and essentially links the resonant frequency of the antenna–plasma circuit to the effective impedance of the plasma. Time-varying plasma properties such as plasma volume, electrical conductivity and deposited power were investigated for various input powers and flow rates. Compared to contemporary non-intrusive plasma diagnostic techniques, such as optical emission spectroscopy and laser-induced fluorescence, the method presented is suitable for arbitrary propellant species and mixtures albeit at a much lower fidelity of output. The reduced outputs are justified by the model's flexibility of application and reduced a priori assumptions. Future work comparing the results of this model to experimental measurements (such as the electron density) would assist greatly in its improvement and validation for further use.

Acknowledgements

The authors would like to thank the German Research Foundation for their financial contributions to the experimental campaign under Project HE 4563/3-1.

This research is supported by an Australian Government Research Training Program (RTP) Scholarship.

Research undertaken for this report has been assisted with a grant from the Sir Ross and Sir Keith Smith Fund (Smith Fund) (www.smithfund.org.au). The support is acknowledged and greatly appreciated. The Smith Fund, by providing funding for this project, does not verify the accuracy of any findings or any representations contained in it. Any reliance on the findings in any written report or information provided to you should be based solely on your own assessment and conclusions. The Smith Fund does not accept any responsibility or liability from any person, company or entity that may have relied on any written report or representations contained in this report if that person, company or entity suffers any loss (financial or otherwise) as a result.

References

- Auweter-Kurtz, M., & Wegmann, T. (1999). Overview of IRS plasma wind tunnel facilities. *RTO AVT Course on "Measurement Techniques for High Enthalpy and Plasma Flows"*.
- Böhrk, H., & Auweter-Kurtz, M. (2006). Preliminary Results of TIHTUS Operation. *42nd AIAA/ASME/SAE/ASEE Joint Propulsion Conference & Exhibit*, AIAA 2006-5158. <https://doi.org/10.2514/6.2006-5158>
- Chadwick, A. R. (2017). *Performance of Alternative Propellants in an Inductive Electric Propulsion System* (Ph.D. Thesis). The University of Adelaide. <http://hdl.handle.net/2440/119192>
- Chadwick, A. R., Dally, B. B., Herdrich, G., & Kim, M. (2020). High-power inductive electric propulsion operation with alternative propellants. *The Aeronautical Journal*, 124(1272), 151–169. <https://doi.org/10.1017/aer.2019.141>
- Chadwick, A. R., Herdrich, G., Kim, M., & Dally, B. B. (2016). Transient electromagnetic behaviour in inductive oxygen and argon-oxygen plasmas. *Plasma Sources Science and Technology*, 25(6). <https://doi.org/10.1088/0963-0252/25/6/065025>
- Georg, R., Chadwick, A. R., Dally, B. B., & Herdrich, G. (2020). Resolving transient discharge cycle behaviour in modulated inductive plasmas. *Vacuum*. <https://doi.org/10.1016/j.vacuum.2020.109636>

- Georg, R., Chadwick, A. R., Dally, B. B., & Herdrich, G. (2021). Power efficiency estimation of an inductive plasma generator using propellant mixtures of oxygen, carbon-dioxide and argon. *Acta Astronautica*, 179(November 2020), 536–545. <https://doi.org/10.1016/j.actaastro.2020.11.020>
- Grover, F. W. (1962). *Inductance Calculations: Working Formulas and Tables* (Vol. 18). Dover Publications.
- Gudmundsson, J. T., & Lieberman, M. A. (1997). Magnetic induction and plasma impedance in a cylindrical inductive discharge. *Plasma Sources Science and Technology*, 6(4), 540–550. <https://doi.org/10.1088/0963-0252/6/4/012>
- Herdrich, G. (2004). *Construction, qualification and characterisation of an inductively heated plasma wind-tunnel system to simulate atmospheric entry (Aufbau, Qualifikation und Charakterisierung einer induktiv beheizten Plasmawindkanalanlage zur Simulation atmosphärischer)* (Ph.D. Thesis). Universität Stuttgart.
- Herdrich, G., Bauder, U., Boxberger, A., Gabrielli, R. A., Lau, M., Petkow, D., Pfeiffer, M., Syring, C., & Fasoulas, S. (2013). Advanced plasma (propulsion) concepts at IRS. *Vacuum*, 88(1), 36–41. <https://doi.org/10.1016/j.vacuum.2012.02.032>
- Herdrich, G., & Petkow, D. (2008). High-enthalpy, water-cooled and thin-walled ICP sources characterization and MHD optimization. *Journal of Plasma Physics*, 74(3), 391–429. <https://doi.org/10.1017/S0022377807006927>
- Isayama, S., Shinohara, S., & Hada, T. (2018). Review of helicon high-density plasma: Production mechanism and plasma/wave characteristics. *Plasma and Fusion Research*, 13, 1–27. <https://doi.org/10.1585/PFR.13.1101014>
- Karrer, N., Hofer-Noser, P., Herdrich, G., & Auweter-Kurtz, M. (2003). Isolated current probe for continuous monitoring of AC currents of high amplitude and high frequency. *European Power Electronics Conference*.
- Karrer, N., Hofer-Noser, P., & Henrard, D. (1999). HOKA: a new isolated current measuring principle and its features. *Conference Record of the 1999 IEEE Industry Applications Conference. Thirty-Forth IAS Annual Meeting (Cat. No.99CH36370)*, 3, 2121–2128. <https://doi.org/10.1109/IAS.1999.806028>
- Kralkina, E. A., Nekliudova, P., Pavlov, V., Vavilin, K., Zadiriev, I., & Zhao, C. (2020). Experimental study of a low-pressure hybrid RF discharge. *Plasma Science and Technology*, 22(5), 055405. <https://doi.org/10.1088/2058-6272/ab69bd>
- Lieberman, M. A., & Lichtenberg, A. J. (2005). *Principles of Plasma Discharges and Materials Processing*. John Wiley & Sons, Inc. <https://doi.org/10.1002/0471724254>
- Magarotto, M., & Pavarin, D. (2020). Parametric Study of a Cathode-Less Radio Frequency Thruster. *IEEE Transactions on Plasma Science*, 48(8), 1–13. <https://doi.org/10.1109/TPS.2020.3006257>
- Massuti-Ballester, B., Marynowski, T., & Herdrich, G. (2013). New Inductively Heated Plasma Source IPG7. *Frontier of Applied Plasma Technology*, 6(2).

4 Circuit model

- Melazzi, D., & Lancellotti, V. (2015). A comparative study of radiofrequency antennas for Helicon plasma sources. *Plasma Sources Science and Technology*, 24(2), 25024. <https://doi.org/10.1088/0963-0252/24/2/025024>
- Navarro-Cavallé, J., Wijnen, M., Fajardo, P., & Ahedo, E. (2018). Experimental characterization of a 1 kW Helicon Plasma Thruster. *Vacuum*, 149, 69–73. <https://doi.org/10.1016/j.vacuum.2017.11.036>
- Piejak, R. B., Godyak, V. A., & Alexandrovich, B. M. (1992). A simple analysis of an inductive RF discharge. *Plasma Sources Science and Technology*, 1(3), 179–186. <https://doi.org/10.1088/0963-0252/1/3/006>
- Romano, F., Chan, Y.-A., Herdrich, G., Traub, C., Fasoulas, S., Roberts, P., Smith, K., Edmondson, S., Haigh, S., Crisp, N., Oiko, V., Worrall, S., Livadiotti, S., Huyton, C., Sinpetru, L., Straker, A., Becedas, J., Domínguez, R., González, D., ... Heißerer, B. (2020). RF Helicon-based Inductive Plasma Thruster (IPT) Design for an Atmosphere-Breathing Electric Propulsion system (ABEP). *Acta Astronautica*, 176(January), 476–483. <https://doi.org/10.1016/j.actaastro.2020.07.008>
- Sou, H., Takao, Y., Noutsuka, T., Mori, Y., Uemura, K., & Nakashima, H. (2000). Study of plasma propulsion system with RF heating. *Vacuum*, 59(1), 73–79. [https://doi.org/10.1016/S0042-207X\(00\)00256-6](https://doi.org/10.1016/S0042-207X(00)00256-6)
- Stoll, R. L. (1974). *The analysis of eddy currents (Monographs in electrical and electronic engineering)* (Hardcover). Clarendon Press.
- Takahashi, K. (2019). Helicon-type radiofrequency plasma thrusters and magnetic plasma nozzles. *Reviews of Modern Plasma Physics*, 3(1), 3. <https://doi.org/10.1007/s41614-019-0024-2>
- Tsifakis, D., Charles, C., & Boswell, R. (2020). An Inductively-Coupled Plasma Electrothermal Radiofrequency Thruster. *Frontiers in Physics*, 8(February), 1–10. <https://doi.org/10.3389/fphy.2020.00034>
- Vitucci, J. J. (2019). *Development and test of a superconducting helicon plasma thruster* (Ph.D. Thesis). University of Maryland.

Appendices

4.A Coil self-inductance calculation

Grover (1962) provides working formulae and tables for calculating the self and mutual inductances of various conductor arrangements. To determine the self-inductance of the helical coil mentioned in this work (L_c), it is necessary to first calculate the self-inductance of an infinitely long cylindrical current sheet, which is given by

$$L_0 = \mu_0 \frac{\pi r_c^2 N^2}{l_c}, \quad (4.37)$$

where r_c is the pitch radius of the coil, l_c is the axial length of the coil and N is the number of turns. The finite length of the coil is accounted for by a correction factor K such that

$$L_1 = L_0 K, \quad (4.38)$$

where K is tabulated as a function of the coil aspect ratio, $\beta = \frac{l_c}{2r_c}$ (pg. 143 in Grover (1962)). The large conductor cross-section is accounted for by the expression

$$L_2 = L_1 - \mu_0 r_c N (G + H), \quad (4.39)$$

where H is tabulated as a function of N (pg. 163 in Grover (1962)). G is given by

$$G = \frac{5}{4} - \ln \frac{l_c}{r_o N}, \quad (4.40)$$

where r_o is the outer radius of the conductor.

The geometric parameters of the coil used are $r_c = 52 \times 10^{-3}$ m, $N = 5.5$, $l_c = 130 \times 10^{-3}$ m and $r_o = 6 \times 10^{-3}$ m. Solving the above equations with these parameters yields $L_0 = 2.484 \mu\text{H}$, $\beta = 1.25$, $K = 0.7351$, $L_1 = 1.826 \mu\text{H}$, $G = -0.121$, $H = 0.225$ and $L_2 = 1.788 \mu\text{H}$. The value of L_2 is 72.0 % that of L_0 . In this work $L_c = L_2 = 1.788 \mu\text{H}$ is used for the self-inductance of the coil.

4.B Coil resistance calculation

The resistance of the coil under DC (or low-frequency) conditions is given by

$$R_{c,DC} = \frac{\rho_c l_{c,arc}}{\pi(r_o^2 - r_i^2)}, \quad (4.41)$$

where ρ_c is the resistivity of the coil conductor, r_i and r_o are the inner and outer conductor radii respectively, and the coil arc length is given by

$$l_{c,arc} = \sqrt{(2\pi N r_c)^2 + (l_c)^2}. \quad (4.42)$$

For AC (high-frequency) conditions, a correction factor must be used to account for the skin effect losses (Stoll, 1974)

$$\frac{R_{c,AC}}{R_{c,DC}} = \frac{r_o}{2\delta_c} + \frac{1}{4} + \frac{3\delta_c}{32r_o}, \quad (4.43)$$

which is itself a function of the coil conductor skin depth

$$\delta_c = \sqrt{\frac{2\rho_c}{\omega\mu_0}}. \quad (4.44)$$

The geometry parameters of the coil used are $r_o = 6 \times 10^{-3}$ m, $r_i = 4 \times 10^{-3}$ m, $N = 5.5$, $r_c = 52 \times 10^{-3}$ m and $l_c = 130 \times 10^{-3}$ m. The resistivity of copper is $\rho_c = 1.724 \times 10^{-8}$ Ω m and the frequency was $\omega = 2\pi \times 585$ kHz. From the above equations, $R_{c,DC} = 0.494$ m Ω , $\frac{R_{c,AC}}{R_{c,DC}} = 34.97$, and $R_{c,AC} = 17.3$ m Ω . In this work, $R_c = R_{c,AC} = 17.3$ m Ω is used for the coil resistance.

4.B Coil resistance calculation



Hybrid circuit–chemistry model

Hybrid circuit-chemistry model investigation of oxygen-argon ratio in inductive plasma thrusters

In the fourth article, a simple chemistry model is integrated with the circuit model to provide further insight and reduce assumptions. The chemistry model is a kinetics approach and could, in principle, be applied to any species for which reaction rates are known. Power series of pure oxygen and two oxygen-argon mixtures were considered. The additional of the chemistry model facilitates the calculation of the time-varying effective collision frequency and localised electron population.

Statement of authorship

Title Hybrid circuit-chemistry model investigation of oxygen-argon ratio in inductive plasma thrusters

Publication Submitted: Georg, R., Chadwick, A. R., Dally, B. B., & Herdrich, G. (2022b). Hybrid circuit-chemistry model investigation of oxygen-argon ratio in inductive plasma thrusters. *IEEE Transactions on Plasma Science* (manuscript TPS14940 submitted 25/5/2022)

Principal author contribution

This paper reports on original research I conducted during the period of my Higher Degree by Research candidature and is not subject to any obligations or contractual agreements with a third party that would constrain its inclusion in this thesis. I am the primary author of this paper.

Principal author R. Georg

Contribution I contributed approximately 80 % to the authorship of this paper. Excluding the experimental component, I was primarily responsible for the conception of the paper. I drafted the manuscript including all tables and figures. I conducted the majority of the analysis. I acted as the corresponding author.

My contribution satisfies all authorship criteria of the *Australian Code for the Responsible Conduct of Research*.

_____ 8 July 2022

Co-author contributions

By signing the statement of authorship, each co-author certifies that: i. the candidate's stated contribution to the publication is accurate (as detailed above); ii. permission is granted for the candidate to include the publication in the thesis; and iii. the sum of all co-author contributions is equal to 100 % less the candidate's stated contribution.

Co-author A. R. Chadwick

Contribution Collected the experimental data that is analysed in the paper. Provided knowledge and assisted with analysis and revising the manuscript. Involved in the conception of the paper, particularly the experimental component.

_____ 8 July 2022

Co-author B. B. Dally

Contribution Provided knowledge and assisted with analysis and revising the manuscript.

_____ 8 July 2022

Co-author G. Herdrich

Contribution Provided knowledge and assisted with analysis and revising the manuscript. Involved in the conception of the paper, particularly the experimental component.

_____ 8 July 2022

Abstract

Electrodeless, propellant-flexible electric propulsion based on inductively coupled plasmas has the potential to expand spaceflight capabilities. However, new diagnostic tools are needed, in particular, tools that are non-intrusive, real-time, propellant agnostic and have a high sampling frequency. A technique based on the circuit transformer model of inductive coupling and meeting these criteria was recently proposed and demonstrated. That technique is augmented in this work by the addition of a chemistry model via the BOLSIG+ software to generate a hybrid circuit-chemistry model. The hybrid model can compute the effective collision frequency and the electron density of mixed-species plasmas. The technique is applied to experimental datasets of pure oxygen and mixed oxygen-argon plasmas to investigate the influence of the argon component on the transient plasma properties and the thermal efficiency of the IPG7 thruster. The self-consistency and alignment of the results with previous work is confirmed. The addition of argon facilitates conditions in which longer (but less intense) periods of inductive coupling, and higher average electron populations occur. An empirical relationship between the transient behaviour of the plasma and the thermal efficiency is found, that may have important practical implications for future flight hardware.

5.1 Introduction

The development of electric propulsion technologies that can use a wide variety of propellants is sought because it would enable the use of propellant material collected in-flight, a concept known as in-situ resource utilisation (ISRU). For example, a satellite in very low Earth orbit may use an intake to collect material from the upper atmosphere as propellant, a concept known as air-breathing electric propulsion (ABEP). To realise that aim, several groups worldwide are investigating the application of electrodeless technologies, especially inductively coupled plasmas, as a means of delivering electric power to an arbitrary propellant (Romano et al., 2020; Sou et al., 2000; Herdrich et al., 2013; Isayama et al., 2018; Navarro-Cavallé et al., 2018; Vitucci, 2019; Magarotto & Pavarin, 2020; Takahashi, 2019; Tsifakis et al., 2020; Kralkina et al., 2020). Recently, propellant mixtures have shown great promise. In particular, mixtures of oxygen and argon have demonstrated high thermal efficiencies, combining the higher thermal conductivity and lower ionisation energy of the two gases, respectively (Georg et al., 2021 (chapter 3)). With the increased interest in different propellants and propellant mixtures, there has been a parallel interest in suitable diagnostic tools.

Phase-resolved optical emission spectroscopy (PROES) is a powerful diagnostic tool that provides a high spatial and temporal resolution by identifying the distinctive emission spectra of species present in the plasma Schulze et al., 2010. The tool relies on

optical measurements and a sufficiently detailed plasma chemistry and radiative model. A key issue in the application of PROES is the selection of frequency bands whose intensity can be uniquely attributed to each of the species in the plasma. Hence, most studies focus on pure argon which is monatomic and has a well-documented chemistry. The current research literature on PROES applied to gas mixtures is extremely limited. Kaupe et al. (2019) considered argon mixed with up to 4 % nitrogen and Liu et al. (2020) considered argon mixed with up to 1 % CO₂ and 1 % CH₄. By contrast, propellants of interest for high-power inductive electric propulsion include oxygen, nitrogen and carbon dioxide with an argon component ranging from 0 to 79 % (Chadwick et al., 2020). Furthermore, PROES is not readily adaptable for use in-flight since it requires optical access and high computational resources.

Recently, a technique based on a simple circuit model treating the antenna-plasma interaction as an electrical transformer was presented and used to estimate the time-varying properties of an inductively coupled plasma (Georg et al., 2022 (chapter 4)). This technique has the following attributes: non-intrusive—to avoid disrupting system operation and to limit erosion of electrical components; real-time—enabling use in monitoring and control; propellant agnostic—enabling flexibility of propellant choice, including mixtures; and capable of a high sampling frequency—to capture transient phenomena (Georg et al., 2022 (chapter 4)). The technique uses measurements of the antenna current and the circuit model to estimate the impedance of the antenna-plasma system, and subsequently several time-varying plasma properties.

In the present work, three key limitations of the circuit model are addressed. Firstly, neither the electron density nor the effective collision frequency could be extracted from the model, only the ratio between those two quantities. Secondly, therefore, it was not possible to verify the electron density against other results nor verify the self-consistency of the collision frequency. Thirdly, while the technique was propellant agnostic, it lacked the ability to provide insight into differences between propellants. These three limitations are addressed by coupling the circuit model with a simple chemistry model. The resulting hybrid model is then used to analyse pure oxygen and oxygen-argon plasmas.

5.2 Methodology

The device under consideration in this work is IPG7 (Massuti-Ballester et al., 2013; Chadwick et al., 2020), an inductively coupled plasma source developed at the Institute for Space Systems (IRS) of the University of Stuttgart, Germany. A sectional view of IPG7 is shown in figure 5.1. A pair of mass flow controllers is used to control the flow rate of each propellant gas before they are fed into an injector head. The injector head induces swirl into the propellant, which then passes through a quartz tube with a

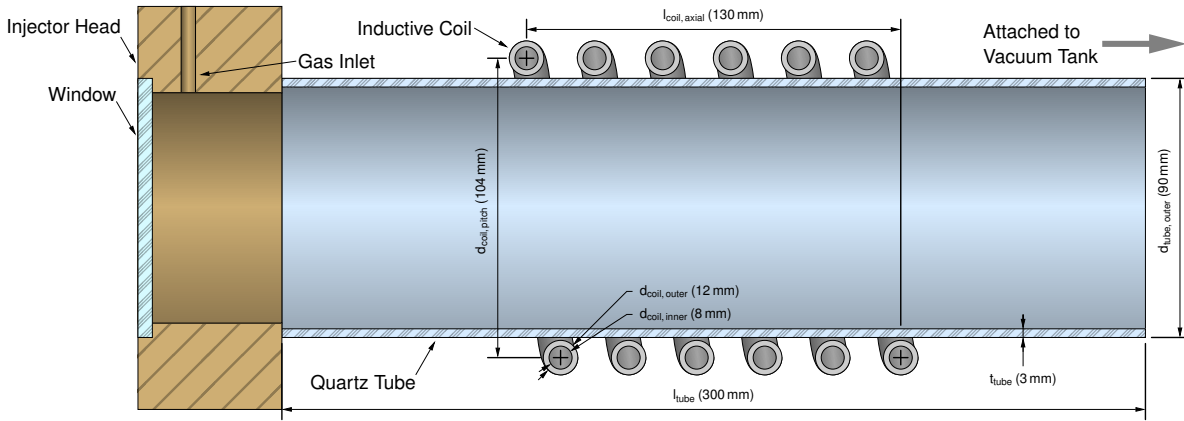


Figure 5.1: Sectional view of IPG7 with dimensions (adapted from Georg et al. (2020) (chapter 2)). A jacket encloses the coil, forming channels for cooling water (not shown).

length of 300 mm, an outer diameter of 90 mm and a thickness of 3 mm. Surrounding the quartz tube is a 5.5-turn helical coil with an axial length of 130 mm, a pitch diameter 104 mm, an outer diameter of 12 mm and an inner diameter of 8 mm. Radiofrequency current is driven through the coil such that it acts as an antenna and, under the right conditions, couples inductively with the plasma formed by the propellant gas. Propellant exits the quartz tube through a flange, into a vacuum tank with a length of 3 m and a diameter of 2 m. The tank pressure is approximately 10 to 30 Pa during operation.

The antenna current is driven by a resonant circuit, shown in figure 5.2 (left), known as a Meissner or Armstrong oscillator, without matching network. The resonant circuit itself is driven by a quasi-DC source (anode) that has a characteristic 300 Hz frequency. This arrangement means that the excitation frequency is floating and takes on the resonant frequency of the circuit, which is a function of the inductance of the antenna and the capacitance of the capacitor bank. The circuit model quantitatively links fluctuations in the excitation frequency to fluctuations in the impedance of the antenna-plasma system that occur during inductive coupling (Georg et al., 2022 (chapter 4)).

A simplified overview of the hybrid circuit–chemistry model showing inputs and outputs is included in figure 5.3. The first part, the circuit model, is described in the following subsection. The integration of the second part, the chemistry model BOLSIG+, is described in the subsequent section. Finally, the experimental setup is described.

5.2.1 Circuit model

A full derivation of the circuit model is provided in Georg et al. (2022) (chapter 4), the results of which are summarised here. The antenna-plasma system is modelled as an electrical transformer in the circuit shown in figure 5.2 (left), where the primary winding of the transformer is the 5.5-turn helical coil with self-inductance L_c , the sec-

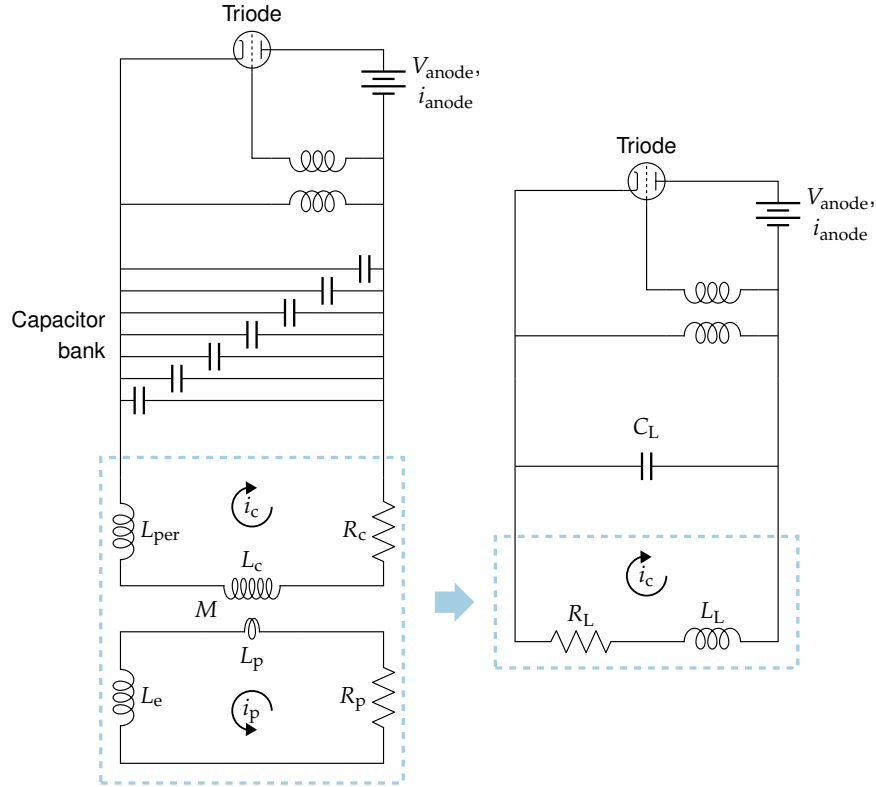


Figure 5.2: Resonant circuit with transformer model of the coil/plasma system (left) and lumped element equivalent circuit (right). Reproduced from Georg et al. (2022) (chapter 4).

ondary winding of the transformer is a single loop plasma current with self-inductance L_p , and there is a mutual inductance M . On the primary side, the coil has a resistance R_c and the circuit has a peripheral inductance L_{per} . On the secondary side, there is a plasma resistance R_p associated with absorbed power and an electron inductance L_e associated with the electron inertia.

The circuit can be reduced to the lumped element equivalent circuit shown in figure 5.2 (right). The lumped capacitance C_L has a fixed value determined by the capacitor configuration. The lumped resistance is given by

$$R_L = R_c + R_{p,\text{eff}}, \quad (5.45)$$

where $R_{p,\text{eff}}$ is the effective plasma resistance (non-zero during periods of inductive coupling). Similarly, the lumped inductance is given by

$$L_L = L_c + L_{\text{per}} - L_{p,\text{eff}}, \quad (5.46)$$

where $L_{p,\text{eff}}$ is the effective plasma inductance (non-zero during periods of inductive coupling).

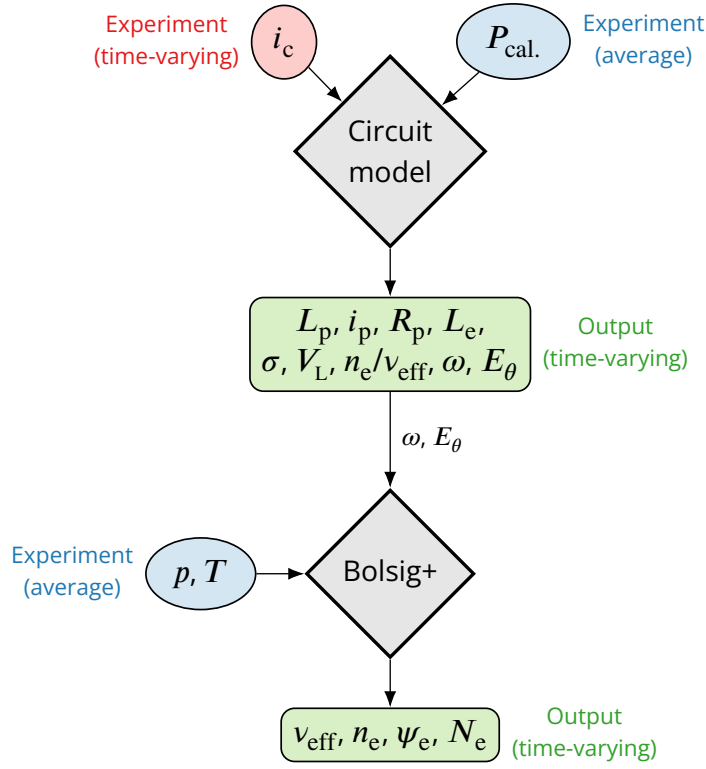


Figure 5.3: Simplified overview of the model. The following representations are used: red ellipse—time-varying experimental data, blue ellipses—time-averaged experimental data, grey diamonds—models, and green rectangles—model outputs (time-varying).

It is shown in Georg et al. (2022) (chapter 4) that, under the assumption of a collisional regime ($\nu_{\text{eff}} \gg \omega$), the effective plasma resistance becomes

$$R_{p,\text{eff}} = \frac{M^2 \omega \delta^*}{L_p((\delta^*)^2 + 1)}, \quad (5.47)$$

and the effective plasma inductance becomes

$$L_{p,\text{eff}} = \frac{M^2}{L_p((\delta^*)^2 + 1)}. \quad (5.48)$$

The mutual inductance between the coil and the plasma, M , has a fixed value determined by geometry. The plasma self-inductance, L_p , varies as a function of the axial length of the plasma discharge volume, l_p . The normalised skin depth, δ^* , varies as a function of the ratio between the electron number density and the collision frequency, n_e/ν_{eff} .

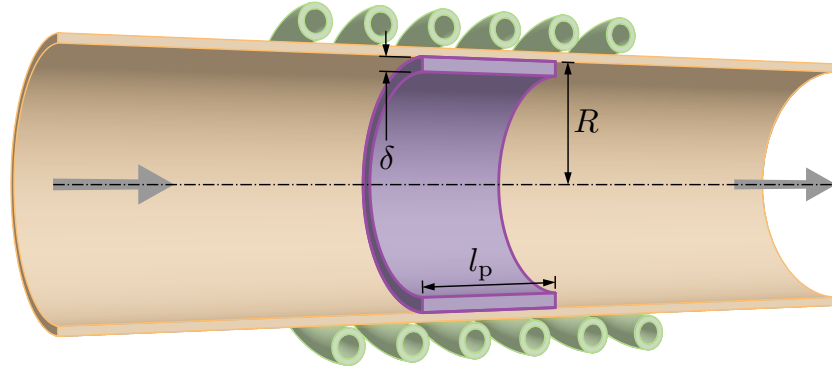


Figure 5.4: Sectional view of IPG7 showing the plasma volume representation. From outside to inside: the 5.5 turn helical coil, the discharge chamber tube, and the plasma volume. The plasma volume is a tube with outer radius R , thickness δ and axial length l_p . $V = l_p \pi(R^2 - (R - \delta)^2)$.

The equivalent circuit is an LC tank with a resonant frequency of

$$\omega = (L_L C_L)^{-\frac{1}{2}}, \quad (5.49)$$

that varies as a function of $L_{p,\text{eff}}$ during periods of inductive coupling. The inductive resonant frequency can be normalised by the non-inductive resonant frequency to yield

$$\begin{aligned} \omega^* &= \frac{((L_c + L_{\text{per}} - L_{p,\text{eff}}) C_L)^{-\frac{1}{2}}}{((L_c + L_{\text{per}}) C_L)^{-\frac{1}{2}}} \\ &= \left(1 - \frac{L_{p,\text{eff}}}{L_c + L_{\text{per}}}\right)^{-\frac{1}{2}}. \end{aligned} \quad (5.50)$$

The time-varying normalised frequency, $\omega^*(t)$, is determined experimentally by applying a short-time Fourier transform to coil current measurements. The time-varying effective plasma resistance, $R_{p,\text{eff}}(t)$, could be determined experimentally via simultaneous measurement of the potential across the coil. For technical reasons these measurements were not possible, hence $R_{p,\text{eff}}(t)$ was determined experimentally by reconciling coil current measurements with calorimetric powers. Using this, one may solve the above system of equations and determine the time-varying plasma volume axial length, $l_p(t)$, and the time-varying plasma volume thickness (skin depth), $\delta(t)$, which together define the plasma volume itself as per figure 5.4. Other time-varying outputs from the model include the plasma electrical conductivity σ , the azimuthal electric field strength E_θ and n_e/v_{eff} .

5.2.2 Chemistry model

A chemistry model was introduced primarily to extract the electron number density, n_e , and the effective collision frequency, ν_{eff} , from the ratio produced by the circuit model. The BOLSIG+ software (Hagelaar & Pitchford, 2005) was selected due to its simplicity, limited assumptions and prevalence in literature. BOLSIG+ is a numerical solver that computes steady-state solutions to the Boltzmann equation for electrons in a uniform electric field. Among other assumptions, it is necessary to assume a uniform electric field and constant properties with respect to space and time. While the system considered here is of course time-varying, these assumptions for the chemistry are nonetheless consistent with the extant assumptions of the circuit model and are appropriate for a tool that can be described as an engineering model. Details about the software inputs and outputs are provided in section 5.A. Cross-sections were retrieved from the Phelps database hosted on the LXCat website (Phelps, 2013). The oxygen cross-sections come from Lawton and Phelps (1978) and the argon cross-sections from Yamabe et al. (1983).

The critical inputs for BOLSIG+ are the electric field strength and the angular frequency. The relevant electric field is the azimuthal field induced during inductive coupling, E_θ . From Georg et al. (2022) (chapter 4), under a collisional assumption, the azimuthal electric field strength is given by

$$E_\theta = \frac{i_p \omega}{l_p} \left(\frac{\nu_{\text{eff}}^*}{n} \frac{\mu_0 m}{2 e^2} \right)^{\frac{1}{2}}, \quad (5.51)$$

which can be computed from the circuit model. Under the presence of $E \times B$ fields, as is the case here, the relevant angular frequency for BOLSIG+ is the cyclotron frequency, given by

$$\omega_c = \mu_0 H_z \frac{e}{m} \quad (5.52)$$

for zero magnetisation, where H_z is axial the magnetic field strength due to the coil. In a previous work (Georg et al., 2020 (chapter 2)) the method provided by Derby and Olbert (2010) yielded $H_z/i_c = 33.04 \text{ m}^{-1}$ at the centre of the coil (the variation within the volume bounded by the coil is minimal). Hence, this value can be used to compute the cyclotron frequency as a function of the coil current.

Paremetric sweeps of the azimuthal electric field strength and the cyclotron frequency were computed with the BOLSIG+ software version “11/2019”. This was used to build a look-up table to determine time-varying outputs such as $\nu_{\text{eff}}(t)$ from the time-varying inputs $\omega_c(t)$ and $E_\theta(t)$. Knowing $\nu_{\text{eff}}(t)$ permits the calculation of the localised electron fraction $\psi_e(t)$, electron number density $n_e(t)$, and number of electrons $N_e(t)$, which completes the process shown in figure 5.3.

5.2.3 Experimental setup










Experiments were conducted on the IPG7 device within the TIHTUS facility at the University of Stuttgart. The selection of gases and their respective flow rates defines the propellant configuration. For each experimental run, the propellant configuration is fixed and the anode potential is adjusted by the experimenter. The anode potential, shown as V_{anode} in figure 5.2, is a characteristic of the quasi-DC power supply and can be used as a proxy for the input power. After the anode potential is adjusted and before capturing data, the input and output powers of the system are allowed to stabilise at the new condition.

The primary measurement required for the following analysis is the coil current. Measurements were taken using a Hofer-Noser Karrer (HOKA) probe designed by Kametech AG (Karrer et al., 1999; Karrer et al., 2003). The probe was specially designed and selected to tolerate prolonged exposure to the high current and to support high sampling frequencies. The coil current was sampled at a frequency of 25 MHz, which is sufficient to determine the characteristic frequency of the current, $f_{\text{char}}(t)$, via short-time Fourier transform analysis. A moving-window rms calculation was used to determine the rms coil current, $i_c(t)$.

Closed loops of cooling water are used, together with flow meters and thermometers, to measure calorimetric powers. The tube cooling power, P_{tube} , is derived from a loop that directly contacts the quartz tube. The jet cooling power, P_{jet} , is derived from a loop that passes through a cavity calorimeter that can be inserted into the vacuum tank to determine the enthalpy of the plasma jet. The sum of the calorimetric powers, P_{cal} , is a model input in the present work. For a truly non-intrusive experimental setup (such as in flight), the phase-resolved potential across the coil could substitute this role. An important figure of merit for the system is the thermal efficiency, defined as $\eta_{\text{thermal}} = P_{\text{jet}}/P_{\text{cal}}$. It represents the portion of power dissipated by the antenna-plasma system that is available to develop thrust via gas-dynamic expansion of the jet through a nozzle.

Temperature and pressure inside the hot zone must be estimated for the chemistry component of the model. Interpolation of previous IPG characterisation results (Herdrich, 2004) for the conditions under consideration provides an approximate pressure of 1500 Pa and temperature of 10,000 K in the hot zone. Order of magnitude accuracy is sufficient for the present work since the BOLSIG+ inputs and outputs are normalised by the neutral gas density.

Table 5.1: Summary of experimental conditions (collected by Chadwick (2017)). Mean values are given, with the exception of root-mean-square for i_c and f_{char} , and median for v_{eff}^* . Species fractions are volumetric. Volumetric flow rate \dot{V} is for standard conditions 0 °C and 1 atm. The thermal efficiency is defined as $\eta_{thermal} = P_{jet}/P_{cal.}$, where P_{jet} is the jet power and $P_{cal.} = P_{jet} + P_{tube}$ is the sum of calorimetric powers.

Legend	Propellant				Anode		Coil		Calorimetry		Group	Outputs		
	O ₂ %	Ar %	\dot{V} L/min	\dot{m} g/s	U_{anode} kV	P_{anode} kW	i_c kA	f_{char} kHz	$P_{cal.}$ kW	$\eta_{thermal}$ %		v_{eff}^* —	ψ_e %	V cm ³
	100	0	142	3.38	4.3	25.3	0.84	586	7.9	23.2	A	158	1.9	2.2
	5.0	38.2	0.85	589	11.0	30.8	B	155	2.6	5.0
	5.5	49.6	0.89	591	13.4	35.5	B	153	3.2	5.7
	42	58	128	3.49	3.6	16.9	0.71	587	5.7	23.6	A	122	1.6	2.3
	4.0	25.0	0.67	592	7.2	34.7	B	124	2.3	6.1
	4.4	44.2	0.55	600	12.7	74.7	C	118	3.8	11.1
	32	68	134	3.74	3.6	25.4	0.71	587	4.2	16.6	A	116	1.7	1.8
	4.0	35.9	0.50	599	10.6	75.7	C	114	3.0	11.6
	5.0	66.8	0.55	608	16.5	80.0	C	110	5.5	14.0

5.3 Results & discussion

The results presented in this section are based on experimental data collected by Chadwick (2017) and processed as described in the previous section. The data are summarised in table 5.1. Three propellant configurations are considered: pure oxygen at 142 L/min, 42 % oxygen and 58 % argon at 128 L/min, and 32 % oxygen and 68 % argon at 134 L/min. There are three anode potential (input power) levels for each propellant configuration, starting with the lowest anode potential that achieves inductive coupling and increasing incrementally. These data were selected to investigate the effect of augmenting oxygen with argon, as this has been found to have implications for propulsion (Chadwick, 2017; Chadwick et al., 2020; Georg et al., 2021 (chapter 3)), as well as demonstrating the propellant-flexible nature of the presented model. The results are presented in figures 5.5 to 5.9 and 5.11 as time-series at the time-scale of the 300 Hz cycle and show respectively: the coil current, the normalised frequency shift, the normalised effective collision frequency, the electron fraction, the plasma volume, and the number of electrons.

Of particular interest are those conditions that lead to high thermal efficiencies. The nine conditions under consideration can be grouped by their thermal efficiencies, such

5 Hybrid circuit–chemistry model

that group A has 23.2 %, 23.6 % and 16.6 %, group B has 30.8 %, 35.5 % and 34.7 %, and group C has 74.7 %, 75.7 % and 80.0 %. Group A consists of the lowest power conditions for each propellant configuration (◉, ◊, ◑). Group B consists of 5.0 kV and 5.5 kV at 100 % oxygen, and 4.0 kV at 42 % oxygen (◀, △, ▽). Group C consists of 4.4 kV at 42 % oxygen, and 4.0 kV and 5.0 kV at 32 % oxygen (★, ▶, ✱). The utility and significance of these groups will become apparent as the results are presented and discussed.

The primary model inputs—coil current and normalised frequency shift—are shown in figure 5.5 and figure 5.6 respectively. In low power conditions, associated with purely capacitive coupling, the coil current resembles a skewed Gaussian distribution (reference curve in figure 5.5). Periods during which the current follows the reference distribution are associated with capacitive coupling, while periods during which it deviates from the reference distribution are associated with inductive coupling. Hence, the capacitive-inductive transition is marked by the initial maxima occurring between 0.4 ms and 1.3 ms. The inductive-capacitive transition cannot be precisely determined from visual inspection of the coil current curve. Considering the trend of group A to B to C, the current deviation increases in magnitude and duration as the thermal efficiency increases.

By definition, the normalised frequency shift is equal to one during periods of purely capacitive coupling. Therefore, the periods of inductive coupling correspond to the periods when $\omega^* > 1$. The transitions between capacitive and inductive coupling are identified in figure 5.6 with markers, and occur at approximately the same times as the transitions seen in the coil current. Because the circuit model has an underlying assumption of significant inductive coupling, it is only valid during the periods when $\omega^* > 1$, and hence the model outputs are only defined during those periods.

The three groups are clearly distinguishable in the curves of normalised frequency shift shown in figure 5.6. Group A consists of the three curves with the shortest periods and smallest peak magnitudes (◉, ◊, ◑). Group B consists of the three curves with intermediate periods (◀, △, ▽). Group C consists of the three curves with the longest periods (★, ▶, ✱). In general, the width of the curve, and the area under the curve, increase both as the anode potential (input power) increases and the percentage argon increases. The percentage argon has more influence than the anode potential, since, for example, 5.5 kV at 100 % oxygen (△) is much narrower than 5.0 kV at 32 % oxygen (✱). Further analysis of the normalised frequency shift was carried out in a prior work (Georg et al., 2021 (chapter 3)), which showed a strong link between the frequency shift and the thermal efficiency. That link is evidenced here by the fact that the thermal efficiency groupings are so clearly visible in the frequency shift curves.

The effective collision frequency is the primary output of the chemistry model, and is

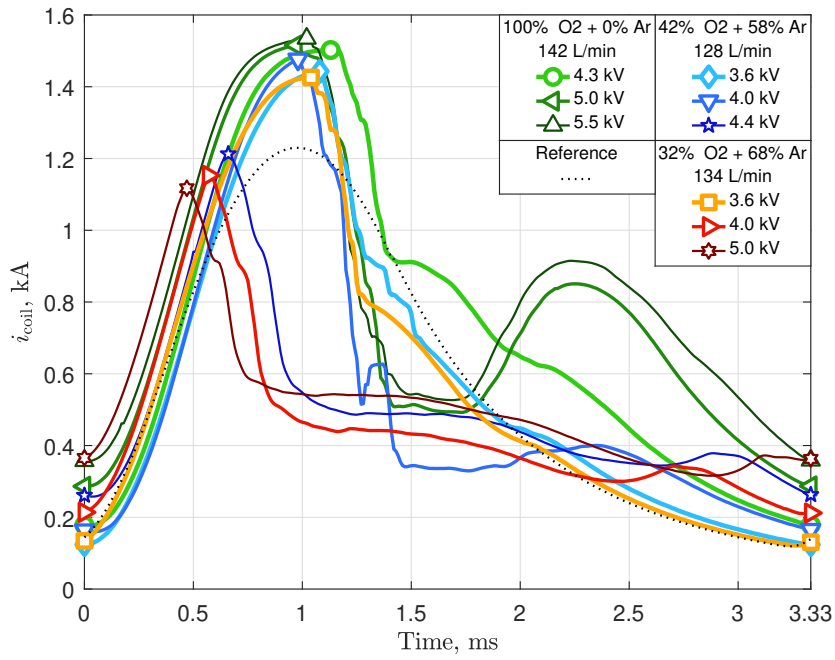


Figure 5.5: Time series of coil current. The initial, maximum and final points are identified with markers. A reference curve is included that shows the typical coil current under a low-power condition with purely capacitive coupling.

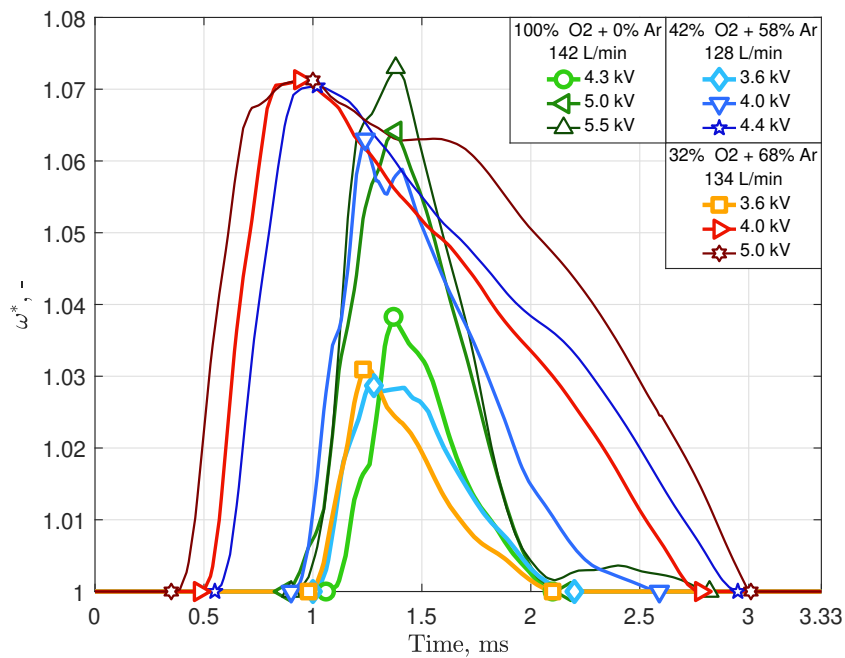


Figure 5.6: Time series of normalised frequency shift. The initial, maximum and final points of the period of inductive coupling ($\omega^* > 1$) are identified with markers.

5 Hybrid circuit–chemistry model

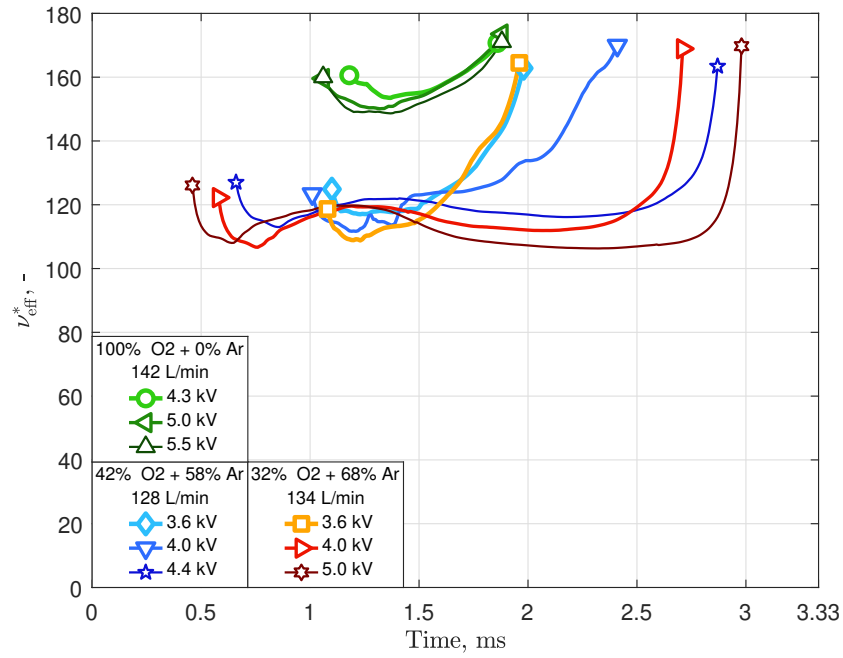


Figure 5.7: Time series of normalised effective collision frequency. The initial and final points are identified with markers.

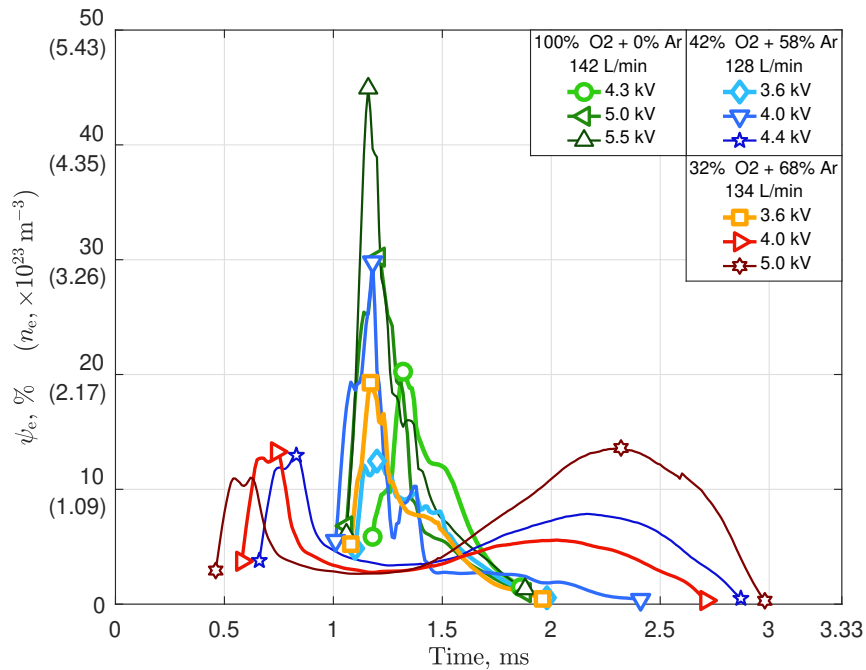


Figure 5.8: Time series of localised electron fraction (and electron number density). The initial, maximum and final points are identified with markers.

shown in figure 5.7 normalised by the excitation frequency, that is $\nu_{\text{eff}}^* = \nu_{\text{eff}}/\omega$. The beginning and end of each curve asymptotes upwards due to the breakdown of the model assumptions at those times. However, the middle part of each curve is relatively stable. Therefore, the typical value for each curve is best characterised by the median, which is tabulated in table 5.1. These values are strongly influenced by the argon fraction of the gas mixture, moreso than the input power, which appears to have little effect. Averaging the values for each gas mixture, the typical normalised effective collision frequency for pure oxygen is 155, for 58 % argon it is 121, and for 68 % argon it is 113. A key assumption used in the present work is that of a collisional regime, defined as $\nu_{\text{eff}} \gg \omega$. This assumption appears in the definition used for the skin depth, as well as several algebraic simplifications (Georg et al., 2022 (chapter 4)). Since ν_{eff} is at least two orders of magnitude larger than ω , this aspect of the model is self-consistent and supports its validity.

Knowledge of ν_{eff}^* allows the calculation of localised electron density both as a fraction and as a number density, both shown in figure 5.8. These quantities concern the localised plasma volume (hot zone), shown in figure 5.9 and discussed later. The electron fraction is defined here as the ratio of the electron number density to the upstream neutral gas density, this is, $\psi_e = n_e/n_g$. Considering the shapes of the curves, group A and B curves have a single, high-magnitude peak and group C curves have two peaks and a much flatter distribution. For the single peak curves, the maxima increase with anode potential and argon percentage, ranging from 12.5 to 44.9 %. For the double peak curves, the peaks range from 5.6 to 13.6 %. The means of ψ_e are tabulated in table 5.1.

Previous experimental work on IPG3, a sister-device to IPG7, captured an operating condition with input conditions of $V_{\text{anode}} = 6.3$ kV, $P_{\text{anode}} = 107$ kW and 128 L min⁻¹ of pure oxygen (Herdrich, 2004). This condition was the subject of a numerical simulation that was spatially resolved, but used a steady state assumption with respect to the coil current. The results of this simulation showed a localised hot zone with an electron temperature of approximately 10,000 K and an electron fraction of approximately 20 %. The most similar condition considered in this work has input conditions of $V_{\text{anode}} = 5.5$ kV, $P_{\text{anode}} = 49.6$ kW and 142 L min⁻¹ of pure oxygen (↩). The electron fraction curve shown in figure 5.8 for this condition has a mean value of 3.2 % and a maximum value of 44.9 %. Taking into consideration the discrepancies in modelling approaches and assumptions, as well as the different input conditions, most notably the different experimental devices and anode powers, a relatively good agreement between the electron fractions is shown.

Time series of the plasma volume are shown in figure 5.9. With respect to the circuit model, the plasma is modelled as a tubular volume (see figure 5.4) with uniform properties. The outer radius R is equal to the discharge chamber inner radius (constant), the thickness is equal to the skin depth δ (time-varying) and the axial length is

5 Hybrid circuit–chemistry model

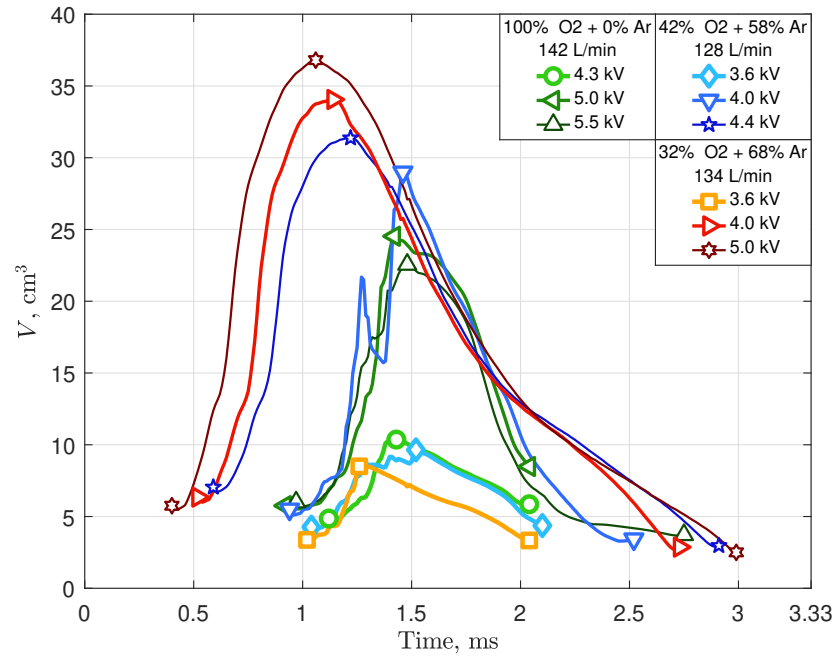


Figure 5.9: Time series of plasma volume. The initial, maximum and final points are identified with markers.

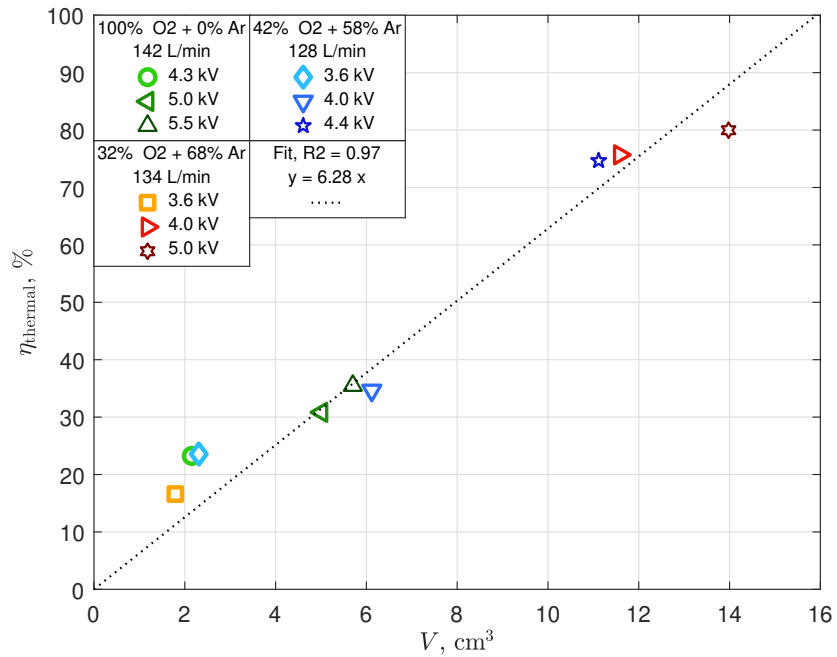


Figure 5.10: Average thermal efficiency against average plasma volume for each condition. A proportional relationship is fitted such that $\eta_{\text{thermal}} = 6.28 V$ with $R^2 = 0.97$.

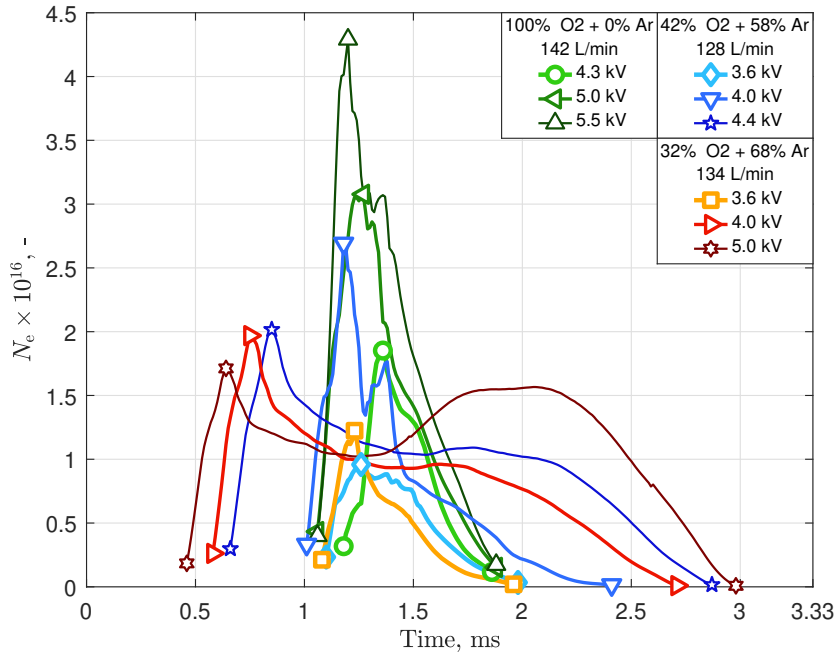


Figure 5.11: Time series of number of electrons. The initial, maximum and final points are identified with markers.

equal to l_p (time-varying). Hence, the volume is a time-varying quantity defined as $V = l_p \pi(R^2 - (R - \delta)^2)$. The groupings by thermal efficiency are clearly visible in this data. Group A peaks around 10 cm^3 , group B around 25 cm^3 , and group C around 35 cm^3 .

Plotting the average thermal efficiency against the average plasma volume for each condition, as in figure 5.10, reveals a strong correlation between the two quantities. The average plasma volume is expected to play an important role with respect to the thermal efficiency, as heating that is highly localised (in time and space) is likely to produce a high rate of heat transfer through the chamber wall (wasted heat). The fitted proportional relationship, $\eta_{\text{thermal}} = 6.28 V$, has an R^2 value of 0.97. The strength of this relationship is particularly notable since the thermal efficiency is a ‘macroscopic’ system property that was measured at a low sampling frequency, while the plasma volume is a ‘microscopic’ system property that comes from the circuit model interpretation of coil current measured at a high sampling frequency. The relationship also holds under differing fractions of argon. Experimental measurement of the thermal efficiency requires a cavity calorimeter that cannot be used in flight; alternatively, the relationship established here could, in principle, be used to estimate the thermal efficiency from coil current measurements in flight, in real-time.

Finally, one may multiply the electron number density with the plasma volume to

arrive at the number of electrons, N_e , which is plotted in figure 5.11. As with the number density shown in figure 5.8, groups A and B exhibit a single, high-magnitude peak and group C curves have two peaks and a much flatter distribution. In the case of group C, the valleys of n_e coincide with the peaks of V , resulting in flatter curves for N_e . The distinguishing feature of group C conditions (high thermal efficiency) may be a long-lived electron population that has sufficient time to transfer heat to heavy particles via collisions.

5.4 Conclusion

In the present work, a circuit model for interpreting time-varying plasma properties from antenna current measurements was augmented with a simple chemistry model using the BOLSIG+ software. The resulting hybrid circuit-chemistry model was used to analyse oxygen and oxygen-argon plasmas at various input powers. The results were shown to be self-consistent and in-line with previous work. The results show a clear distinction between the transient plasma properties of conditions that generate a high thermal efficiency, and those that do not, hence building an understanding of the internal processes that lead to desirable propulsion figures of merit. In particular, the thermal efficiency shows a strong correlation with time averaged plasma volume. It may be possible in a future work to robustly demonstrate the prediction of thermal efficiency from purely non-intrusive measurements; this would be a useful characterisation for in-flight operation. The relative simplicity of the hybrid circuit-chemistry model depicted in this work leads to a low fidelity of results in comparison to techniques such as optical emission spectroscopy. Nonetheless, this simplicity comes with limited required input data and a high degree of flexibility of its application. Further validation of this approach may lead to a diagnostic tool that is non-intrusive, is highly flexible with respect to propellant, and provides insight into transient phenomena and how they affect thruster performance.

Acknowledgements

The authors would like to thank Dr Ramses Snoeckx of King Abdullah University of Science and Technology for productive conversations related to the chemistry model.

The authors would also like to thank the German Research Foundation for their financial contributions to the experimental campaign under Project HE 4563/3-1.

This research is supported by an Australian Government Research Training Program (RTP) Scholarship.

Research undertaken for this report has been assisted with a grant from the Sir Ross and Sir Keith Smith Fund (Smith Fund) (www.smithfund.org.au). The support is acknowledged and greatly appreciated. The Smith Fund, by providing funding for this project, does not verify the accuracy of any findings or any representations contained in it. Any reliance on the findings in any written report or information provided to you should be based solely on your own assessment and conclusions. The Smith Fund does not accept any responsibility or liability from any person, company or entity that may have relied on any written report or representations contained in this report if that person, company or entity suffers any loss (financial or otherwise) as a result.

References

- Chadwick, A. R. (2017). *Performance of Alternative Propellants in an Inductive Electric Propulsion System* (Ph.D. Thesis). The University of Adelaide. <http://hdl.handle.net/2440/119192>
- Chadwick, A. R., Dally, B. B., Herdrich, G., & Kim, M. (2020). High-power inductive electric propulsion operation with alternative propellants. *The Aeronautical Journal*, 124(1272), 151–169. <https://doi.org/10.1017/aer.2019.141>
- Derby, N., & Olbert, S. (2010). Cylindrical Magnets and Ideal Solenoids. *American Journal of Physics*, 78(3), 229–235. <https://doi.org/10.1119/1.3256157>
- Georg, R., Chadwick, A. R., Dally, B. B., & Herdrich, G. (2020). Resolving transient discharge cycle behaviour in modulated inductive plasmas. *Vacuum*. <https://doi.org/10.1016/j.vacuum.2020.109636>
- Georg, R., Chadwick, A. R., Dally, B. B., & Herdrich, G. (2021). Power efficiency estimation of an inductive plasma generator using propellant mixtures of oxygen, carbon-dioxide and argon. *Acta Astronautica*, 179(November 2020), 536–545. <https://doi.org/10.1016/j.actaastro.2020.11.020>
- Georg, R., Chadwick, A. R., Dally, B. B., & Herdrich, G. (2022). Model for Estimating Time-Varying Properties of an Inductively Coupled Plasma. *IEEE Transactions on Plasma Science*. <https://doi.org/10.1109/TPS.2022.3166162>

- Hagelaar, G. J., & Pitchford, L. C. (2005). Solving the Boltzmann equation to obtain electron transport coefficients and rate coefficients for fluid models. *Plasma Sources Science and Technology*, 14(4), 722–733. <https://doi.org/10.1088/0963-0252/14/4/011>
- Herdrich, G. (2004). *Construction, qualification and characterisation of an inductively heated plasma wind-tunnel system to simulate atmospheric entry (Aufbau, Qualifikation und Charakterisierung einer induktiv beheizten Plasmawindkanalanlage zur Simulation atmosphärischer)* (Ph.D. Thesis). Universität Stuttgart.
- Herdrich, G., Bauder, U., Boxberger, A., Gabrielli, R. A., Lau, M., Petkow, D., Pfeiffer, M., Syring, C., & Fasoulas, S. (2013). Advanced plasma (propulsion) concepts at IRS. *Vacuum*, 88(1), 36–41. <https://doi.org/10.1016/j.vacuum.2012.02.032>
- Isayama, S., Shinohara, S., & Hada, T. (2018). Review of helicon high-density plasma: Production mechanism and plasma/wave characteristics. *Plasma and Fusion Research*, 13, 1–27. <https://doi.org/10.1585/PFR.13.1101014>
- Karrer, N., Hofer-Noser, P., Herdrich, G., & Auweter-Kurtz, M. (2003). Isolated current probe for continuous monitoring of AC currents of high amplitude and high frequency. *European Power Electronics Conference*.
- Karrer, N., Hofer-Noser, P., & Henrard, D. (1999). HOKA: a new isolated current measuring principle and its features. *Conference Record of the 1999 IEEE Industry Applications Conference. Thirty-Forth IAS Annual Meeting (Cat. No.99CH36370)*, 3, 2121–2128. <https://doi.org/10.1109/IAS.1999.806028>
- Kaupe, J., Riedl, P., Coenen, D., & Mitic, S. (2019). Temporal evolution of electron density and temperature in low pressure transient Ar/N₂ plasmas estimated by optical emission spectroscopy. *Plasma Sources Science and Technology*, 28(6). <https://doi.org/10.1088/1361-6595/ab252d>
- Kralkina, E. A., Nekliudova, P., Pavlov, V., Vavilin, K., Zadiriev, I., & Zhao, C. (2020). Experimental study of a low-pressure hybrid RF discharge. *Plasma Science and Technology*, 22(5), 055405. <https://doi.org/10.1088/2058-6272/ab69bd>
- Lawton, S. A., & Phelps, A. V. (1978). Excitation of the b 1 Σ +g state of O₂ by low energy electrons. *The Journal of Chemical Physics*, 69(3), 1055. <https://doi.org/10.1063/1.436700>
- Liu, Z., Huang, B., Zhu, W., Zhang, C., Tu, X., & Shao, T. (2020). Phase-Resolved Measurement of Atmospheric-Pressure Radio-Frequency Pulsed Discharges in Ar/CH₄/CO₂ Mixture. *Plasma Chemistry and Plasma Processing*, 40(4), 937–953. <https://doi.org/10.1007/s11090-020-10071-5>
- Magarotto, M., & Pavarin, D. (2020). Parametric Study of a Cathode-Less Radio Frequency Thruster. *IEEE Transactions on Plasma Science*, 48(8), 1–13. <https://doi.org/10.1109/TPS.2020.3006257>
- Massuti-Ballester, B., Marynowski, T., & Herdrich, G. (2013). New Inductively Heated Plasma Source IPG7. *Frontier of Applied Plasma Technology*, 6(2).

- Navarro-Cavallé, J., Wijnen, M., Fajardo, P., & Ahedo, E. (2018). Experimental characterization of a 1 kW Helicon Plasma Thruster. *Vacuum*, *149*, 69–73. <https://doi.org/10.1016/j.vacuum.2017.11.036>
- Phelps, A. V. (2013). Phelps database. Retrieved June 4, 2013, from www.lxcat.net
- Romano, F., Chan, Y.-A., Herdrich, G., Traub, C., Fasoulas, S., Roberts, P., Smith, K., Edmondson, S., Haigh, S., Crisp, N., Oiko, V., Worrall, S., Livadiotti, S., Huyton, C., Sinpetru, L., Straker, A., Becedas, J., Domínguez, R., González, D., ... Heißerer, B. (2020). RF Helicon-based Inductive Plasma Thruster (IPT) Design for an Atmosphere-Breathing Electric Propulsion system (ABEP). *Acta Astronautica*, *176*(January), 476–483. <https://doi.org/10.1016/j.actaastro.2020.07.008>
- Schulze, J., Schüngel, E., Donkó, Z., Luggenhölscher, D., & Czarnetzki, U. (2010). Phase resolved optical emission spectroscopy: A non-intrusive diagnostic to study electron dynamics in capacitive radio frequency discharges. *Journal of Physics D: Applied Physics*, *43*(12). <https://doi.org/10.1088/0022-3727/43/12/124016>
- Sou, H., Takao, Y., Noutsuka, T., Mori, Y., Uemura, K., & Nakashima, H. (2000). Study of plasma propulsion system with RF heating. *Vacuum*, *59*(1), 73–79. [https://doi.org/10.1016/S0042-207X\(00\)00256-6](https://doi.org/10.1016/S0042-207X(00)00256-6)
- Takahashi, K. (2019). Helicon-type radiofrequency plasma thrusters and magnetic plasma nozzles. *Reviews of Modern Plasma Physics*, *3*(1), 3. <https://doi.org/10.1007/s41614-019-0024-2>
- Tsifakis, D., Charles, C., & Boswell, R. (2020). An Inductively-Coupled Plasma Electrothermal Radiofrequency Thruster. *Frontiers in Physics*, *8*(February), 1–10. <https://doi.org/10.3389/fphy.2020.00034>
- Vitucci, J. J. (2019). *Development and test of a superconducting helicon plasma thruster* (Ph.D. Thesis). University of Maryland.
- Yamabe, C., Buckman, S. J., & Phelps, A. V. (1983). Measurement of free-free emission from low-energy-electron collisions with Ar. *Physical Review A*, *27*(3), 1345–1352. <https://doi.org/10.1103/PhysRevA.27.1345>

Appendices

5.A BOLSIG+ data

The following are excerpts from the results.dat file produced by BOLSIG+. The first part contains the input conditions, the second part contains the outputs and the third part contains the chemistry cross-section inputs.

```

1 BOLSIG+ version: 11/2019
2 Collision input data:
3 -----
4 Ar
5 SigloDataBase-LXCat-04Jun2013.txt
6 How to reference in publications:
7 1) Yamabe, Buckman, and Phelps, Phys. Rev. 27, 1345 (1983). Revised Oct 1997
8 2) PHELPS database,http://www.lxcat.laplace.univ-tlse.fr, retrieved June 4, 2013.
9 -----
10 O2
11 SigloDataBase-LXCat-04Jun2013.txt
12 How to reference in publications:
13 1) Lawton and Phelps, J. Chem. Phys. 69, 1055(1978).
14 2) PHELPS database, http://www.lxcat.laplace.univ-tlse.fr, retrieved June 4, 2013
15 NOTE:3 body attachment cross section are normalized to gas density in units of cm-3.
16
17
18
19 Conditions
20 A1 Electric field / N (Td)
21 A2 Angular frequency / N (m3/s)
22 A3 Cosine of E-B field angle 0.000
23 A4 Gas temperature (K)
24 A5 Excitation temperature (K)
25 A6 Transition energy (eV) 0.000
26 A7 Ionization degree 0.000
27 A8 Plasma density (1/m3) 0.1000E+19
28 A9 Ion charge parameter 1.000
29 A10 Ion/neutral mass ratio 1.000
30 A11 Coulomb collision model 3.000
31 A12 Energy sharing 1.000
32 A13 Growth model 1.000
33 A14 Maxwellian mean energy (eV) 0.000
34 A15 # of grid points 200.0
35 A16 Grid type 0.000
36 A17 Maximum energy 200.0
37 A18 Precision 0.1000E-09
38 A19 Convergence 0.1000E-03
39 A20 Maximum # of iterations 1000.
40 A21 Mole fraction Ar 0.6800
41 A22 Mole fraction O2 0.3200
42 R# A1 A2 A4 A5
43 1 0.9204E-01 0.1619E-13 0.1000E+05 0.1000E+05
44 2 3.373 0.1619E-13 0.1000E+05 0.1000E+05
...
645 Transport coefficients
646 A1 Mean energy (eV)
647 A2 Mobility *N (1/m/V/s)
648 A3 Re/perp mobility *N (1/m/V/s)

```

5.A BOLSIG+ data

```

649 A4    Im/Hall mobility *N (1/m/V/s)
650 A6    Diffusion coefficient *N (1/m/s)
651 A11   Energy mobility *N (1/m/V/s)
652 A12   Energy diffusion coef. *N (1/m/s)
653 A13   Total collision freq. /N (m3/s)
654 A14   Momentum frequency /N (m3/s)
655 A16   Total ionization freq. /N (m3/s)
656 A17   Total attachment freq. /N (m3/s)
657 A20   Power /N (eV m3/s)
658 A21   Elastic power loss /N (eV m3/s)
659 A22   Inelastic power loss /N (eV m3/s)
660 A23   Growth power /N (eV m3/s)
661 A27   Maximum energy
662 A28   # of iterations
663 A29   # of grid trials
664      R#    E/N (Td)      A1      A2      A3      A4      A6
          A11    A12      A13     A14     A16     A17     A20
          A21    A22      A23     A27     A28     A29
665      1  0.9204E-01  1.284    0.7710E+25  0.4059E+25 -0.2950E+25  0.6527E+25
          0.7927E+25  0.6790E+25  0.2235E-13  0.7268E-14  0.6759E-21  0.2485E-18
          0.3439E-19 -0.8516E-20  0.3610E-18 -0.3183E-18  20.70      5.000      1.000
666      2  3.373      1.868    0.4709E+25  0.3364E+25 -0.1661E+25  0.6737E+25
          0.5642E+25  0.6974E+25  0.3161E-13  0.5616E-14  0.1559E-20  0.5271E-18
          0.3827E-16  0.5481E-18  0.3869E-16 -0.9819E-18  24.47     10.00     2.000
...
1267 Rate coefficients (m3/s)
1268 C1    Ar    Effective (momentum)
1269 C2    Ar    Excitation    11.50 eV
1270 C3    Ar    Ionization    15.80 eV
1271 C4    O2    Attachment
1272 C5    O2    Attachment
1273 C6    O2    Effective (momentum)
1274 C7    O2    Excitation    0.020 eV
1275 C8    O2    Excitation    0.19 eV
1276 C9    O2    Excitation    0.19 eV
1277 C10   O2    Excitation    0.38 eV
1278 C11   O2    Excitation    0.38 eV
1279 C12   O2    Excitation    0.57 eV
1280 C13   O2    Excitation    0.75 eV
1281 C14   O2    Excitation    0.98 eV
1282 C15   O2    Excitation    1.63 eV
1283 C16   O2    Excitation    4.50 eV
1284 C17   O2    Excitation    6.00 eV
1285 C18   O2    Excitation    8.40 eV
1286 C19   O2    Excitation    9.97 eV
1287 C20   O2    Ionization    12.06 eV
1288      R#    E/N (Td) Energy (eV)      C1      C2      C3      C4
          C5      C6      C7      C8      C9      C10     C11
          C12     C13     C14     C15     C16     C17
1289      1  0.9204E-01  1.284    0.1422E-13  0.7980E-20  0.1081E-21  0.6205E-36
          0.7766E-18  0.3963E-13  0.2487E-16  0.2720E-15  0.1587E-16  0.8701E-16
          0.7929E-17  0.2284E-16  0.6440E-17  0.9012E-16  0.1952E-16  0.6228E-17
          0.5027E-17  0.2377E-17  0.8407E-21  0.1882E-20
1290      2  3.373      1.868    0.2381E-13  0.1876E-19  0.2212E-21  0.3207E-36
          0.1647E-17  0.4818E-13  0.1833E-16  0.1726E-15  0.3709E-16  0.6274E-16
          0.1922E-16  0.2128E-16  0.6925E-17  0.1874E-15  0.4350E-16  0.1350E-16
          0.8632E-17  0.3568E-17  0.1788E-20  0.4400E-20
...
1889 End of file

```



Summary and conclusion

The overall aim of this thesis was the investigation of transient antenna-plasma interactions within an inductive plasma thruster. This was achieved, firstly, by confirming the existence of significant transient phenomena linked to coupling mode transitions in chapter 2. Secondly, the coupling mode transition behaviour was quantified and shown to affect the thruster's thermal efficiency in chapter 3. Thirdly, the behaviour was explained in terms of a circuit that linked the time-varying antenna current with the time-varying plasma impedance in chapter 4. Fourthly, a chemistry component was added to the circuit model to gain further insight into the influence of propellant choice in chapter 5.

It was shown conclusively that the observed transient antenna current behaviour is linked to mode transitions occurring periodically at 300 Hz. These mode transitions can be tracked precisely through antenna current observations and were confirmed by simultaneous visible emission observations. This violates the steady state approximation that is typically used when studying inductive plasma sources and supports the necessity of transient analysis.

The antenna current behaviour was quantified by the definition of the 'inductive duty cycle' and the 'inductive frequency shift'. The latter in particular was demonstrated to be strongly related to the input power and associated with a third, high thermal efficiency mode. This showed that these transient phenomena are linked to the propulsive performance of the thruster.

A theoretical explanation of the transient phenomena was provided in the form of a circuit model that links the antenna current behaviour to the plasma impedance. The model was built on the transformer model of inductive coupling and exploits the changing antenna current frequency to determine the plasma impedance. This not only explains the mechanism behind the transient phenomena but also provides the basis for a new diagnostic tool.

The link between the time-varying antenna current and exciting frequency was exploited to generate a new non-intrusive diagnostic tool. Besides being non-intrusive, the tool is also propellant agnostic and capable of being implemented in real time and resolving transient effects. With the addition of a simple chemistry model, the tool can

also provide insight into the influence of propellant composition.

The combination of the four studies presented in this thesis represents a significant dataset and body of knowledge related to the transient behaviour of inductive plasma thrusters. An overview of the conditions considered is provided in table 6.1. The developed diagnostic tool and dataset together provoke a number of possible avenues for future work, four of which are described as follows.

6.1 Future work

Firstly, the validation level of the model could be significantly increased by additional experimental work. In particular, this could mean Langmuir probe measurements and/or the application of phase-resolved optical emission spectroscopy (PROES). The latter can provide a more forthright point of comparison since it is also non-intrusive in nature. However, it would only be applicable to a limited number of propellants. On the other hand, Langmuir probe measurements can be made with a minimal number of assumptions, hence they may provide a stronger validation. Induced plasma current and electron number density are important quantities to verify.

Secondly, the chemistry model could be extended to output species populations. This is in principle possible with limited alterations, however, it would require significant validation as per the previous point. It is conceivable that this could be used alongside PROES to provide powerful diagnostics, although this would limit certain aspects of the hybrid model, such as propellant-flexibility.

Thirdly, access to simultaneous measurements of the potential across the antenna would reduce the uncertainty of the circuit model. For technical reasons, these measurements could not be made in the present work. This led to the use of assumptions concerning the power supply behaviour in order to estimate the time-varying plasma resistance. These assumptions could be eliminated with access to antenna potential measurements.

Fourthly, the time-varying results presented in this thesis (or generated in future work based on this approach) could be used as a verification or basis for future numerical investigations. The significant transient behaviour documented in this thesis, particularly the switching between capacitive and inductive coupling modes, necessitates time-resolved modelling approaches. Hence the data presented in this thesis and the associated hybrid circuit-chemistry model can support future numerical work.

The key tangible outcome was the development of a new diagnostic tool for inductive plasmas based on a hybrid circuit-chemistry model. With additional validation and development, it is believed that this tool can aid in the development and operation of inductive plasma thrusters as a propellant-flexible space propulsion technology.

Table 6.1: Summary of all experimental conditions considered in this thesis. The shaded conditions are low power conditions that do not exhibit inductive coupling; in other words, they exhibit purely capacitive coupling.

Propellant			Input conditions						
Species	\dot{V} [L/min]	\dot{m} [g/s]	U_{anode} [kV], P_{anode} [kW]						
Chapter 2: Transient behaviour									
Key results: antenna current, magnetic field strength and radially-resolved visible emission.									
100 % N ₂	107	2.23	2, 4	4, 25					
32 % N ₂ + 68 % Ar	133	3.58	2, 4	4, 34					
32 % O ₂ + 68 % Ar	133	3.69	3, 4	10, 36					
Chapter 3: Power efficiency estimation									
Key results: inductive duty cycle, inductive frequency shift and thermal efficiency.									
100 % O ₂	76	1.66	1.0, 0.9 4.1, 27.8	2.0, 4.0 5.0, 58.4	2.4, 6.1 5.5, 75.0	2.5, 7.8 6.0, 96.4	3.1, 13.9	...	
100 % O ₂	105	2.28	1.0, 1.0	2.0, 4.2	3.0, 11.6	4.0, 26.1	5.0, 51.2		
100 % O ₂	105	2.29	1.0, 1.0 5.0, 49.8	2.0, 4.0 6.0, 86.1	3.4, 15.4 6.2, 105.8	3.4, 16.2	4.0, 24.5	...	
100 % O ₂	142	3.10	1.0, 0.9 5.0, 38.2	2.0, 4.0 5.5, 49.6	3.0, 9.9 6.0, 88.5	4.0, 18.9	4.3, 25.3	...	
42 % O ₂ + 58 % Ar	128	3.20	1.0, 0.9 4.0, 25.0	2.0, 4.0 4.4, 44.2	3.0, 10.2 6.0, 113.3	3.5, 14.0	3.6, 16.9	...	
32 % O ₂ + 68 % Ar	134	3.43	1.0, 0.9 4.0, 35.9	1.0, 0.9 5.0, 66.8	2.0, 4.0 5.5, 85.5	3.1, 10.1 6.0, 122.0	3.6, 25.4	...	
100 % CO ₂	80	2.40	1.0, 1.0 5.0, 42.6	2.0, 4.0 5.5, 56.3	3.0, 9.8	3.2, 13.5	4.0, 24.2	...	
100 % CO ₂	102	3.07	1.0, 0.9 5.0, 38.7	2.0, 4.1 5.5, 50.3	3.0, 10.0	4.2, 22.6	5.0, 38.7	...	
26 % CO ₂ + 74 % Ar	123	3.42	1.0, 1.0 4.0, 33.3	2.1, 4.3 4.5, 46.7	2.1, 4.3 5.0, 63.4	2.8, 8.6 5.5, 80.5	2.9, 11.5 6.0, 104.6	...	
31 % CO ₂ + 69 % Ar	130	3.66	1.0, 0.9 5.5, 77.9	2.0, 4.2 6.0, 99.4	3.0, 10.0 6.5, 129.3	3.2, 12.8 6.6, 143.4	5.0, 60.3 6.6, 143.4	...	6.7, 154.5
Chapter 4: Circuit model									
Key results: plasma volume, electrical conductivity and plasma current.									
100 % O ₂	76	1.81		2.5, 7.8	3.1, 13.9	4.1, 27.8	5.0, 58.4	5.5, 75.0	6.0, 96.4
100 % O ₂	142	3.38		4.3, 25.3	5.0, 38.2	5.5, 49.6	6.0, 88.5		
Chapter 5: Hybrid circuit–chemistry model									
Key results: effective collision frequency and localised electron fraction.									
100 % O ₂	142	3.38		4.3, 25.3	5.0, 38.2	5.5, 49.6			
42 % O ₂ + 58 % Ar	128	3.49		3.6, 16.9	4.0, 25.0	4.4, 44.2			
32 % O ₂ + 68 % Ar	134	3.74		3.6, 25.4	4.0, 35.9	5.0, 66.8			

